Characteristics of Atmospheric Humidity Derived From Reanalyses and Stable Isotopic Measurements From Space

by

Derek Philip Brown

B.A., University of Colorado, 1995

M.S., University of Colorado, 2006

A thesis submitted to the

Faculty of the Graduate School of the

University of Colorado in partial fulfillment

of the requirements for the degree of

Doctor of Philosophy

Department of Atmospheric and Oceanic Sciences

2011

This thesis entitled:
Characteristics of Atmospheric Humidity Derived From Reanalyses and Stable Isotopic Measurements From Space

written by Derek Philip Brown
has been approved for the Department of Atmospheric and Oceanic Sciences

____

Dr. David Noone

____

Dr. Darin Toohey

Date_______________

The final copy of this thesis has been examined by the signatories, and we
Find that both the content and the form meet acceptable presentation standards
Of scholarly work in the above mentioned discipline.

Brown, Derek P. (Ph.D., Atmospheric and Oceanic Sciences)

Characteristics of Atmospheric Humidity Derived From Reanalyses and Stable Isotopic Measurements From Space

Thesis directed by Dr. David Noone

This study identifies the large-scale processes that balance regional relative humidity (*H*), and utilizes satellite measurements of HDO/H_2O to characterize moisture processes that influence large-scale humidity. Using the MERRA reanalysis, dynamical and thermodynamical processes that balance zonal mean *H* are presented. The controls on *H* vary regionally, with eddy heat and moisture divergence being most influential in the extratropics. Condensation and eddy moisture convergence in midlatitudes, and subsidence and heat divergence in the NH subtropics, have increased from 1979-2004. While *H* has remained in balance, the strength of the compensating regional controls are changing in response to large-scale circulation shifts. The distribution of HDO/H_2O in water vapor, measured from the Tropospheric Emission Spectrometer, is analyzed to quantify influences from advection, convection, condensation, vapor recycling, and evapotranspiration. The analysis focuses on monsoonal regions, where strong hydrological coupling between the land surface and atmosphere provides an ideal test bed for the new dataset. Wet-minus-dry season differences in δD values over the Asian, South American, and North Australian regions are near-zero, negative, and positive, respectively, due to seasonal variations in the characteristics and strength of convection and subsidence. A global Lagrangian mass budget model, constrained by H_2O and

HDO/H_2O measurements, was constructed to give estimates of mixing and loss rates of moisture, fractional increases in humidity due to local moistening, the humidity and isotopic composition of regional source waters, and post-condensational exchange. The source water results are compared to expectations from simple mixing and dehydration models in order to gain new insight into the nature of the exchange processes (e.g., convective detrainment or direct mixing). Further insight is given by the sensitivity of the effective isotopic fractionation in the Lagrangian model to the conditions during condensation. Reversible moist adiabatic processes (i.e., cloud evaporation) are shown to moisten the dry subtropics, while rainfall evaporation is found to provide local moistening in the tropics and summertime subtropics. This study shows that compensating processes may preclude proper interpretation of small changes in mean humidity. Enhanced characterization of the processes that underlie the humidity budget is required for accounting for changes in atmospheric hydrology with climate shifts.

Dedication

To my bundle of joy, Adelaide. Let this mirror the inspiration and amazement you have brought me.

Acknowledgments

My first, and most earnest, acknowledgment must go to my advisor and chair of my thesis committee, David Noone. The pure zeal he has for research was contagious and motivational for me, even during tough times in the Ph.D. pursuit. David has been instrumental in ensuring my academic, professional, and financial well-being during my graduate work. In every sense, none of this work would have been possible without him. Many thanks also to committee members Brian Toon, Linnea Avallone, and Darin Toohey for helpful discussions and guidance.

Many people at the University of Colorado and elsewhere have given support during this work. I offer thanks to all: administration assistants, Laurie Conway and Sherry Yearsley; academic and computing advisors, Nik Buenning, Scotty Gregory, Jason Hill, and Camille Risi; and fieldwork cohorts, Leah Johnson, John Hurley, Jonathan Wright, Adriana Bailey, and Joe Galewsky. I would also like to thank several anonymous reviewers for their help and comments that improved my publications.

Data for this study were provided by the Tropospheric Emission Spectrometer team at NASA. I am extremely grateful for this team's diligence and timeliness in developing this data, without which this dissertation would not have been possible. I sincerely thank TES team leader, John Worden, for many helpful discussions and manuscript revisions, for infinite technical advice, and for serving on my thesis committee.

This research was primarily supported by a Graduate Research Environmental Fellowship from the U.S. Department of Energy's Global Change Education Program. I would like to thank the entire GREF team, including Jeffrey Gaffney, Nancy Marley, and

Milton Constantin, for several years of generous funding as well as for many well-organized and engaging conferences. I am also indebted to the Department of Atmospheric and Oceanic Sciences at the University of Colorado for several travel and academic grants. Lastly, I graciously acknowledge supplemental support from NASA for tuition fees and publication costs.

A heartfelt thank-you goes to my wonderful parents and in-laws, who provided confidence, support, and patience during the completion of my dissertation. For never once complaining about how infrequently I visit, my parents deserve far more credit than I can ever give them. To my friends, I offer thanks for pushing and prodding me to step away from the computer and get outside, which always acted to clear my mind and revamp my focus. To my loving dogs, Jasper and Linus, there will never be an emotional substitute for your endless wagging and smiling faces.

Finally, my most sincere acknowledgment goes to my wife, Mariah. Your support, encouragement, and companionship was without question the cornerstone of my sanity during this work. You have always given me the confidence and freedom to pursue the science I so love, and as such this achievement is as much yours as mine.

Contents

Tables

Table

Figures

Figure

1 Chapter 1

Introduction

1.1 Overview and Motivation

For Earth's global energy balance (Figure 1.1), water vapor (or humidity) plays a central role by directly impacting the net absorption and re-emission of longwave radiation and by indirectly impacting shortwave and longwave radiation through its effects on cloud formation and growth. Additionally, approximately half of the poleward, and a majority of the upward, heat transport within Earth's present atmosphere is due to the latent heat associated with phase changes of water vapor [*Sherwood et al.*, 2010b]. Since water vapor is the planet's dominant greenhouse gas [*Kiehl and Trenberth*, 1997] and is tightly coupled to long-term temperature fluctuations through the Clausius-Clapeyron relation [*Held and Soden*, 2000], it provides the climate system's strongest feedback [*Karl and Trenberth*, 2003]. The dominance of the water vapor feedback in the climate system is a robust result within IPCC AR4 General Circulation Models (Figure 1.2), and this feeback has the capacity to approximately double the direct warming from future greenhouse gas increases [*Manabe and Wetherald*, 1967; *Soden et al.*, 2005; *Randall et al.*, 2007]. Due to its pivotal roles in both weather and climate, a thorough understanding of the atmospheric processes that act to control water vapor is crucial for scientific advancement.

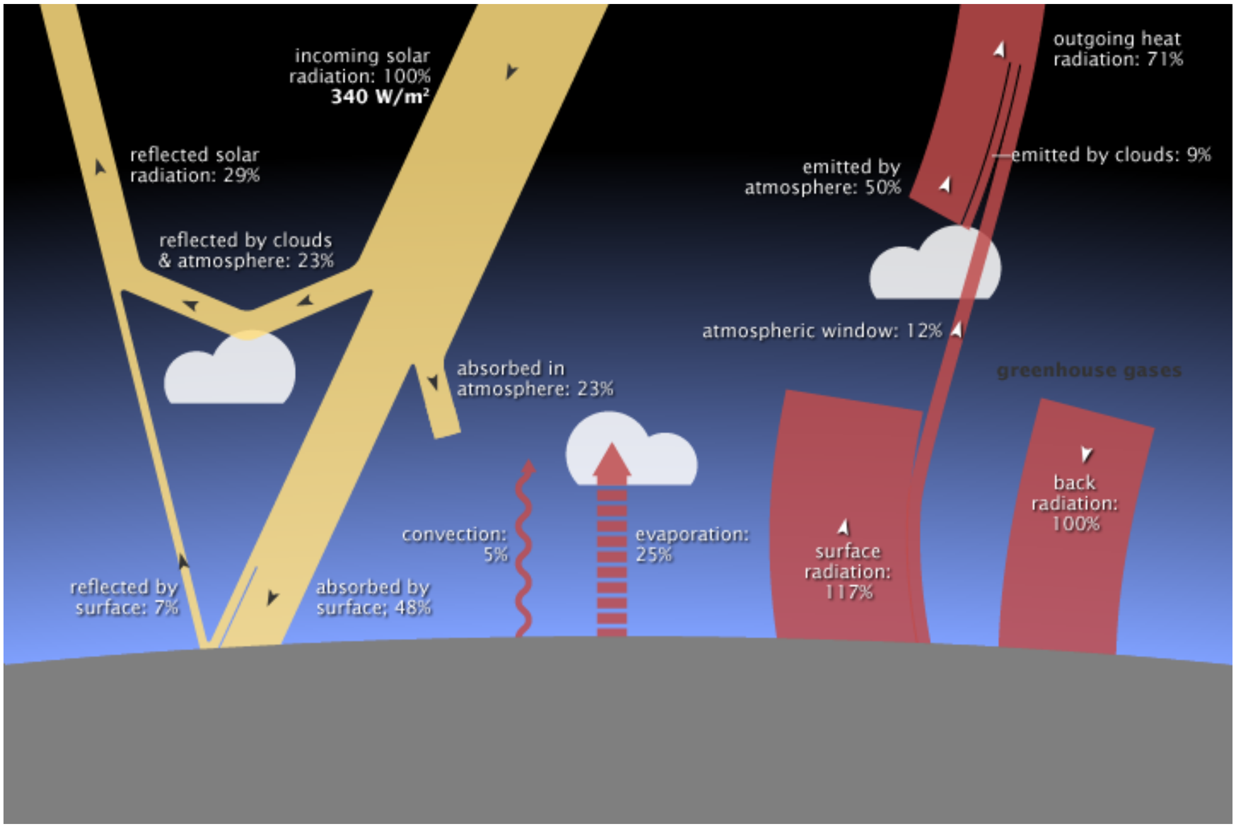

Figure 1.1: Estimate of the Earth's annual and global mean energy balance. Over the long term, the amount of incoming solar radiation absorbed by the Earth and atmosphere is balanced by the Earth and atmosphere releasing the same amount of outgoing longwave radiation. About half of the incoming solar radiation is absorbed by the Earth's surface. This energy is transferred to the atmosphere by warming the air in contact with the surface (convection), by evapotranspiration, and by longwave radiation that is largely absorbed by clouds and greenhouse gases. The atmosphere in turn radiates longwave energy back to Earth as well as out to space. Source: NASA illustration adapted from Kiehl and Trenberth [1997] by Robert Simmon.

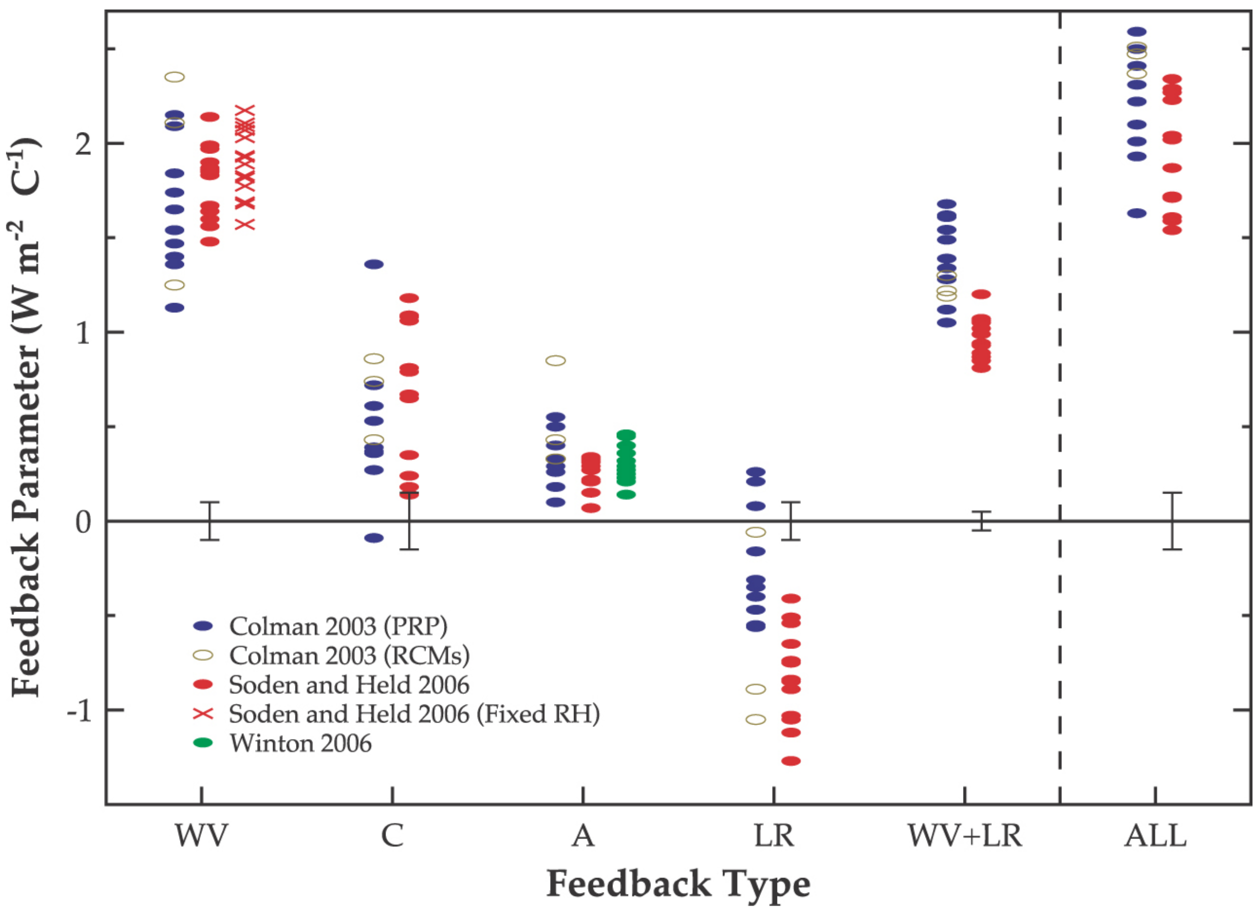

Figure 1.2: Comparison of GCM climate feedback parameters for water vapor (WV), cloud (C), surface albedo (A), lapse rate (LR) and the combined water vapor plus lapse rate (WV + LR) in units of $Wm^{-2}C^{-1}$. 'ALL' represents the sum of all feedbacks. Results are taken from Colman [2003; blue, black], Soden and Held [2006; red] and Winton [2006; green]. Closed blue and open black symbols from Colman [2003] represent calculations determined using the partial radiative perturbation (PRP) and the radiative-convective method (RCM) approaches respectively. Crosses represent the water vapor feedback computed for each model from Soden and Held [2006] assuming no change in relative humidity. Vertical bars depict the estimated uncertainty in the calculation of the feedbacks from Soden and Held [2006]. Source: Randall et al. [2007].

Water vapor is of central importance to many atmospheric processes, including storm initiation and growth, cloud microphysical processes, moist convection, and evapotranspiration. The processes that primarily act to control water vapor concentrations vary with geographical region (Figure 1.3). In the tropics, low-level moisture convergence associated with the tradewinds and condensation during ascent are the large-scale components to the water vapor balance; however, smaller scale processes such as entrainment and detrainment rates, convective moisture recycling, subsidence, and rainfall evaporation are also important. The subtropical region water vapor budget is primarily controlled by large-scale subsidence, strong oceanic evaporation, and eddy mixing with the midlatitudes, yet moist convection and the balance of evaporation versus precipitation of condensate formed near the top of the boundary layer (i.e., precipitation efficiency) are also important components to the budget. The midlatitude region's water vapor budget is largely controlled by transient eddy mixing and subsequent precipitation, with evapotranspiration and turbulent mixing also contributing. While the scientific community has a broad, qualitative understanding of the processes that influence water vapor concentrations in each geographical region, the accurate quantification of the effects of each of these processes on the large-scale humidity field remains an elusive and challenging aspect of climate science.

While progress in water vapor research is evident, the dominant processes that control humidity in certain regions are not yet fully agreed upon, especially in the driest areas of the globe (see comprehensive review in Sherwood et al. [2010b]). For example, local moistening of (dry) subsiding air in the intertropical regions is apparent since specific humidity here is at least two orders of magnitude higher than that at the tropopause [*Pierrehumbert*, 1999], yet several processes have been proposed to primarily moisten this air: evaporation or sublimation of condensate derived from tropical clouds [*Sun and Lindzen*, 1993], vertical convective mixing

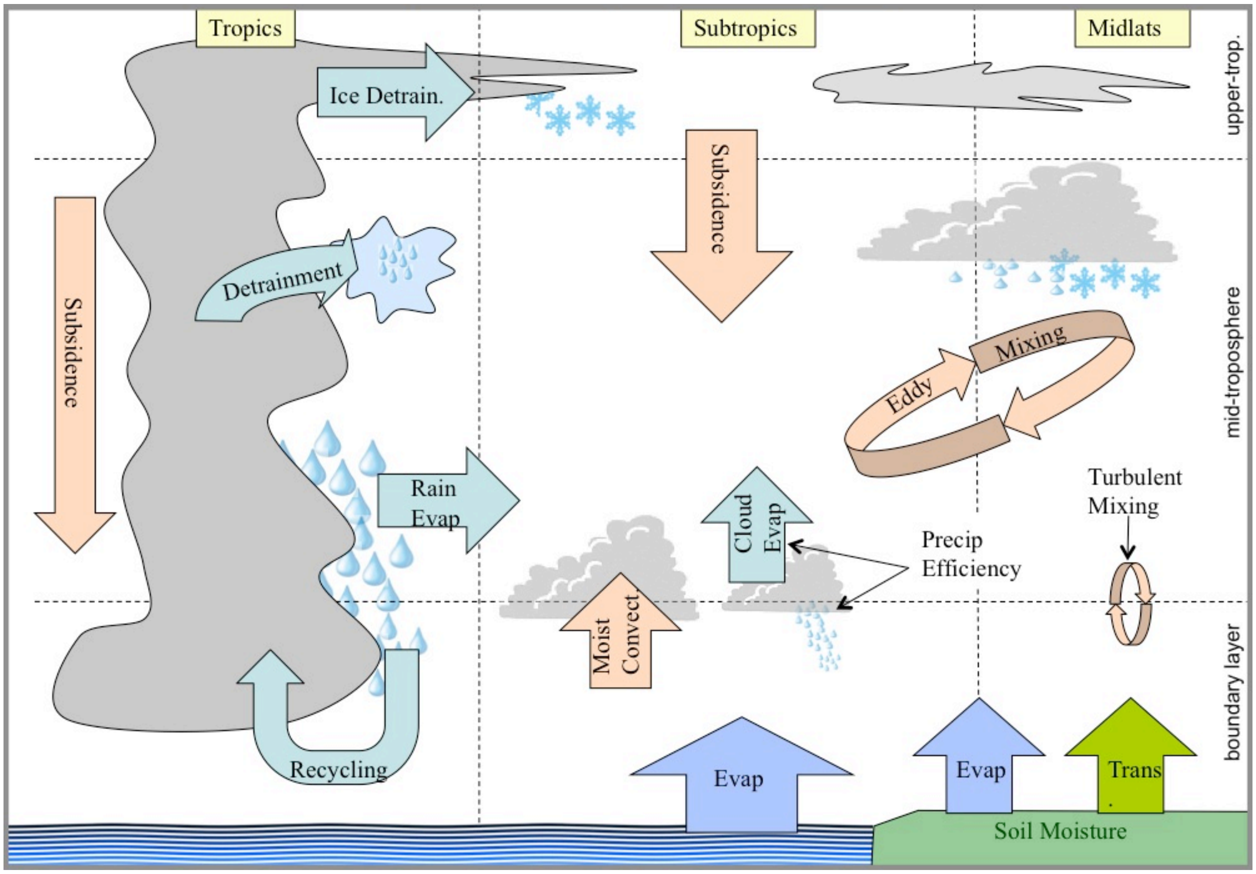

Figure 1.3: Schematic of water vapor processes for the tropical, subtropical, and midlatitude regions.

[*Yang and Pierrehumbert*, 1994], convergence of vertically transported water associated with small-scale eddies [*Couhert et al.*, 2010], and meridional mixing by large-scale eddies [*Salathe and Hartmann*, 1997; *Pierrehumbert*, 1998; *Pierrehumbert and Roca*, 1998; *Ryoo et al.*, 2009]. Part of the reason for disagreement between previous work on water vapor were limited radiosonde observations over most ocean and over continental areas with limited population or the lack of economic means to maintain upper-air stations.

Measurements of water vapor from operational and research satellites (e.g., TIROS, Meteosat, Aqua) have greatly increased the density and quality of global humidity data, especially in the upper troposphere where radiosonde measurements are unreliable [*Elliott and Gaffen*, 1991; *Soden and Lanzante*, 1996]. The effectiveness of assimilating satellite-borne water vapor data into reanalyses was recently demonstrated in a study by Dessler and Davis [2010], which cast doubt on a long-term decreasing specific humidity trend derived from the NCEP-NCAR Reanalysis [*Paltridge et al.*, 2009]. It was found that assimilated radiosonde data in the NCEP-NCAR product had allowed for spurious drying effects as instrument responsiveness increased over time [*Gaffen et al.*, 1991; *Ross and Gaffen*, 1998], whereas the drying was not found in four other reanalysis products that included the assimilation of satellite radiance or humidity retrievals into their specific humidity products. In addition, the newest reanalysis products (e.g., the Modern Era Retrospective-Analysis For Research And Applications,MERRA, [*Suarez et al.*, 2008]) directly address climate signal contamination due to changes in observing systems [*Dee*, 2005; *Bengtsson et al.*, 2007] via variational bias correction algorithms (e.g., Dee and Uppala, [2009]). Thus, with the aid of satellite data, recently developed reanalyses offer new hope for studies that strive to explore water vapor processes both globally and over long periods.

In addition to improved reanalyses, the water vapor community has recently benefited from the availability of isotopic ratio data measured from satellite [e.g., the Tropospheric Emission Spectrometer (TES) aboard NASA's AURA or the Scanning Imaging Absorption Spectrometer for Atmospheric Cartography (SCIAMACHY) aboard ENVISAT]. Measurements of the isotopic composition in water vapor enable one to trace the history of moist processes since the lighter and most abundant isotopologues of water (e.g., H_2O) preferentially evaporate over heavier ones (e.g., HDO or $H_2{}^{18}O$), and heavier isotopologues preferentially condense. Studies based on these measurements are increasing our understanding of water vapor processes [*Payne et al.*, 2007; *Worden et al.*, 2007; *Brown et al.*, 2008; *Risi et al.*, 2010], and are an important complement to past work that used the isotopic composition of precipitation to elucidate important humidity processes.

Research using isotopic information in precipitation showed that once an air parcel is removed from its primary moisture source (e.g., the ocean), isotopic fractionation during condensation and subsequent removal of the condensate via precipitation continually depletes the parcel's vapor (hereafter Rayleigh model), which generally leads to increasingly depleted precipitation as latitude, altitude, or continentality increases [*Dansgaard*, 1964; *Gat*, 1996]. This model was successful in explaining isotopic variations in high latitude (frozen) precipitation and has provided insight into climatic temperature variations [*Dansgaard*, 1964; *Jouzel et al.*, 2003; *Blunier et al.*, 2004; *Fricke and Wing*, 2004], but has failed to explain isotopic variations in tropical ice cores [*Bony et al.*, 2008; *Risi et al.*, 2008a]. The isotopic composition of precipitation is an integrated result of many processes that occur before, during, and after condensation occurs, and for unfrozen precipitation, isotopic equilibration with ambient air during descent can obscure any previously formed isotopic signal [*Friedman et al.*, 1962; *Lee and Fung*, 2008]. These aspects of precipitation isotopic ratios makes deduction of particular humidity processes difficult using precipitation alone, makes the failure to elucidate the specific processes which control the isotopic composition of tropical ice understandable (noted above), and is why measurements of the isotopic composition of water vapor will be very useful for advancing understanding of moist processes.

Although precision and accuracy are limited in satellite-borne measurements of water vapor isotopic ratios [*Worden et al.*, 2006], the spatial and temporal coverage they offer are invaluable for hydrologic research. Event-based measurements of the isotopic composition of water vapor can capture many important humidity processes, including air mass mixing and ice lofting [*Webster and Heymsfield*, 2003; *Risi et al.*, 2010; *Noone et al.*, 2011], post-condensational exchange (e.g., rainfall evaporation) [*Worden et al.*, 2007; *Brown et al.*, 2008; *Risi et al.*, 2010], evapotranspiration [*McGuffie and Henderson-Sellers*, 2004], variability in precipitation rates [*Hoffmann et al.*, 2003], turbulent transport, and convection [*Brown et al.*, 2008; *Risi et al.*, 2010]. An example of modeling the joint evolution of isotopic ratios and water vapor concentrations to elucidate different water vapor processes (Figure 1.4) was recently demonstrated in work by Noone [2010], where results from mixing a moist source (e.g., the marine boundary layer) with a drier source (e.g., mid to upper tropospheric air) were shown to substantially deviate from results where marine boundary layer air experiences condensation during ascent. Further, Noone [2010] found that the conditions during condensation can be captured by comparing the isotopic fractionation with the amount of residual vapor in clouds as condensation progresses, and thus demonstrated the usefulness of isotopologues in capturing aspects of the atmosphere such as precipitation efficiency and the recycling of subcloud vapor through post-condensational exchange (see Figure 1.4). This study and others have shown that important humidity processes emerge by considering not only the isotopic measurements

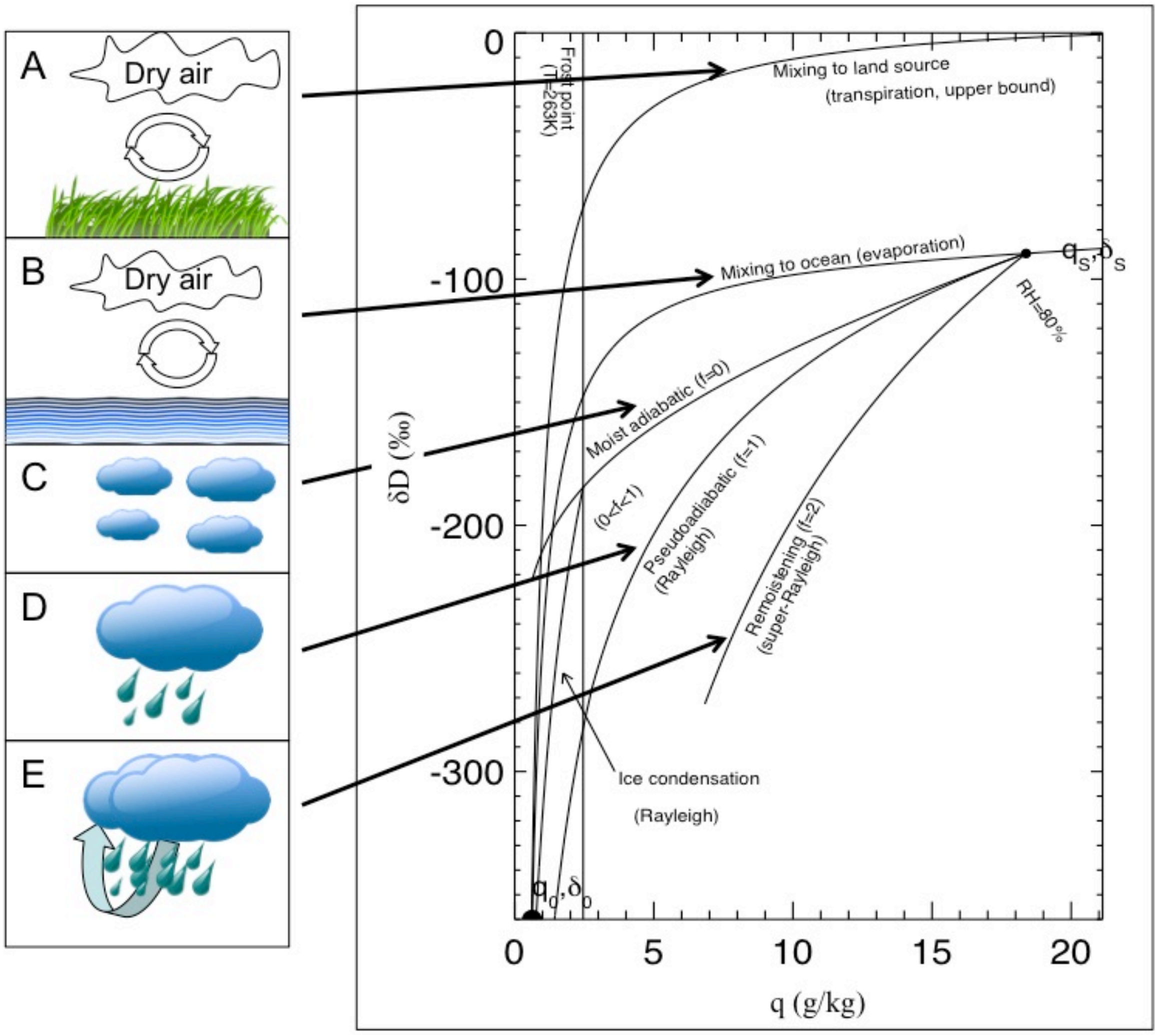

Figure 1.4: The joint evolution of δD [‰; found as (R/R_{VSMOW})-1 where R=HDO/H_2O and R_{VSMOW} is twice the Vienna Standard Mean Ocean Water standard of D/H and is 311.52x10^{-6}] and specific humidity (q; g/kg) in an air parcel (labeled lines in large right panel), as modeled by Noone [2010] during five different mixing and dehydration scenarios (represented graphically as Cases A-E, left panels): Case A, transpired moisture mixes with drier, more depleted air (q_0, δD_0; filled circle at lower left); Case B, moisture with typical q and δD values observed in the tropical marine boundary layer (q_s, δD_s; filled circle at upper right) mixes with drier, more depleted air; Case C, marine boundary layer moisture is allowed to condense, with the condensate remaining suspended and in isotopic equilibrium with the residual vapor (i.e., as in a reversible moist adiabatic process); Case D, marine boundary layer moisture condenses and the condensate is instantaneously removed from the system (i.e., as in a Rayleigh process); and Case E, marine boundary layer moisture condenses and the condensate falls from the cloud, however, water vapor resulting from subcloud post-condensational exchange (e.g., rainfall evaporation) is reintroduced into the system, leading to further depletion of the in-cloud, residual vapor (i.e., more depletion than a Rayleigh process).

themselves, but the degree to which the measurements deviate from those predicted by simple expectations (such as those expected from a Rayleigh model).

The recent availability of improved reanalyses and isotopic measurements from satellite provides an opportunity to characterize, in a well-balanced manner, unresolved water vapor processes that are important since atmospheric humidity plays a critical role in both weather and climate. There remains a need to better expose the controls of humidity in different regions, which can be achieved by using the isotopic measurements to increase our understanding of the processes which underlie the atmospheric humidity budgets. However, there also remains a need to understand the distribution of new and spatially resolved measurements of water isotopic composition.

1.2 Research Objectives

Although progress has been made on understanding water vapor's influence on many components of the climate system, it remains uncertain which combination of processes control humidity in different geographic locations and in different seasons. Through developing a sound understanding of the important controls on the humidity budget found from observations, forthcoming modeling efforts will find help in estimating future regional hydrologic changes. To this end, we identify important large-scale, seasonal humidity processes in different geographical regions by first decomposing the zonal mean temperature and moisture budgets derived from MERRA data (1979-2004) into their dynamic and thermodynamic components, and by using information from the water isotopic composition to further deduce which processes dominate the controls on the atmospheric moisture budgets.

The subtropical regions are especially important for climate since it is there that the infrared water vapor feedback is strongest [*Held and Soden*, 2000], relative changes in water vapor concentrations are large, and substantial variability is exerted on climate feedbacks [*Pierrehumbert*, 1999]. These regions account for a substantial portion of the 'atmospheric window' (see Figure 1.1), where large amounts of longwave radiation escape to space (Figure 1.5). General Circulation Model (GCM) results have shown robust changes in relative humidity that indicate a widening of the tropical Hadley cell and a poleward shift in the midlatitude storm tracks (e.g., *Seager et al.* [2010]; *Wright et al.* [2010]), yet the observed drying in the subtropics in the recent past far exceeds that predicted by the GCMs [*Sherwood et al.*, 2010a]. Thus, in addition to identifying the balance of important subtropical humidity processes, we analyze the trends of these processes from 1979-2004 and thus expose how the strength of those processes and the overall humidity balance have shifted over time.

Analyses of the distribution of satellite-derived ratios of deuterium (HDO) to $H_2{}^{16}O$ (hereafter, H_2O) in water vapor can provide important fingerprints of atmospheric processes [*Zakharov et al.*, 2004; *Herbin et al.*, 2007; *Payne et al.*, 2007; *Worden et al.*, 2007; *Brown et al.*, 2008; *Noone*, 2008b; a; *Risi et al.*, 2010]. This is a quickly advancing field, however many of the results presented here come from the first comprehensive analysis of HDO/H_2O data from satellite-based sensors. It is notable here that isotope-enabled GCMs do not currently reproduce the isotopic observations found from satellite-based, and other, sensors adequately. This is generally indicative of poor physical representations (or in some cases, parameterizations) of humidity and isotopic processes, and is a strong motivation to better characterize and constrain these processes with isotopic observations so that GCMs may better predict future changes in tropospheric hydrology.

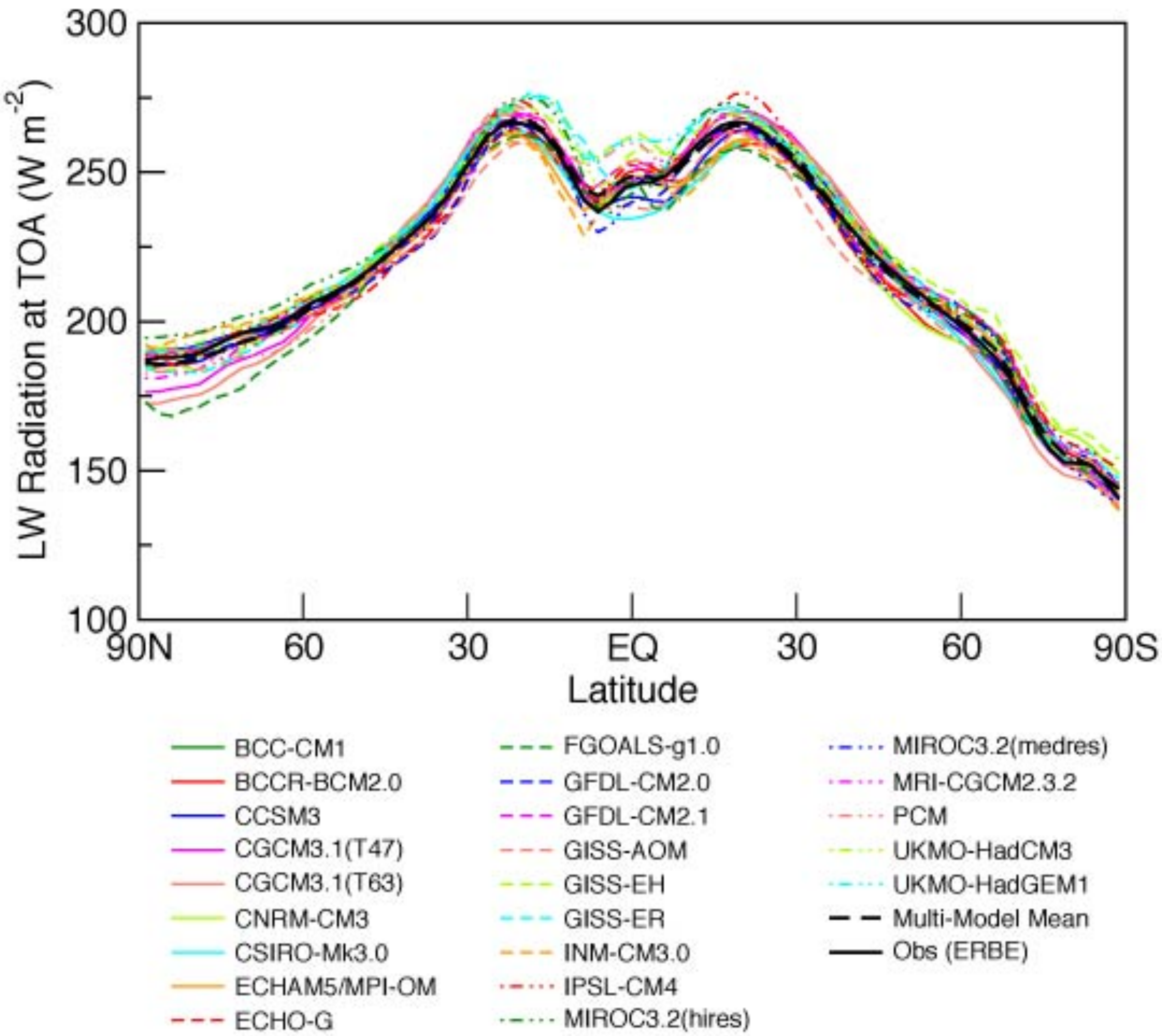

Figure 1.5: Zonal mean outgoing longwave (LW) radiation at the top-of-atmosphere (TOA) from models and observations used in the IPCC AR4, in units of Wm^{-2}. Source: Randall et al. [2007].

Continental monsoon regions exhibit particularly strong hydrological coupling between the land surface and the atmosphere, and are an ideal target to test the value of new isotopic data for use in quantitative analysis. The moisture budget in these regions reflects a complex balance of large-scale advective supply of water, surface exchange, and atmospheric condensation, all of which are important for the regional energy balance and climate (Figure 1.6). The transfers of heat and moisture from the land surface to the monsoonal atmosphere are substantial, yet are poorly resolved in current land-atmosphere models [*Dirmeyer*, 2006; *Dirmeyer et al.*, 2006]. Once the meteorological processes that control the isotopic composition are established, we examine and contrast the hydrologic budget inferred from the isotope measurements with budgets computed from non-isotope methods. Isotopic exchanges during turbulent mixing and intense condensation are also analyzed to expose the limitations of simple explanations based on Rayleigh distillation. Ultimately, a unique assessment of each monsoonal region is provided by quantifying relative contributions from advection, local and upstream convection, *in situ* condensation, recycling of vapor within regions of organized convection, and evapotranspiration.

Past work reveals that following condensation the effects of air mass mixing, re-evaporation of precipitation, and post-condensational isotopic exchange introduce non-Rayleigh isotopic variability of residual vapor [*Webster and Heymsfield*, 2003; *Lawrence et al.*, 2004; *Schmidt et al.*, 2005; *Worden et al.*, 2007; *Brown et al.*, 2008; *Wright et al.*, 2009b; *Field et al.*, 2010]. Additionally, the isotopic composition of water vapor is particularly sensitive to changes in convective activity and organization [*Lawrence and Gedzelman*, 1996; *Gedzelman et al.*, 2003; *Lawrence and Gedzelman*, 2003; *Lawrence et al.*, 2004; *Brown et al.*, 2008; *Risi et al.*, 2010]. Thus, to utilize the sensitivity of isotopic ratios to differential moistening and dehydration

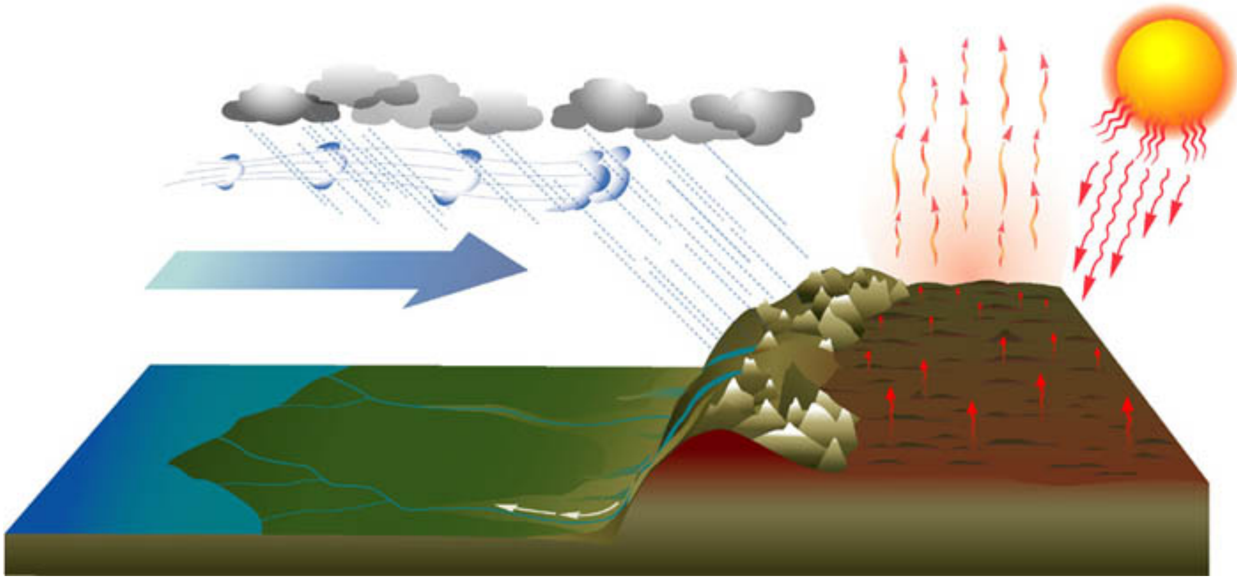

Figure 1.6: Schematic of typical monsoonal conditions (specifically the SE Asian Monsoon, with the high Tibetan Plateau downstream of the Himalaya). Monsoonal regions are associated with high levels of advective moisture transport (blue arrow), precipitation, and convection (red and yellow arrows) during seasons with maximum insolation. Source: Peter Clift, University of Aberdeen.

processes during convection and provide a comprehensive assessment of regional low to mid-tropospheric hydrology, a global Lagrangian mass budget model is constructed that is dually constrained by humidity and isotopic ratios found from TES. The model estimates average mixing and loss rates of moisture, moistening efficiency (i.e., fractional increases in atmospheric moisture), the humidity and isotopic composition of regional source waters, and post-condensational exchange for a given season. The regional source water results are compared to those expected from simple mixing and dehydration mechanisms (Figure 1.4) in order to infer their nature (e.g., convective detrainment, marine boundary layer air, etc.). This modeling work extends our understanding of the dominant moistening processes to the global scale, and particularly highlights the controls on the tropospheric humidity over climatically sensitive regions by using isotopic analysis. Specifically, this study uses the isotopic information to expose the influences from local moistening associated with convective mixing, cloud processes, and post-condensational exchange, which is not readily achievable from more traditional (non-isotopic) data.

1.3 Thesis Outline

The intent of this work is to provide an analysis of large-scale processes which dictate regional humidity as seen from reanalysis data, and to use isotopic analysis to characterize water vapor processes that influence large-scale humidity. Chapter 2 describes a decomposition of the relative humidity budget into its separate temperature and specific humidity components using MERRA data over the years 1979-2004. For the tropical, subtropical, and midlatitude regions, the balance of dynamical (e.g. divergence associated with eddies) and diabatic (e.g., latent heating) forcings within the individual temperature and moisture budgets are used to evaluate the overall balance of the relative humidity budget. Relative humidity is a pertinent quantity because it is at the core of coupling between the atmospheric moisture and energy budgets (e.g., via clouds, radiation, condensation and moistening processes). Relative humidity captures changes in both water vapor concentration and temperature, making it a different, yet complementary, metric to specific humidity that provides a more complete description of hydrologic change. Chapter 3 provides an assessment of the isotopic composition of water vapor as measured from TES, including local correlation analysis with several relevant proxies (e.g. lapse rates, advection) and seasonal assessment of five-day changes in isotopic composition as parcels approach different monsoonal regions. A mass exchange model is presented in Chapter 4, which uses specific humidity and HDO/H_2O ratios from TES to deduce humidity mixing and loss rates, the specific humidity and isotopic composition of dominant regional source reservoirs (e.g., detrained moisture from convective plumes, simple boundary layer air), and the degree of isotopic fractionation that occurs over various regions. Concluding remarks and a general summary of this work are found within Chapter 5.

2 Chapter 2

Temperature and Moisture Effects on Mid-Tropospheric Relative Humidity Values From 1979-2004 From MERRA

2.1 Abstract

The regional balances and trends of relative humidity in the recent past are important to resolve so that predictions of future changes may be improved. Moisture and temperature tendencies found from the MERRA reanalysis during 1979-2004 are used to calculate the primary processes that balance relative humidity in the tropical, subtropical, and midlatitude regions in the low to mid-troposphere. The effects on relative humidity from moisture and heat divergence associated with mean flow, stationary eddies, and transient eddies, and from turbulence, radiation, phase changes, and adiabatic processes are deduced. Results show changes in moisture primarily control deviations in relative humidity on intraseasonal timescales. The findings indicate substantial variation in the primary balancing components between regions and seasons, with transient eddies being a crucial dynamic component in all regions. Relative humidity effects from heat and moisture convergence via transient eddies are found to be approximately balanced in the tropics and subtropics, while in the midlatitudes, transient eddy moisture convergence produces precipitation and drives the hydrologic cycle. A strengthening of the hydrological cycle in the lower midlatitudes during boreal and austral winter is indicated by 12% increases over 26 years in both transient eddy moisture convergence and condensation. The southern hemisphere (15º-45º S) summer shows an opposing trend, with a weakening of the hydrologic cycle. Additionally, relative humidity decreases by adiabatic heating are increasing

during subtropical boreal winter, with compensating relative humidity increases from heat divergence. While the regional relative humidity budgets have remained balanced from 1979-2004, the primary balancing components are not static, and indicate shifts in the general circulation and climate.

2.2 Introduction

Relative humidity (hereafter *H*) is an important variable for many applications, including hydrology, agriculture, water resource management, and cloud research. *H* influences the amount and rate of evaporation in the atmosphere and on the land surface, and is an important factor in establishing the tropospheric distribution and amount of clouds [*Sundqvist*, 1978; *Price and Wood*, 2002]. In addition to their influence on radiation through cloud processes, *H* fluctuations in the free troposphere are important for the radiation budget since the infrared water vapor feedback scales with relative, instead of absolute, changes in water vapor concentration [*Couhert et al.*, 2010]. Importantly, in the dry intertropical troposphere, where the infrared water vapor feedback is strongest [*Held and Soden*, 2000], relative changes in water vapor concentration are large, and exert substantial variability on climate feedbacks [*Pierrehumbert*, 1999]. Thus, characterizing and quantifying the intertropical *H* budget, and the mechanisms which influence it, has great potential to increase our understanding in these disciplines (i.e., clouds, climate feedbacks, and hydrology). The intent of this study is to investigate the large-scale controls on *H* in the troposphere over the tropics, subtropics, and midlatitudes through an analysis of the *H* budget derived from atmospheric gridded analyses.

Many studies using climate models have indicated that global mean *H* will remain approximately constant as the earth warms, due to strong correlations in increasing specific humidity and saturation vapor pressure values that are expected to result from such warming (e.g., *Held and Soden* [2000]; *Sun and Held* [1996]). Other studies have shown weak decreases in global mean tropospheric *H* values in GCM climate warming experiments [*Manabe and Wetherald*, 1975; *Rind et al.*, 1991; *Mitchell and Ingram*, 1992], while observational studies of global mean, near-surface *H* have shown a weak decrease (e.g., *Dai* [2006]) or no trend (e.g., *Willet et al.* [2008]) over the years 1975 to 2005. Nonetheless, even if global mean *H* values have remained constant in the past and continue to do so in the future, the spatial distribution of *H* is not likely to remain static [*Mitchell and Ingram*, 1992; *Lorenz and DeWeaver*, 2007; *Sherwood et al.*, 2010a], and thus even small regional changes in *H* will substantially impact aspects of the climate [*Sherwood et al.*, 2010a]. Thus, the fundamental processes which have acted as primary controls on regional *H* in the recent past are important to understand in order to gain insight on potential changes in regional *H*, and are the focus of this study.

Tropospheric *H* has many thermodynamic and dynamic controls, and deciphering the primary controls on *H* is challenging due to the complexity of the atmospheric circulation [*Held and Soden*, 2000]. However, significant progress has been made on understanding *H* controls in the past twenty years. Using correlation analysis over large scales, Peixoto and Oort [1996] showed that variability in tropical tropospheric *H* is primarily moisture dependent, that *H* in the midlatitudes is largely temperature controlled, and that temperature exerts stronger seasonal control of *H* values over continents than over oceans. Couhert [2010] reported seasonally and spatially varying factors that influence *H* over the subtropical free troposphere; for instance, convective moistening and drying via subsidence were shown as primary controls on *H* during the Northern Hemisphere winter, while drying by condensation approximately balance convective moistening during the Summer Hemisphere summer. Sherwood [1996] concluded that the large-scale flow field, and the effects that convection have on it, are of primary importance for the global *H* budget; his findings illustrate that free tropospheric (700-200 hPa) *H* values could be estimated to within ±10% using analyzed large-scale wind fields with realistic boundary conditions, while ignoring subgrid scale moistening (i.e., cumulus-scale events). Several modeling studies using tracers of last saturation, where the specific humidity of an air parcel remains constant following the last saturation event, calculate that subtropical variability in atmospheric *H* largely reflects atmospheric circulation changes, and is not simply thermodynamically driven [*Sherwood*, 1996; *Pierrehumbert and Roca*, 1998; *Couhert et al.*, 2010; *Galewsky and Hurley*, 2010; *Hurley and Galewsky*, 2010a; b; *Wright et al.*, 2010]. In response to global warming, results from General Circulation Models (GCMs) have shown robust changes in *H* that indicate a widening of the tropical Hadley cell and a poleward shift in the midlatitude storm tracks (e.g., *Seager et al.* [2010]; *Wright et al.* [2010]), yet the observed drying in the subtropics in the recent past far exceeds that predicted by the GCMs [*Sherwood et al.*, 2010a]. Thus, the nature of the dynamical mechanisms responsible for variability in tropospheric *H* are not completely understood, and there remains a need to decipher the primary controls over *H* in the recent past.

For example, research has shown that the specific humidity in the subtropical dry zones (~500 hPa in the winter hemispheres) is two orders of magnitude higher than that at the tropopause, indicating that local moistening of the subsiding air does occur [*Pierrehumbert*, 1999] and that the balance of regional *H* is more complex. Many processes have been proposed to moisten this subtropical air, including evaporation or sublimation of condensate derived from tropical clouds [*Sun and Lindzen*, 1993], vertical convective mixing [*Yang and Pierrehumbert*, 1994], convergence of vertically transported water associated with small-scale eddies [*Couhert et al.*, 2010], and meridional mixing by large-scale eddies [*Salathe and Hartmann*, 1997; *Pierrehumbert*, 1998; *Pierrehumbert and Roca*, 1998; *Ryoo et al.*, 2009]. Thus, substantial disagreement exists on the mechanisms in this region that control specific humidity alone, which is only a single component of the more complex H budget. Thus, further characterization of the moisture and heat processes (e.g., moisture divergence by eddies, warming by adiabatic compression, etc.) that have acted to control regional H values in the recent past will add information to this unresolved issue.

A reanalysis project reprocesses observational data spanning an extended historical period using a consistent modern analysis system, and produces a coherent dataset that can be used for meteorological and climatological studies. The choice of a specific reanalysis for diagnostic calculations must take into account the spatial resolution, any aliasing effects due to post-processing from the model's native coordinate system to the pressure level archives, and any continuity problems associated with biases introduced (or reinforced) during assimilation [*Trenberth et al.*, 2002]. While the ECMWF reanalysis has noted flaws during post-processing due to an erroneous truncation scheme [*Trenberth et al.*, 2002], as well as continuity problems due to positive reinforcement of biases in satellite radiances with those of the assimilating model's first guess [*Stendel et al.*, 2000], biases associated with assimilated radiosonde data in the NCEP-NCAR product have been shown to introduce spurious drying trends as instrument responsiveness increased over time [*Dessler and Davis*, 2010]. The latter study revealed that the assimilation of satellite-borne water vapor data in recent reanalyses removed this spurious drying trend, and further comment that the newest reanalysis products (e.g., the Modern Era Retrospective-Analysis For Research And Applications, MERRA, [*Suarez et al.*, 2008]) directly address climate signal contamination due to changes in observing systems [*Dee*, 2005; *Bengtsson et al.*, 2007] via variational bias correction algorithms (e.g., Dee and Uppala, [2009]). In addition, the vertical levels of the MERRA product are those found to be optimal for diagnostic calculations of energy budgets using pressure coordinates [*Trenberth et al.*, 2002].

In the present study, we investigate the effects of terms in the temperature and moisture budgets, derived from the MERRA on tropical, subtropical, and midlatitude *H* in the lower to mid-troposphere (900-350 hPa) over the years 1979-2004. The purpose is to ascertain the summertime versus wintertime balance of factors which influence regional *H* and if the dominant factors for each region have changed over time. The *H* budget is decomposed into contributions associated with temperature (i.e., mean and eddy heat divergence, adiabatic expansion/compression, diabatic heating, and turbulence) and moisture (i.e., mean and eddy moisture divergence, evaporation/condensation, and turbulence) using three-dimensional data at six hour intervals. In so doing, we characterize the balance of the regional *H* budget in the recent past and provide preliminary information on the sensitivity of regional *H* budgets to future changes in atmospheric circulation. The methods and datasets are described in Section 2.3, the climatological long-term mean values of moisture and temperature are shown and discussed in Section 2.4.1, the differing sensitivities of *H* between datasets to changes in temperature and moisture are explained in Section 2.4.2, a validation of the methods is shown in Section 2.4.3, the balance of processes which govern tropical, subtropical, and midlatitude *H* values are shown in Section 2.4.4, and the 25 year trends in notable subtropical controls are shown in Section 2.4.5. A brief discussion and relevant conclusions are found in Section 2.5.

2.3 Methods

2.3.1 Relative Humidity Budget Equations

The basic derivation of the temperature and moisture components to the humidity budget equation is shown below, following Peixoto and Oort [1996]. The definition of relative humidity is the ratio of the actual water vapor pressure, *e,* to the saturation vapor pressure, e_s, at the same pressure *p* and air temperature *T*. One can make an approximation by using the ratio of the corresponding specific humidity values

$$H = \frac{e}{e_s} \approx \frac{q}{q_s}. \tag{E2.1}$$

This approximation is most robust when the vapor is near saturation and when $e \ll p$, which follows from the definition

$$q = \varepsilon \frac{e}{p + (1 - \varepsilon)e} \approx \varepsilon \frac{e}{p}, \tag{E2.2}$$

where $\varepsilon = R_d/R_v = 0.622$; the ratio of the gas constants for dry air and water vapor. Using the Clausius-Clapeyron equation to relate the saturation vapor pressure to the ambient temperature,

$$\frac{de_s}{dT} = \frac{Le_s}{R_v T^2} = \varepsilon \frac{Le_s}{R_d\, T^2}, \tag{E2.3}$$

where L represents the latent heat of water vaporization (assumed constant, and chosen here for $T \geq 273$ K), or sublimation ($T < 273$ K). Differentiating (E2.1) leads to

$$\frac{dH}{H} = \frac{de}{e} - \frac{de_s}{e_s} \approx \frac{dq}{q} - \frac{dq_s}{q_s}, \tag{E2.4}$$

and from (E2.2), it follows that

$$\frac{dq_s}{q_s} = \frac{de_s}{e_s} - \frac{dp}{p}. \tag{E2.5}$$

At constant pressure,

$$\frac{dq_s}{q_s} = \frac{de_s}{e_s} = \left(\frac{L}{R_v T}\right)\frac{dT}{T}. \tag{E2.6}$$

Inserting (E2.6) into (E2.4), the relationship between relative humidity, moisture, and temperature is found as

$$\frac{dH}{H} = \frac{dq}{q} - \left(\frac{L}{R_v T}\right)\frac{dT}{T}. \tag{E2.7}$$

Of note from (E2.7) is that the changes in H due to changes in T and q are of opposite sign, and that on constant pressure surfaces, fractional changes in T are ~20 times more effective at changing the value of H than are fractional changes in q. Rearranging, and taking the temporal derivative of (E2.7) leads to

$$\frac{dH}{dt} \approx \frac{1}{q_s}\frac{dq}{dt} - \left(\frac{HL}{R_v T^2}\right)\frac{dT}{dt}, \tag{E2.8}$$

where the moisture and temperature tendency terms have scaling factors (hereafter, $f_q = 1/q_s$ and $f_T = -(HL)/(R_v T^2)$, respectively) which compute their effects on the H tendency.

The role of advective transport on the three-dimensional moisture and temperature budgets is evaluated by decomposing the Lagrangian budget. The total derivative for moisture is written as

$$\frac{dq}{dt} = S(q) + D\ , \tag{E2.9}$$

where $S(q)$ is the source-sink term of water vapor within a unit mass of air due to phase changes and D is the molecular and transport by turbulent eddies of scales smaller than that resolved by the available gridded datasets. Expanding the total derivative in (E2.9), and placing the large-scale dynamical components on the left-hand side, we find a general expression for the q budget on a sphere;

$$\left(\frac{\partial(uq)}{R\cos\phi\partial\lambda} + \frac{\partial(vq\cos\phi)}{R\cos\phi\partial\phi} + \frac{\partial(\omega q)}{\partial p}\right) = S(q) + D - \frac{\partial q}{\partial t}, \tag{E2.10}$$

with R the radius of earth, u and v the zonal and meridional wind speeds, ω the vertical velocity in pressure units, ϕ and λ the latitude and longitude, and p the vertical (pressure) coordinate. Taking the zonal average of (E2.10), and considering long-term statistics (i.e., monthly or seasonal means) where the local rate of change, $\partial q / \partial t$, can be neglected [*Peixoto and Oort*, 1996], the budget equation for q takes the form

$$\left(\frac{\partial \left(\left[\overline{vq} \right] \cos\phi \right)}{R\cos\phi \partial\phi} + \frac{\partial \left[\overline{\omega q} \right]}{\partial p} \right) = \left[\overline{S(q)} \right] + \left[\overline{D} \right] \tag{E2.11}$$

where square brackets denote a zonal average and the overbar denotes the time mean. The flux divergence terms on the left hand side of (E2.11) can be further decomposed into mean and eddy components. For example, the mean divergence of the northward transport of water vapor across a specific latitude circle is found as

$$\frac{\partial \left(\left[\overline{vq} \right] \cos\phi \right)}{R\cos\phi \partial\phi} = \frac{\partial \left(\left[\overline{v} \right] \left[\overline{q} \right] \cos\phi \right)}{R\cos\phi \partial\phi} + \frac{\partial \left(\left[\overline{v'q'} \right] \cos\phi \right)}{R\cos\phi \partial\phi} + \frac{\partial \left(\left[\overline{v}^{*} \overline{q}^{*} \right] \cos\phi \right)}{R\cos\phi \partial\phi} \tag{E2.12}$$

where an overbar ($^{-}$)represents the time mean, a prime ($'$) the deviation from the time average, and an asterisk (*)the deviation from the zonal average. The three terms on the right hand side of (E2.12) represent the meridional flux divergence associated with mean flow, transient eddies, and stationary eddies, respectively. The same decomposition is performed in pressure coordinates for the vertical flux divergence term which yields a total of six terms to describe the advective contributions to the time mean and zonal mean q. This decomposition of the zonally averaged water vapor budget aids in identifying which type of atmospheric motions predominantly control q, and thus to some extent H, values in the troposphere.

Following the derivation techniques in forming (E2.10), the time averaged, zonal mean budget equation for temperature is

$$\left(\frac{\partial\left(\left[\overline{vT}\right]\cos\phi\right)}{R\cos\phi\partial\phi}+\frac{\partial\left[\overline{\omega T}\right]}{\partial p}\right)+\frac{\kappa\left[\overline{\omega T}\right]}{p}=\left[\frac{\overline{Q}}{c_p}\right] \tag{E2.13}$$

with κ equal to R_v/c_p, c_p the heat capacity of air at constant pressure, and Q the diabatic heating rate. The three (dynamical) terms on the left hand side of (E2.13) represent the meridional flux divergence of temperature, the vertical flux divergence of temperature, and the adiabatic temperature tendency, while the single term on the right hand side represent the temperature tendency due to all diabatic processes. The diabatic term includes heating associated with radiation, turbulent diffusion, friction, and latent heating or cooling. A similar decomposition as in (E2.12) is used to find the temperature flux divergence terms with respect to the zonal mean, the transient eddies, and the stationary eddies. The effects of the T and q budget components on H can then be found by scaling according to the derivation in (E2.8).

2.3.2 Data Selection, Averaging, and Divergence Calculations

From the MERRA assimilated gridded product (MERRA product name, inst_3d_asm_Cp), values of u, v, ω, q, T, H, and p_s (surface pressure are taken at six hourly intervals for the years 1979-2004). The MERRA daily product is sampled at 2.5º longitudinal and 1.25º latitudinal spacing, using the 25 pressure levels reported from 1000-100 hPa. The analysis focuses on zonal averages within the low to mid-troposphere (900-350 hPa) from 60º S to 60º N latitude, and uses long-term (1979-2004) seasonal (DJF, December-January-February; JJA, June-July-August) statistics.

For this analysis, the large-scale dynamical terms in the moisture and temperature budgets [terms on the left hand sides of (E2.11) and (E2.13)], as well as their mean and eddy components, were computed using the MERRA state variables at six hour intervals, with monthly averages archived. Divergence calculations were performed using finite differencing on a sphere, making use of centered finite differencing above 1000 hPa and below 100 hPa. MERRA monthly mean temperature and moisture tendency data (MERRA product names, tavgM_3d_tdt_Cp and tavgM_3d_qdt_Cp, respectively) are used to validate our calculated monthly large-scale dynamical components, as well as to establish the diabatic and turbulent components [terms on the right hand sides of (E2.11) and (E2.13)]. The advantage of calculating the dynamical components independently is the separation of the total dynamical forcing on q and T into mean and eddy components, and the separation of adiabatic compression/expansion effects on T from other large-scale dynamical processes.

The MERRA monthly mean moisture tendency data include diabatic tendencies resulting from turbulence and moist processes. The turbulence term includes surface evaporation, while the moist processes term includes the effects of the convection parameterization [*Moorthi and Suarez*, 1992] and all other effects from the cloud microphysics and large scale and anvil precipitation schemes. The MERRA monthly mean temperature tendency data include diabatic tendencies resulting from friction (from both turbulence and gravity wave drag), radiation, moist processes, and turbulence (including sensible heat from the surface). Close inspection reveals that the friction components are unimportant to the long-term budget at the 900-350 hPa levels, and thus are not shown here. The MERRA monthly mean T and q tendency products include an analysis tendency introduced during the corrector segment of the Incremental Analysis Update cycle [*Bloom et al.*, 1996]. These values are not shown here, since they are found to have negligible effects on the balance of the long-term humidity budget.

All monthly averaged T and q tendency terms are multiplied by the appropriate monthly H conversion factor [i.e., f_q and f_T from (E2.8)] to deduce the effects on relative humidity values. To aid the reader, a legend containing the naming convention of the many effects on H due to the dynamical and diabatic components of the zonally averaged T and q budgets is shown as Table 2.1.

name	*term*	*description*	*units*
H_DQDIVG	$f_q \left(\frac{\partial([\overline{vq}]\cos\phi)}{R\cos\phi\partial\phi} + \frac{\partial[\overline{\omega q}]}{\partial p}\right)$	*H* tendency due to total moisture flux divergence	%/day
H_DVQZM	$f_q \frac{\partial([\bar{v}][\bar{q}]\cos\phi)}{R\cos\phi\partial\phi}$	*H* tendency due to mean meridional moisture flux divergence	%/day
H_DVQSE	$f_q \frac{\partial([\bar{v}^*\bar{q}^*]\cos\phi)}{R\cos\phi\partial\phi}$	*H* tendency due to stat. eddy merid. moisture flux divergence	%/day
H_DVQTE	$f_q \frac{\partial([\overline{v'q'}]\cos\phi)}{R\cos\phi\partial\phi}$	*H* tendency due to tran. eddy merid. moisture flux divergence	%/day
H_DWQZM	$f_q \frac{\partial([\bar{\omega}][\bar{q}])}{\partial p}$	*H* tendency due to mean vertical moisture flux divergence	%/day
H_DWQSE	$f_q \frac{\partial[\bar{\omega}^*\bar{q}^*]}{\partial p}$	*H* tendency due to stat. eddy vert. moisture flux divergence	%/day
H_DWQTE	$f_q \frac{\partial[\overline{\omega'q'}]}{\partial p}$	*H* tendency due to tran. eddy vert. moisture flux divergence	%/day
H_DQCOND	$f_q \partial q_{cond}$ [a]	*H* tendency due to moist processes (evaporation/condensation)	%/day
H_DQTURB	$f_q \partial q_{turb}$ [a]	*H* tendency due to turbulence (including surface evaporation)	%/day
H_DTDIVG	$f_T \left(\frac{\partial([\overline{vT}]\cos\phi)}{R\cos\phi\partial\phi} + \frac{\partial[\overline{\omega T}]}{\partial p}\right)$	*H* tendency due to total heat flux divergence	%/day
H_DVTZM	$f_T \frac{\partial([\bar{v}][\bar{T}]\cos\phi)}{R\cos\phi\partial\phi}$	*H* tendency due to mean meridional heat flux divergence	%/day
H_DVTSE	$f_T \frac{\partial([\bar{v}^*\bar{T}^*]\cos\phi)}{R\cos\phi\partial\phi}$	*H* tendency due to stat. eddy merid. heat flux divergence	%/day
H_DVTTE	$f_T \frac{\partial([\overline{v'T'}]\cos\phi)}{R\cos\phi\partial\phi}$	*H* tendency due to tran. eddy merid. heat flux divergence	%/day
H_DWTZM	$f_T \frac{\partial([\bar{\omega}][\bar{T}])}{\partial p}$	*H* tendency due to mean vertical heat flux divergence	%/day
H_DWTSE	$f_T \frac{\partial[\bar{\omega}^*\bar{T}^*]}{\partial p}$	*H* tendency due to stat. eddy vert. heat flux divergence	%/day
H_DWTTE	$f_T \frac{\partial[\overline{\omega'T'}]}{\partial p}$	*H* tendency due to tran. eddy vert. heat flux divergence	%/day
H_DTWORK	$f_T \kappa[\overline{\omega T}]/p$	*H* tendency due to adiabatic compression/expansion	%/day
H_DTTURB	$f_T \partial T_{turb}$ [a]	*H* tendency due to turbulence (including sensible surface heat flux)	%/day
H_DTCOND	$f_T \partial T_{cond}$ [a]	*H* tendency due to latent heating/cooling	%/day
H_DTRADN	$f_T \partial T_{radn}$ [a]	*H* tendency due to radiation	%/day

[a]See Suarez et al. [2008] for full calculation of the respective moisture or temperature tendency

Table 2.1: Index of terms from relative humidity budget.

2.4 Results

2.4.1 Long-Term Seasonal Average MERRA Moisture, Temperature, and RH Values

Long-term zonal mean values of H, q, and T for the December-January-February (DJF) and June-July-August (JJA) are shown in Figure 2.1a-f. The spatial distributions in Figures 2.1a-b show the highest H values near the surface in the tropics and midlatitudes, with relatively high H values throughout the atmospheric column over these regions. Tropical H maxima coincide with global maxima of q and T (Figures 2.1c-f) while the mid-latitude H maxima correspond with sharp meridional gradients in T and q. The reduction in saturation specific humidity values caused by lower poleward T values outweighs the H effects of decreasing q values, and thus H increases poleward of 35º N or S. H minima in both seasons are found near 500 hPa in the subtropical regions (20º-35º N and S), with the winter hemisphere minima ($H \approx$ 10-20%) being lower than those found in the summer hemisphere ($H \approx$ 25-30%). These winter minima coincide with low q values (1-2 g/kg) and a sharp meridional gradient in temperature, and are generally regarded as a result of subsiding air motions associated with the descending branch of the Hadley Cell.

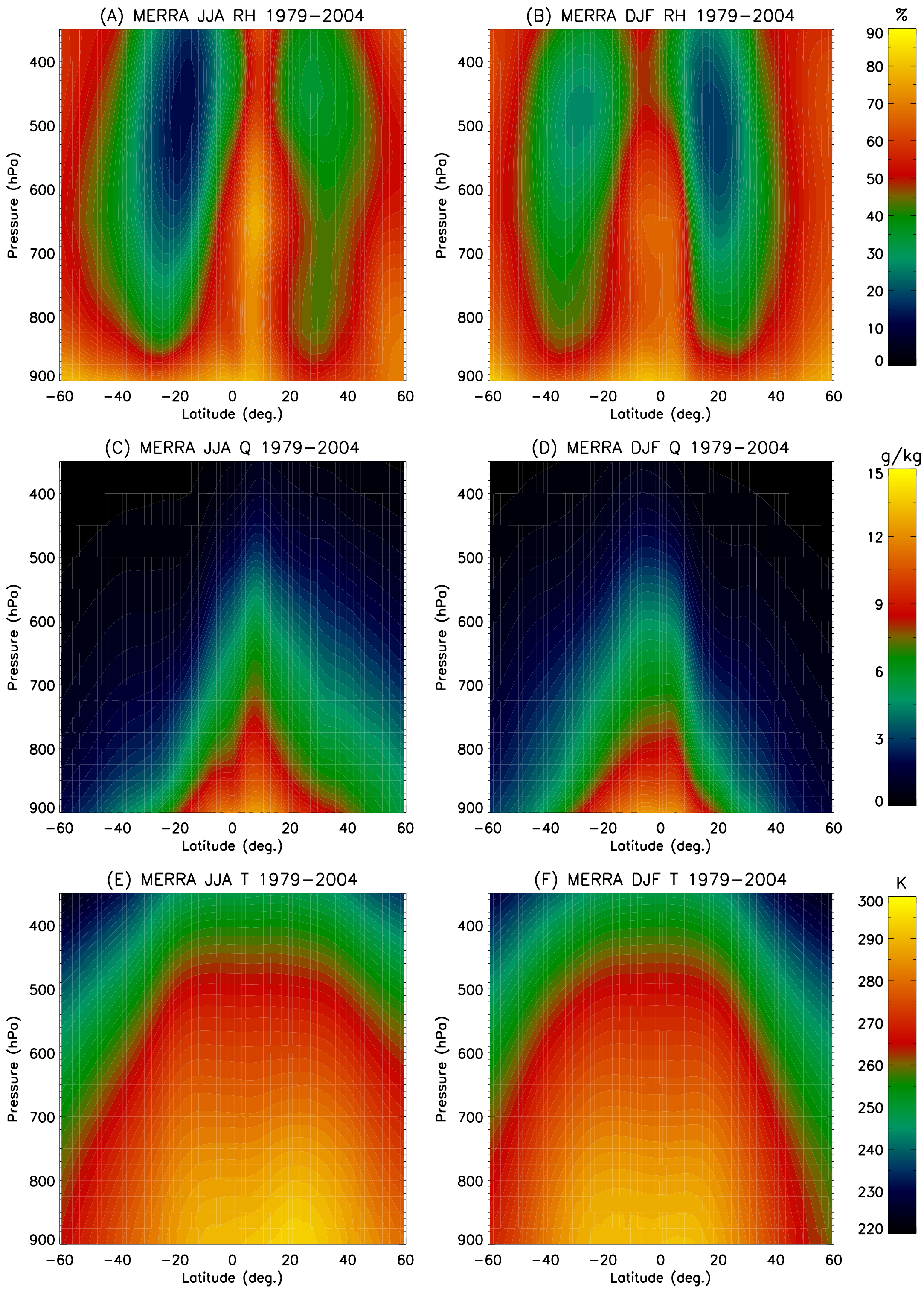

Figure 2.1: Long-term average H (a, b), q (c,d), and T (e,f) values during June-July-August (JJA, left panels) and December-January-February (DJF, right panels).

Long-term average monthly standard deviations of *T* and *q* (Figure 2.2) can provide information on the expected average monthly range of changes in *T* and *q* during each season (JJA or DJF). The monthly standard deviation of *q* (σ_q ;Figures 2.2a-b) shows maxima at lower levels in the subtropics (15-35º) during both DJF and JJA, and past work has shown these to be largely associated with intermittent intrusions by moist plumes from the tropics (i.e., 'atmospheric rivers', [*Newell and Zhu*, 1994; *Zhu and Newell*, 1994; 1998; *Ralph et al.*, 2006; *Neiman et al.*, 2008; *Guan et al.*, 2010]). Minimum monthly σ_q and a weak meridional gradient in monthly σ_q are found in the drier levels above 500 hPa, where anomalously moist tropical plumes are rare due to rainout during moist adiabatic ascent. The spatial structure of monthly σ_q is fundamentally different than monthly σ_T (Figures 2.2c-d), where there is a strong meridional gradient at all levels but little vertical gradient equatorward of 40º. The latent heating that tropical storms create above 500 hPa helps maintain the upper level meridional temperature gradients (see Figure 2.2e-f). When these warm anomalies mix with colder poleward air, upper-level deviations in temperature result. Monthly σ_T increases with increasing latitude values at all levels as a result of higher baroclinicity associated with the polar front.

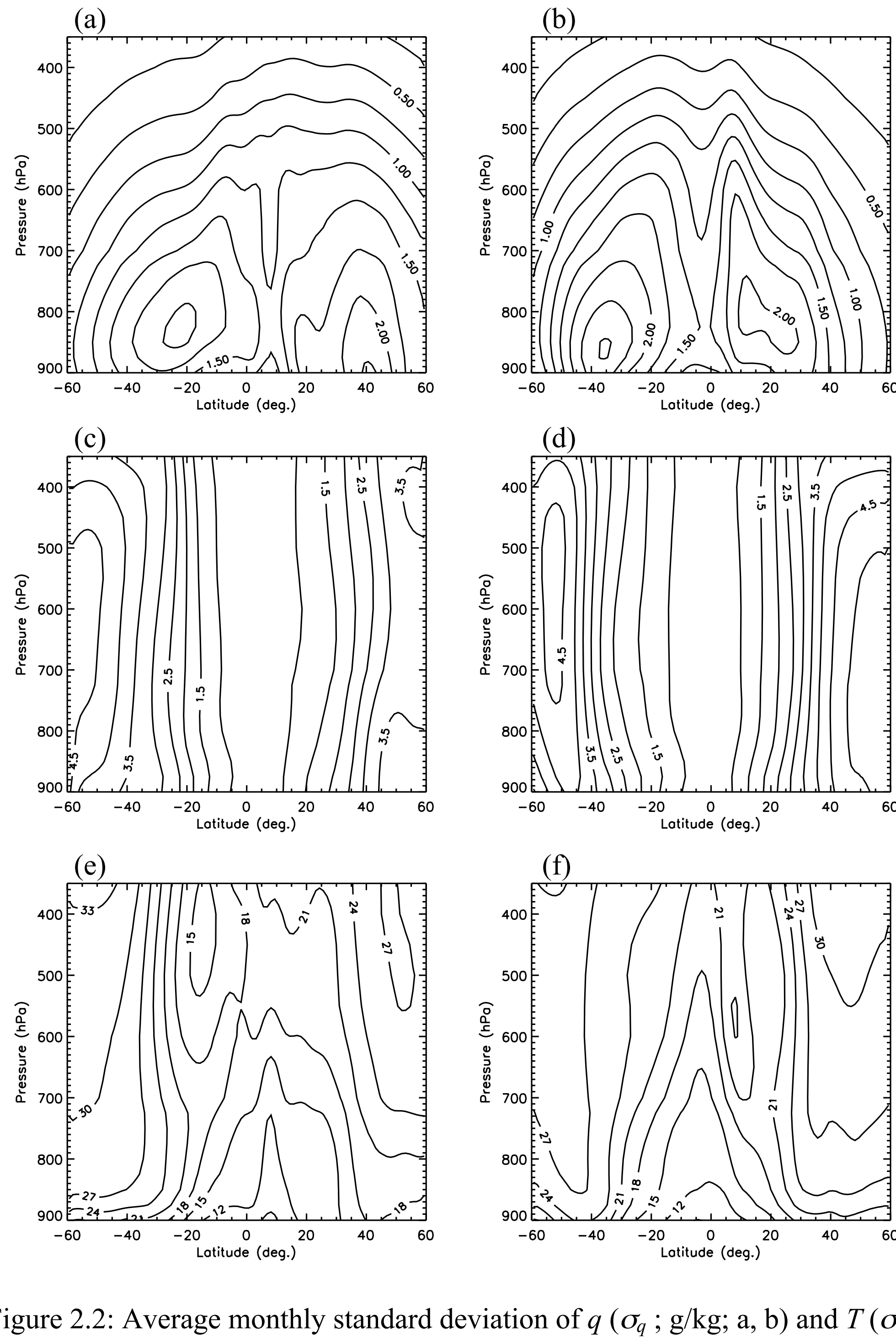

Figure 2.2: Average monthly standard deviation of q (σ_q ; g/kg; a, b) and T (σ_T ; K; c, d) and H (σ_H ; %; e, f) for JJA (left panels) and DJF (right panels) from MERRA for the 1979-2004 period. Contour intervals for are 0.25 g/kg (a,b), 0.5 K (c,d), and 3% (e,f).

Figure 2.3 indicates that the interannual standard deviations of *q* (0.01-0.45 g/kg) and *H* (1-3%) are an order of magnitude smaller than the monthly deviations in Figure 2.2. Large interannual deviations in *q* and *H* are found in the tropical low to mid-troposphere (~800 hPa), and coincide with very high seasonal mean *H* values (Figure 2.1). Thus, year-to-year variations in *H* in the tropics are largely influenced by moisture amounts, as noted by Peixoto and Oort [1996], and tend to be influenced by the yearly variations in position, structure, and strength of the ITCZ [*Okajima et al.*, 2003; *Wu et al.*, 2003; *Davenport*, 2009; *Bellucci et al.*, 2010], which itself has ENSO influences [*Chen and Lin*, 2005; *Munnich and Neelin*, 2005]. The large deviations in *H* near 60º S during JJA coincide with a sharp meridional increase in intraseasonal deviations in *T*, which is linked to year-to-year changes in circulation patterns in the Antarctic troposphere [*Wexler*, 1959]. Opposed to the monthly deviations of *T*, which show a strong meridional gradient (Figures 2.2c-d), the interannual deviations of *T* primarily show a vertical structure, which is related to increasing variations in planetary wave activity with height [*Trenberth*, 1980] and reduced sensitivity of interannual *T* deviations to changes in ENSO related patterns at lower levels [*Boyle*, 2000]. Below 750 hPa, the air is relatively well mixed, thus interannual deviations in *T* are low.

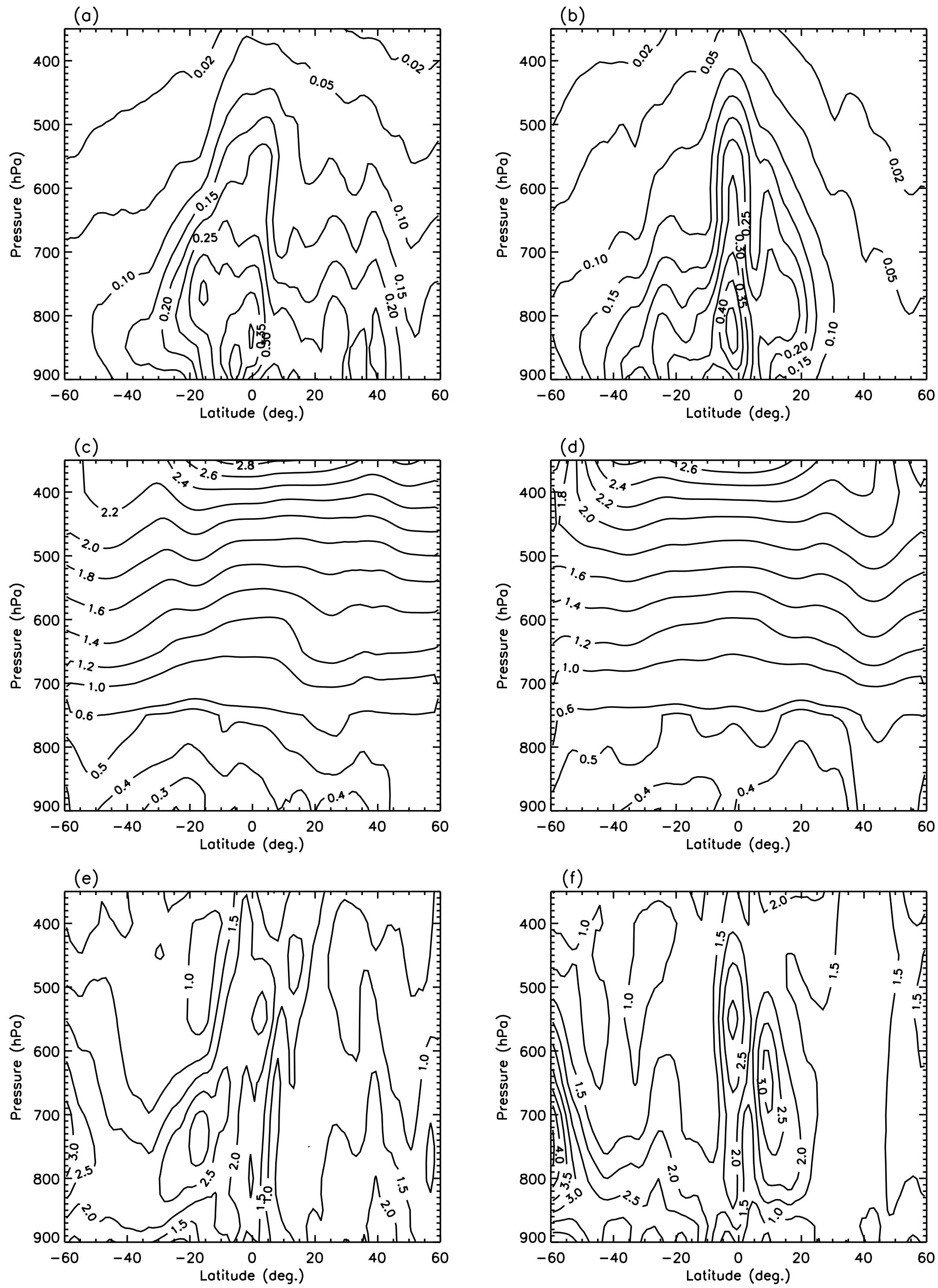

Figure 2.3: Average interannual standard deviation of q (g/kg; a, b), T (K; c, d), and H (%; e, f) for all JJA (left panels) and all DJF (right panels) from MERRA for the 1979-2004 period. Contour intervals: for (a,b), 0.05 g/kg with one additional contour at 0.02 g/kg; for (c,d), 0.1 K from 0-1 K and 0.2 K from 1-3 K; and, for (e,f), 0.5%.

2.4.2 Relative Humidity Sensitivity to Changes in Moisture and Temperature

The sensitivity of the atmosphere to potential changes in moisture and heat is captured in the *H* conversion factors, f_q and f_T. The long-term, zonal mean averages for these variables at the 900-350 hPa levels for MERRA are shown in Figure 2.4. Figures 2.4a and b show that f_q values reach a minimum at low levels in the tropical regions, and a maximun at upper levels in the midlatitudes. *H* values are more sensitive to changes in moisture variations above the surface and poleward of the tropics, and are directly related to the spatial distribution of *T* (Figures 2.1e-f). Thus, from 1979-2004, for an equal change in *q* (via divergence, condensation, etc.), the upper midlatitude regional *H* would change more so than at lower levels in the tropics. The f_T values (Figure 2.4c-d) show *H* is more sensitive (i.e., f_T values have larger magnitude) with both increasing *H* and $1/T^2$ values, thus cold and moist regions should expect the highest f_T values. However, over the latitudes and levels used here the variations in f_T primarily follow those in *H*; f_T has stronger spatial correlations with *H* (r = -0.82) than with $1/T^2$ (r = -0.32).

Maximum sensitivity (i.e., f_T most negative) is generally found at all levels in the tropics, as well as at all levels poleward of 45º N or S. Low sensitivity values are found in the subtropical dry zones (600-500 hpa, 20º-35º N or S), with the winter hemisphere dry zone *H* values the least sensitive to changes in *T*. During both summer and winter, the Southern Hemisphere *H* values are less sensitive to potential changes in *T* than those in the Northern Hemisphere. Modeling studies that have shown greater decreases in zonal mean *H* values in the southern versus northern hemisphere in response to global warming [*Mitchell and Ingram*, 1992; *Lorenz and DeWeaver*, 2007; *Sherwood et al.*, 2010a; *Wright et al.*, 2010]. Thus, this asymmetric result in subtropical *H* sensitivity to *T* suggests that, given the recent state of the climate, a greater change in heating

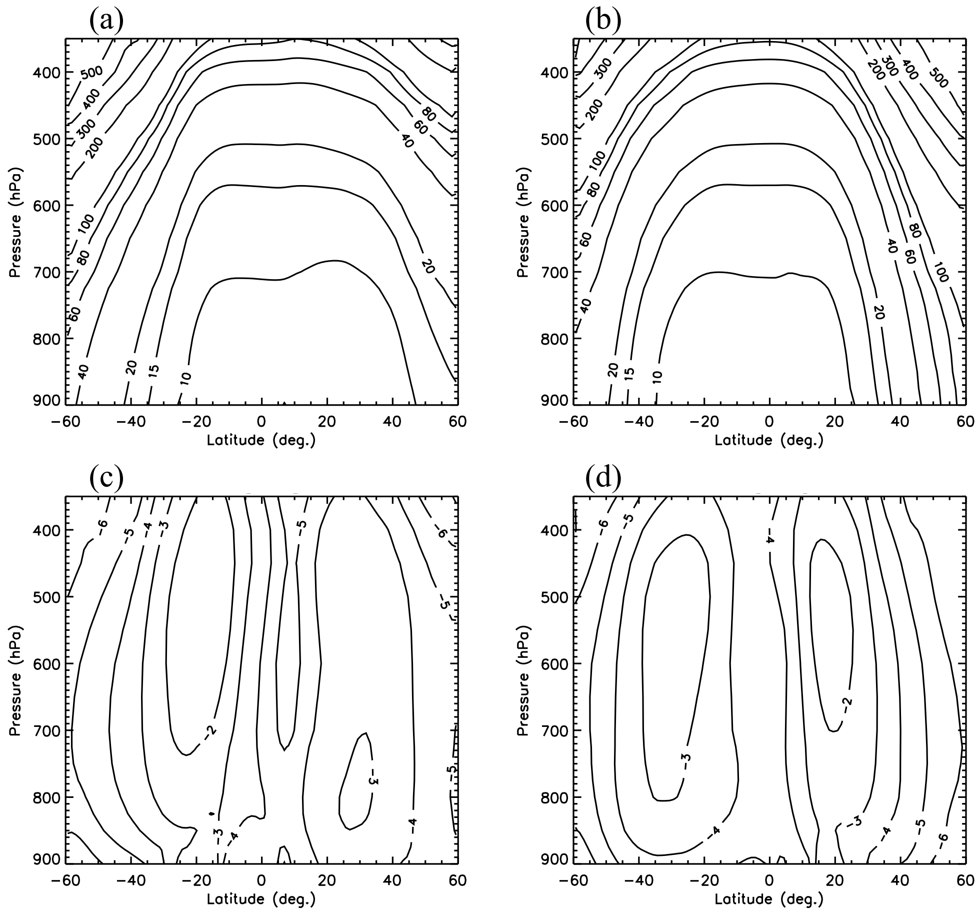

Figure 2.4: Long-term (1979-2004) zonal mean relative humidity conversion factors for moisture (f_q ; [%/(g/kg)]; a, b) and temperature (f_T ; [%/K]; c, d) tendencies derived from MERRA data for the DJF (left panels) and JJA (right panels) seasons. Contours for (a,b) are 0,5,…20,40,…100,200,…500%/(g/kg), while contour interval for (c,d) is 1%/K.

over the southern subtropics is required than over the northern subtropics to replicate the modeling results. Alternatively, given the similarity in winter versus summer hemispheric sensitivities to moisture changes (Figures 2.4a-b), changes in moistening processes over the southern subtropics could be implicated. This aspect is explored in Section 2.4.4 and 2.4.5, below.

The variations in *H* associated due to variation in *q* or *T* can be found by combining the f_T and f_q terms with the average *T* and *q* monthly standard deviations (σ_q and σ_T). This gives an expected range of regional forcing on *H* values due to independent changes in *q* or *T* (Figure 2.5), however, the results in Figures 2.5a-d should be taken with caution as they do not account for any covariance between *q* and *T*. Given that f_q and f_T are found as monthly means (i.e., constant), an approximation for the expected intraseasonal deviation of *H* is found as $f_q\sigma_q + f_T\sigma_T$ (note that $f_T < 0$) for comparison with the observed deviation of *H* (Figure 2.2). While this approximation accounts for some of the covariance between *T* and *q*, the intraseasonal covariance between f_q and f_T are not accounted for (discussed below).

The expected range of regional forcing on *H* values due to changes in *T* or *q* (Figure 2.5) increases sharply with increasing latitude at all levels poleward of 30º, especially in the winter hemisphere. This meridional gradient was not seen for the *q* standard deviation, and is strictly a result of f_q values, which increase sharply as temperature values fall. Near 500 hPa in the winter hemisphere, the effects on *H* are greater than 50% due to σ_q, and greater than 30% due to σ_T. This values fall within the baroclinic polar front zone, where exchanges between cold and dry arctic air with warmer, moist air of subtropical origin can lead to periodic storms (i.e., clouds) that are often followed by much colder and drier conditions. Although the more moist regions have greatest *H* sensitivity to potential perturbations in temperature, the temperature

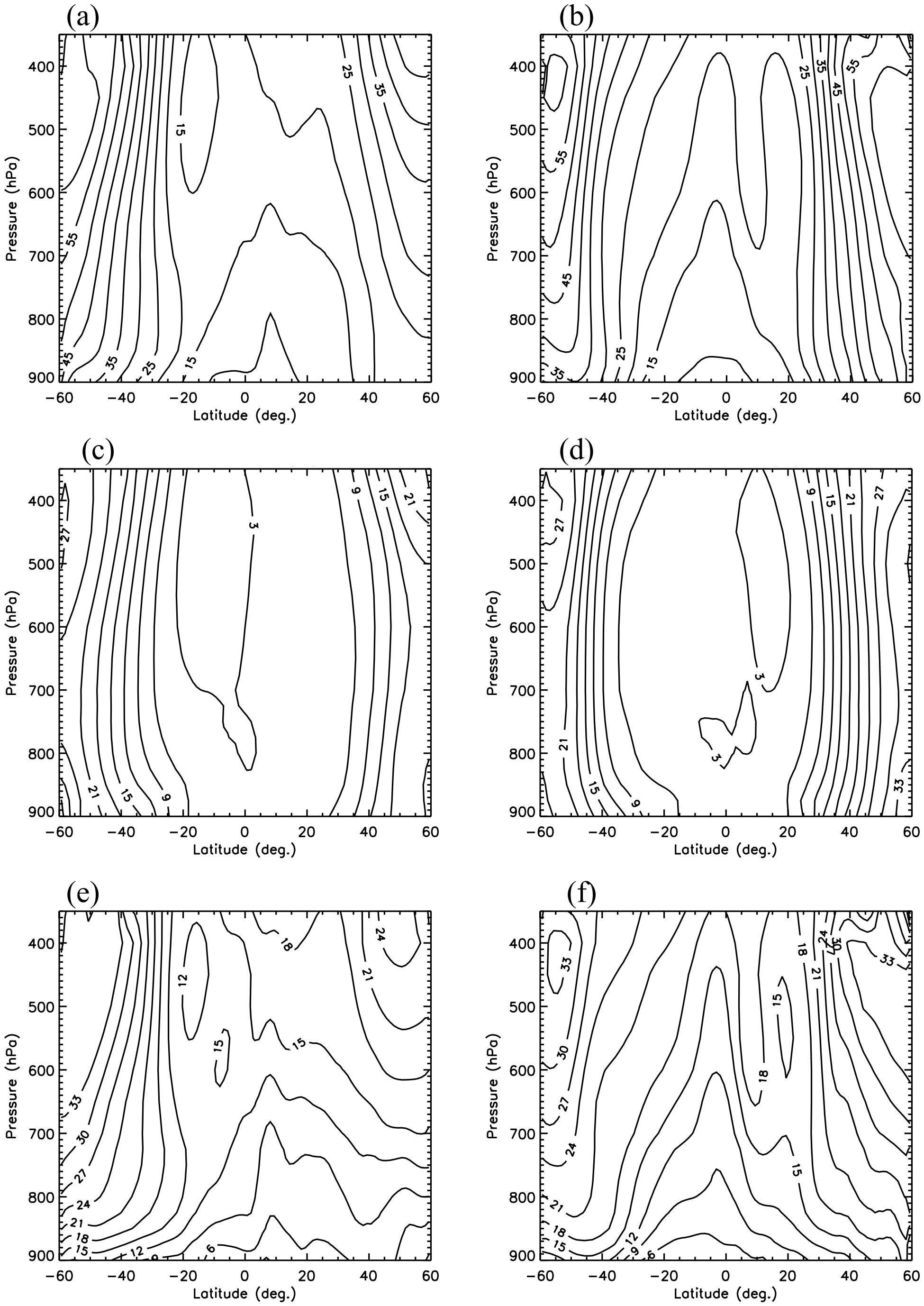

Figure 2.5: Average monthly standard deviation of q (σ_q ; a, b) and T (σ_T ; c, d) multiplied by absolute values of f_q and f_T, respectively, and $f_q\sigma_q$+ $f_T\sigma_T$ (e, f) for JJA (left panels) and DJF (right panels). Contour intervals: for (a,b) 5%; and, for (c,d,e,f) 3%.

perturbations in the warmest regions (i.e., the tropics) are generally smaller than those outside of that region. Thus, minima associated with q (Figure 2.5a-b) are found at 900 hPa in the tropics, where both f_q (Figures 2.4a-b) and monthly σ_q (Figures 2.2a-b), are low.

H variations related to T (Figures 2.5c-d) have minima in the subtropical dry zones (~500 hPa and ~15º-20º in the winter hemispheres), which is a direct result of the low regional H values (recall Figure 2.1a-b), which decrease the sensitivity of H to changes in temperature (Figures 2.4c-d). The higher H forcing values associated with T again fall in the baroclinic zone near 60º, where exchanges of arctic and subtropical air masses are commonplace. It is clear that from the analysis that the midlatitudes, subtropics, and tropical regions have varying characteristics in regional sensitivity of H to changes in T or q, in the average intraseasonal deviations of T and q, and in the expected intraseasonal changes in H due to these effects. Thus, these regions are considered separately in the analysis of the dynamical and diabatic tendencies of the temperature and moisture dependent relative humidity budget in the following sections.

The combined effects of T and q deviations on H (Figures 2.5e-f) show explicitly that deviations in q primary drive deviations in H on intraseasonal timescales (i.e., $f_q\sigma_q - f_T\sigma_T > 0$), in agreement with past work [*Peixoto and Oort*, 1996]. Differences between $f_q\sigma_q + f_T\sigma_T$ and σ_H (Figure 2.2) partially arise through the covariance of f_q and f_T, which is not accounted for here since these are taken as monthly means. Additionally, these differences may arise at lower levels since large-scale processes have been shown to very reasonably replicate atmospheric H above 700 hPa, while unresolved cumulus-scale effects are important drivers of H at lower levels [*Sherwood*, 1996]. Nonetheless, the comparisons agree to within 3% above 750 hPa, and to within 3-7% below 750 hPa, with the largest differences at 900 hPa. Thus, we will primarily focus on the mid-troposphere, where better agreement is found.

2.4.3 Total Divergence Calculation Validation

Six zonal regions are defined for study: the tropics, 0º-10º N and S; the subtropics, 15º-30º N and S; and the midlatitudes, 40º-60º N and S. Each region is examined during the DJF and JJA periods separately in order to expose hydrologic differences that arise due to seasonal variations in the strengths of monsoonal or baroclinic flow. Monthly mean advective T and q tendencies found from finite differencing on a sphere are compared with those calculated online in the MERRA; however, the results are multiplied by (the same) monthly mean f_q and f_T values to illustrate the regional H tendencies (Figure 2.6). Good agreement is found between our calculated total q divergence and those derived online in the MERRA, which results in agreement in total dynamical forcing on H from moisture divergence (green versus black lines in Figure 2.6). Some disagreement is seen above 500 hPa in the midlatitudes (~2-3%/day, Figures 2.6a-d), at 900 hPa in the subtropical winter plots (~3-6%/day Figures 2.6f-g), and at various levels in the tropics(~1-2%/day, Figures 2.6i-l), however these slight differences are at least an order of magnitude lower than those of the regional primary balancing components (see Section 2.4.4, below). These slight differences are solely a result of numerical artifacts that occur from post-processing the data offline in pressure coordinates versus processing the data online in model coordinates [*Trenberth et al.*, 2002].

Relative humidity statistics due to dynamical T tendencies found using finite differencing (red and blue lines in Figure 2.6) show less agreement with those in the MERRA monthly data archive. Prior work has shown even larger disagreements can occur due to cancellations of large opposing terms in the dry static energy budget [*Oort and Peixoto*, 1983; *Trenberth et al.*, 2002], however strict adherence to the hydrostatic equation in our code minimizes this effect. These

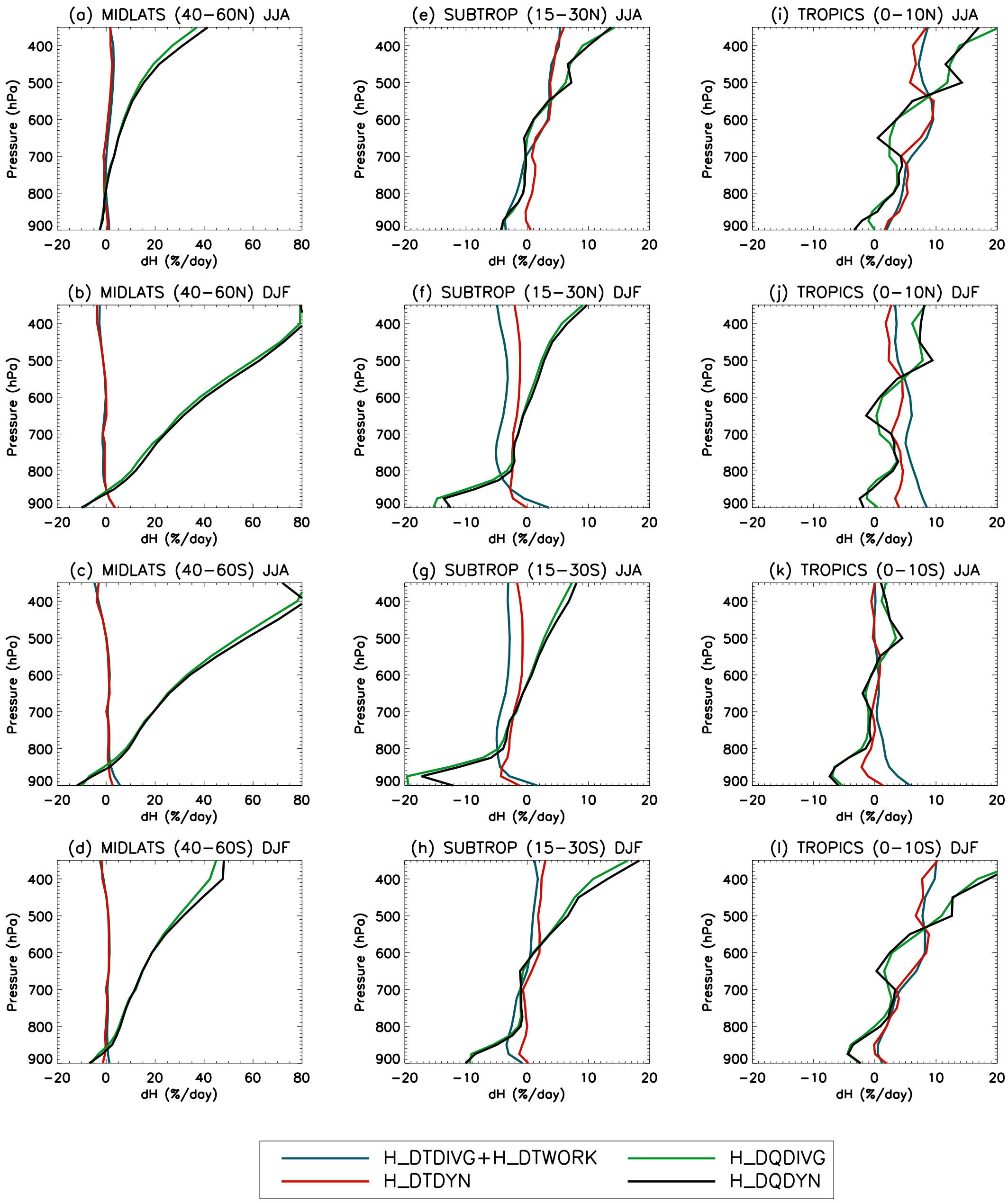

Figure 2.6: Comparison of finite difference calculations of seasonal mean relative humidity effects due to total dynamical moisture and temperature tendencies (green and blue lines, respectively) with those taken directly from the MERRA data archive [H_DQDYN (black) and H_DTDYN (red) lines, respectively). Evaluated are the midlatitude (40º-60º, left column), subtropical (15º-30º, center column), and tropical (0º-10º, right column) regions during JJA (first and third rows) and DJF (second and fourth rows). Note that the left column (midlatitude) x-axis scaling differs from that used in the center and right column panels.

differences are also partially attributed to the interpolation of the state variables from the GEOS-5 AGCM and Data Assimilation System (2/3º degrees longitude by 1/2º latitude with 72 hybrid levels, [*Rienecker et al.*, 2008]) to the more coarse grid of the MERRA daily output files (1.25º by 1.25º with 42 pressure levels). Nonetheless, the problem is limited to the subtropical and tropical regions during wintertime (Figures 2.6f-g and 2.6j-k), where offline versus online differences are reasonable (5%/day or less). We note that these differences are likely associated with numerical precision resulting from the divergence calculation in a region where spatial gradients in wind and temperature are weak.

Both calculations agree that the effects on *H* due to total moisture divergence increase with height, have maxima at 450 hPa in the midlatitudes, and have steeper vertical gradients in the summer versus wintertime in the subtropical and tropical regions. The vertical gradients in total temperature divergence are less steep than those of total moisture divergence, which was predicted in our standard deviation analysis (Figure 2.5). However, there are many dynamical components which make up the total divergence, and the magnitudes are those components are not restricted by the total divergence values. Deduction of the magnitudes, and overall balance, of these components is the focus of the remaining sections.

2.4.4 Moisture and Temperature Effects on Regional *H*

2.4.4.1 Calculation and Description

To evaluate the moisture processes that influence *H* in the Northern and Southern Hemisphere tropics, subtropics, and midlatitudes during different seasons, area-weighted monthly mean averages of several pertinent terms for DJF and JJA are taken for the respective hemispheres. Dynamical terms are calculated using finite differences on a sphere, while diabatic terms are taken directly from the MERRA monthly data archive. Differences in *H* from the *T* and *q* dynamic tendency calculations (i.e., Figure 2.6) are also shown in Figures 2.7-2.12 as H_DTDERR and H_DQDERR, respectively.

2.4.4.2 Midlatitude Regions

Area-weighted *H* tendencies in the midlatitudes due to moisture processes are shown in Figures 2.7. During both seasons, moisture-related *H* forcing above 700 hPa (Figures 2.7 a-d) is balanced by moisture convergence from transient eddies and dehydration via condensation. During periods of high baroclinicity (i.e., winter season, DJF for the NH and JJA for the SH), *H* forcing from transient eddy moisture convergence reaches levels greater than 70%/day at 500 hPa. Mid-latitude synoptic storms are found to be the strongest forcing mechanism on *H* out of all regions and seasons evaluated. 85% of the positive winter *H* forcing at 500 hPa comes from vertical eddy convergence (H_DWQTE), with the remainder from the meridional component (H_DVQTE). H_DVQTE is increasingly important to the overall moistening towards the lower levels, and is equal in magnitude to H_DWQTE at 700 hPa. H_DVQTE is barotropic-like, even though the vertical gradient in f_q ($1/q_s$) is steep in this region (Figure 2.4). There are little moistening effects from stationary eddies, except during the Northern Hemisphere winter, where the contribution to *H* total tendency is ~5%/day at upper levels. The lack of this effect in the SH winter is linked to the hemispheric asymmetry in stationary wave structure [*Solomon*, 1997], however, past work has shown stationary waves transport heat and moisture poleward of 60º S [*Kirk*, 1987]. At lower altitude (below 850 hPa level), positive *H* forcing due to turbulent

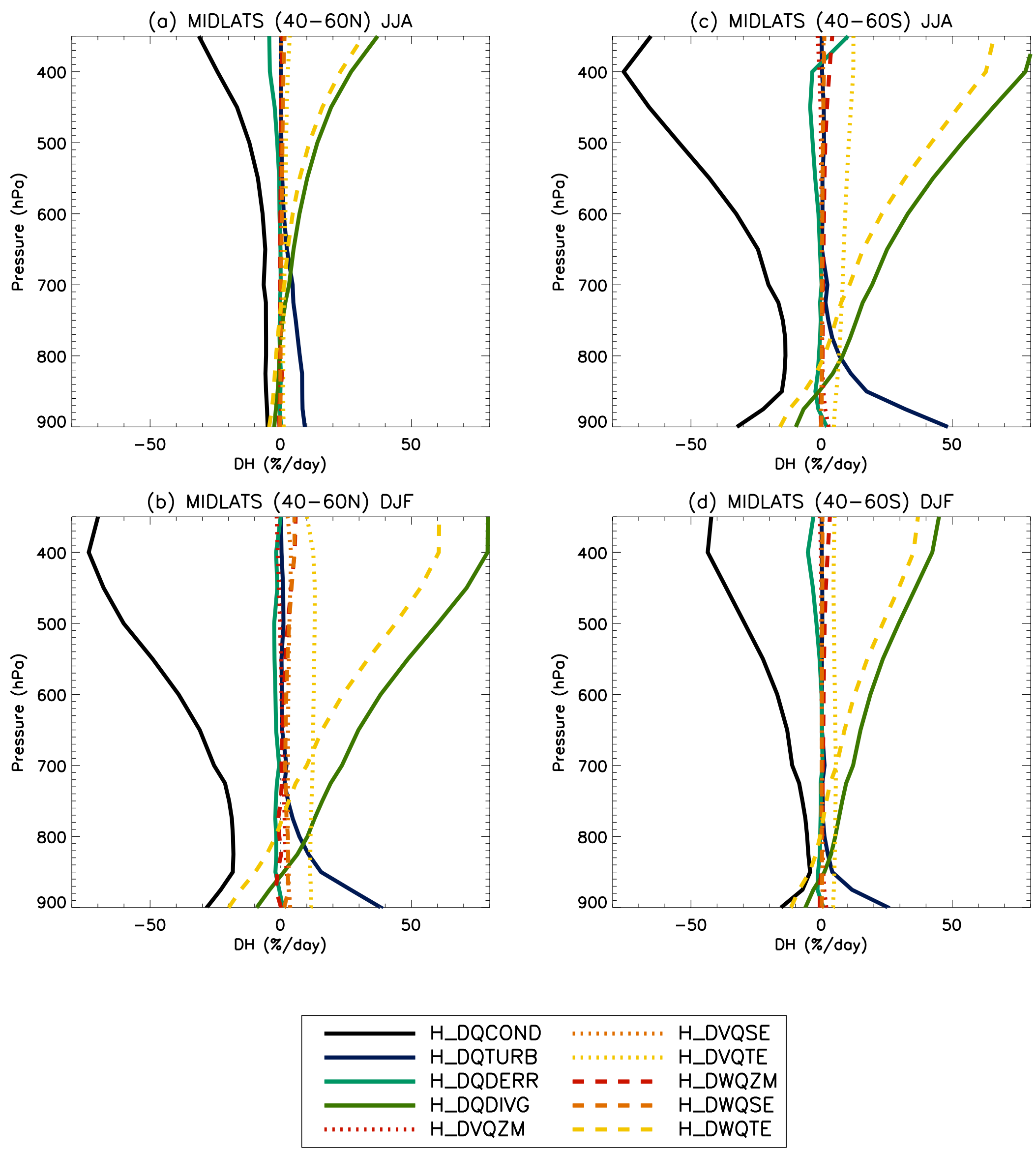

Figure 2.7: MERRA-derived long-term relative humidity tendencies due to moisture processes (Table 2.1) during June-July-August (a, c) and December-January-February (b, d) for the years 1979-2004. Regions shown are 40º-60ºN (a-b) and 40º-60ºS (c-d).

exchange (H_DQTURB; 40-45%/day winter and ~10-20%/day summer) tend to offset negative *H* forcing from condensation (i.e., boundary layer precipitation). However, during winter, eddies also play a role due to surface cold fronts and associated storms; vertical divergence in transient eddy flow contributes to the regional water sink (~30-40% of total), while meridional eddy convergence contributes to the regional water gain (5-20% of total).

Magnitudes of the *H* influences from temperature-related effects (5-10%/day; Figures 2.8) in the midlatitudes are much less than those found from the moisture budget (20-70 %/day; Figure 2.7). Note in Figure 2.8 that the overall budget is formed as follows (with the large-scale dynamical components on the left hand side), H_DTDIVG + H_DTWORK ≈ -(H_DTCOND + H_DTTURB + H_DTRADN), where the H_DTDIVG term is the summation of the six directional terms on the right side of the legend. A positive temperature change (e.g., from divergence, etc.) leads to a decrease in *H* values. At all levels, *H* decreases from latent heat release (H_DTCOND; ~10%/day at 900 hPa, decreasing to <5%/day at 500 hPa), while *H* increases from adiabatic expansion (H_DTWORK; 1%/day at 900 hPa, increasing to >5%/day at 500 hPa) and from radiative cooling (H_DTRADN; ~5-8% throughout the column). Adiabatic expansion is a strong component to the total dynamical forcing of *H*, however above 500 hPa its influence is entirely offset, or exceeded, by heat convergence occurring with the vertical mean flow (H_DWTZM; 2-3%/day) and transient eddies (H_DWTTE; 2-5%/day). As shown in the moisture budget, the transient eddies are most active during winter. At lower levels (~900 hPa) in the winter hemispheres (Figures 2.8b-c), vertical heat divergence by transient eddies tends to raise *H* values, while meridional heat convergence by transient eddies and vertical heat convergence by stationary eddies tend to decrease *H*. Turbulence also plays a role, and generally causes increases in *H* at the 900 hPa level (H_DTTURB≈2-4%/day) as it describes the mixing of

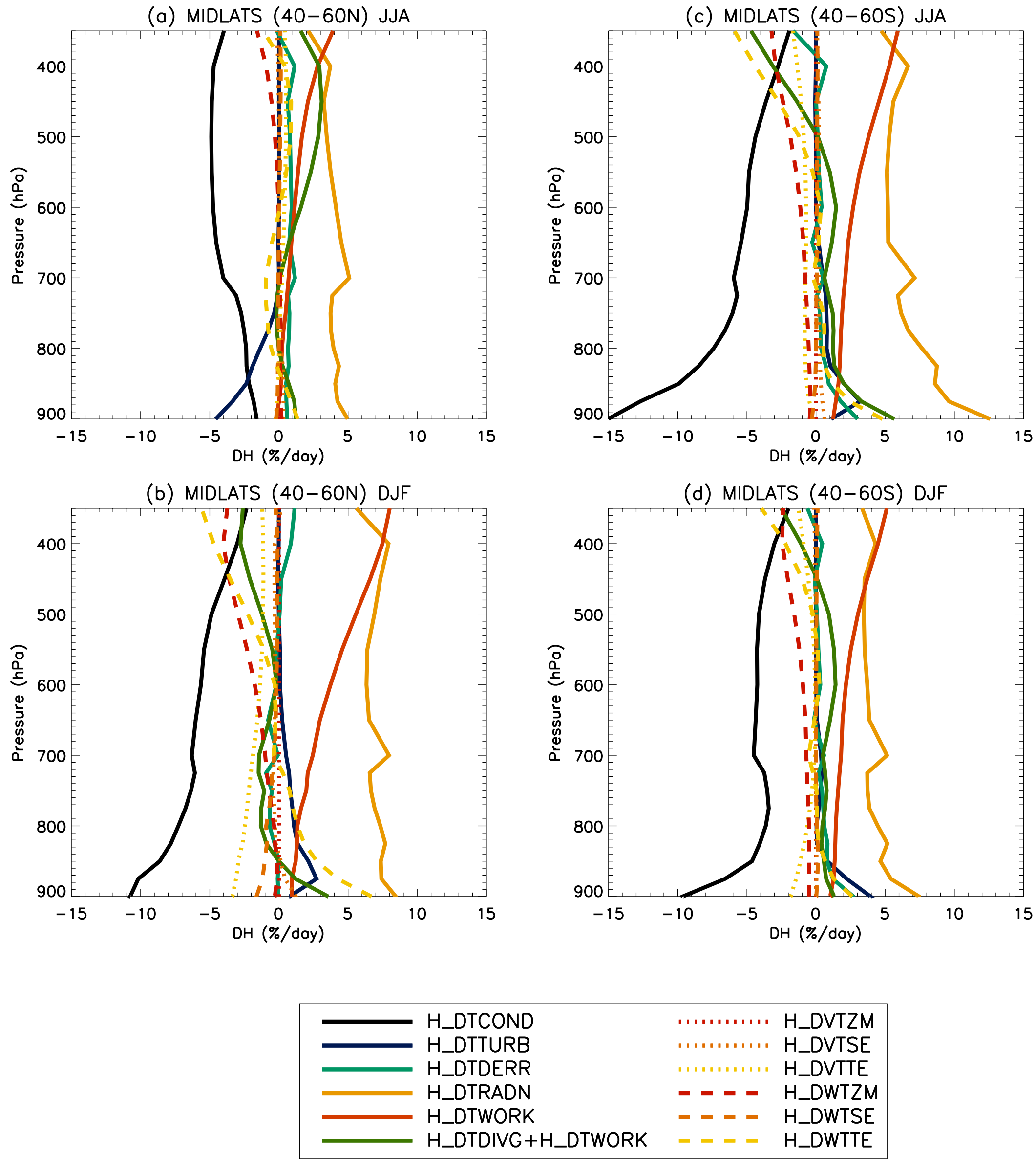

Figure 2.8: MERRA-derived long-term relative humidity tendencies due to temperature related processes (Table 2.1) during June-July-August (a, c) and December-January-February (b, d) for the years 1979-2004. Regions shown are 40º-60ºN (a-b) and 40º-60ºS (c-d).

the free atmosphere (colder) air with that at the top of the boundary layer (i.e., cooling). Below 900 hPa (not shown), this term is negative (i.e., sensible heat flux from the surface acts to decrease *H*). Since the boundary layer is higher during JJA in the NH, turbulence causes warming at 900 hPa. Although there are complex relationships within the heat budget, the overall balance of *H* is primarily maintained by the moisture budget in this region during all seasons.

2.4.4.3 Subtropical Regions

The primary difference between the subtropical *H* tendencies associated with the moisture balance (Figure 2.9), and that in the midlatitudes, is the smaller magnitude of *H* forcing by vertical divergence via transient eddies (a six-fold difference during winter, and a three-fold difference during summer). The dynamical terms in Figure 2.9 show that positive forcing on *H* from 600-350 hPa in the subtropics during the hemispheric winters (Figures 2.9 b-c) is largely achieved through moisture convergence associated with the vertical component of transient (4-7%/day) and stationary (~2%/day) eddies, which is slightly counteracted by moisture divergence in the vertical mean flow (3-5%/day). These results agree with past work [focused on a single season (1998/1999)] that found the vertical convergence of water vapor by eddies moisten the subtropical *H* minimum during DJF in the SH [*Couhert et al.*, 2010]. However, modeling studies have found decreasing moisture convergence via transient eddy activity on the poleward edge of the subtropical zones may, over time, act to expand the subtropical dry zone (e.g., *Seager et al.* [2010]). We find drying by divergence within the mean vertical flow counteracts some of the moistening introduced by transient eddies during the hemispheric winter (which is notably absent during the summers), and thus a trend on this term could produce the same result. Evaluation of

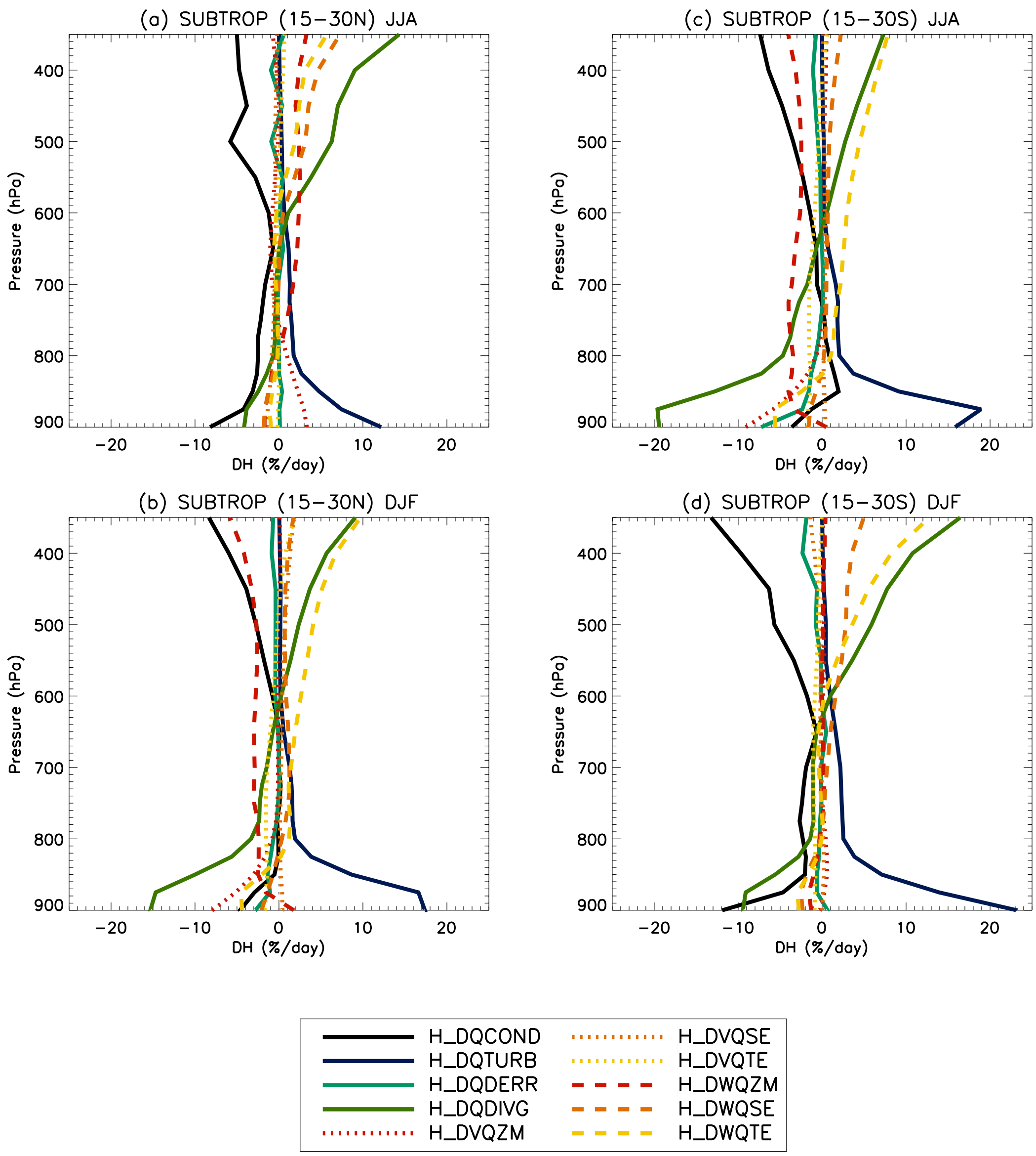

Figure 2.9: As in Figure 2.7, but for the subtropical regions (15º-30º).

significant 26 year trends of the relevant processes is performed in 2.4.5 to address this question.

At low levels (below 700 hPa) during winter (Figures 2.9b-c), moisture divergence by mean, stationary, and transient eddy flow combine to create strong negative *H* forcing of ~10-20%/day, with the largest values found near 900 hPa. This drying process is balanced by turbulent gains of surface-derived moisture near the top of the planetary boundary layer (~15%/day). The near-surface balance is different during summertime, with approximately equal drying effects from condensation (~10%/day) and moisture divergence (5-10%/day) that oppose turbulent moisture gains (~20%/day). The NH summer (Figure 2.9a) shows low level moisture convergence associated with mean meridional flow (~3%/day), which is likely influenced by the seasonal monsoons (e.g., the Asian Monsoon and the North American Monsoon).

Results from the wintertime temperature budget (Figures 2.10b-c) show that heating adiabatic compression dries the atmospheric column (5-8%/day) in both hemispheres. The wintertime subsidence, associated with vertical mean flow (not shown separately, but calculated as $\kappa[\overline{\omega}][\overline{T}]/p$), is approximately balanced by the divergence of heat within this flow (H_DWTZM, dashed red line) above 750 hPa. Closer to the planetary boundary layer, wintertime heat divergence by transient eddies and the meridional mean flow counteract heat convergence by the vertical mean flow, with radiation from the trade wind inversion cooling (and raising *H*) and latent heat release from boundary layer clouds bringing *H* values down.

The subtropical *H* budget during summertime (Figures 2.10a and 2.10d) is notably different than during winter; forcing by the adiabatic component reverses sign, and now acts to raise regional *H* as air rises and cools (5-15%/day). Additionally, above 700 hPa, heat release from condensation is an important component that lowers *H* values (5-10%/day). Thus, the effects of storms along the ITCZ, and others convective areas forced by maximum yearly surface

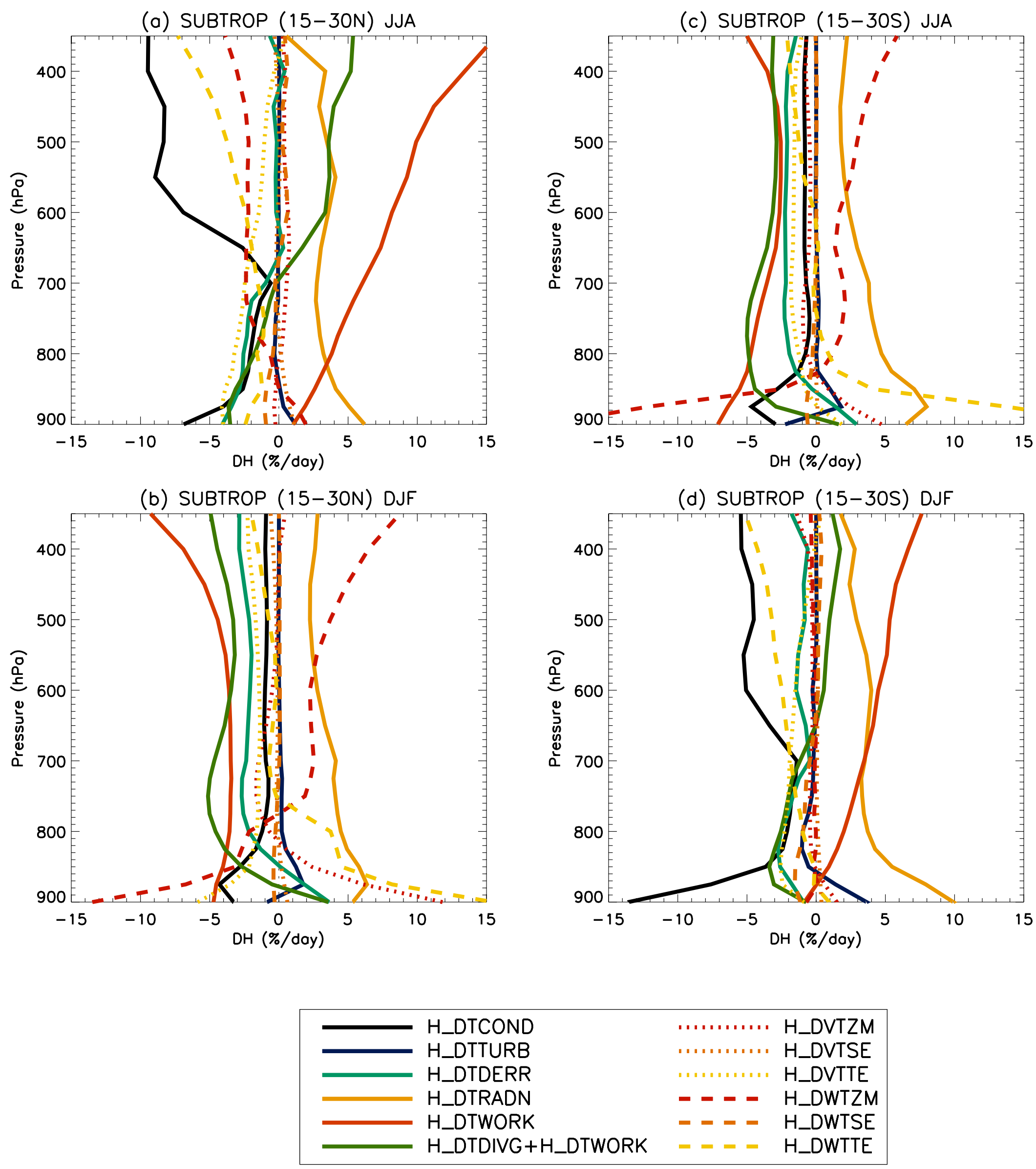

Figure 2.10: As in Figure 2.8, but for the subtropical regions (15º-30º).

heating (i.e., monsoonal areas) are captured here. The summertime subtropics also show vertical heat convergence associated with transient eddies (H_DWTTE; 2-7%/day) act to reduce the *H* increases from adiabatic expansion, with a smaller contribution from vertical divergence of the mean flow (H_DWTZM; 2-4%/day) in the NH.

2.4.4.4 Tropical Regions

In the tropical regions, summertime moisture budget results (Figures 2.11a and 2.11d) show *H* values are increasingly forced up with height via moisture converging within the vertical mean flow (from 1%/day at 800 hPa to 10%/day at 350 hPa), with transient and stationary eddies also contributing to this rise (5-6%/day at 350 hPa). The stationary eddy component is likely related to 30-100 day period of the Madden-Julian Oscillation [*Zhang*, 2005], since the divergence calculations here are calculated in six-hourly intervals over a month's time. Large-scale condensation balances these moistening effects above 650 hPa. Below 800 hPa, condensation balances *H* increases from turbulent gains of moisture and meridional moisture convergence within the mean flow (i.e., tradewind convergence). The results depict the classical monsoonal and convective flow near the ITCZ, which is characterized by a mix of shallow and deeper convection with maximum condensational effects above 500 hPa.

The *q* budget for the wintertime tropics (Figures 2.11b-c) exhibit greater hemispheric asymmetry, which is related to the average position of the ITCZ tending towards the NH. This comes about from increased land surface in the NH, which shifts the meridional position of maximum global heating. Thus, the NH hemisphere winter results resemble those of the tropical

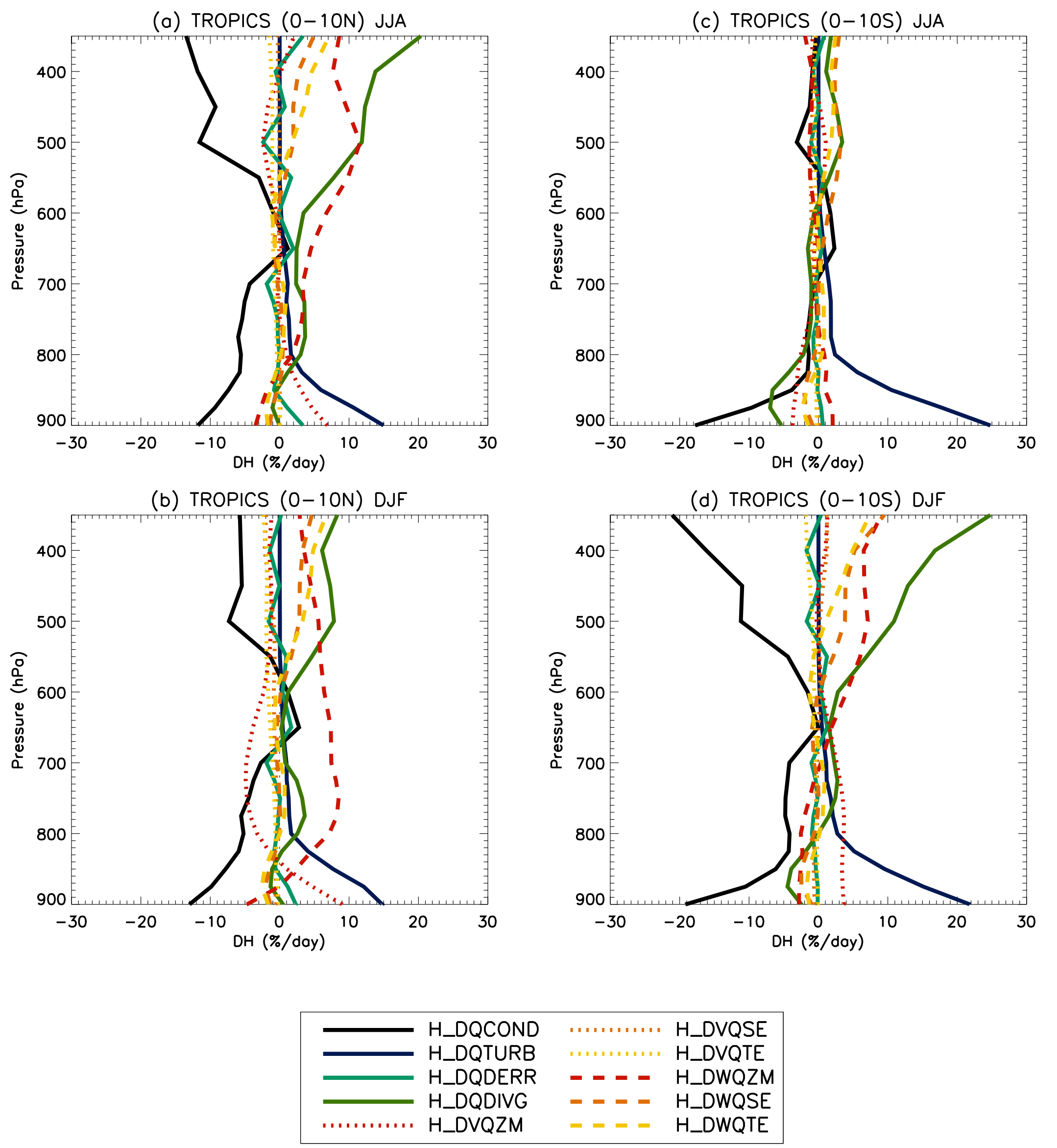

Figure 2.11: As in Figure 2.7, but for the tropical regions (0º-10º).

hemispheric summers, with some reduction in *H* decreases due to less condensation at upper levels. The SH tropical region during JJA is far enough removed from the maximum heating and monsoonal convection as to show similar (yet muted) characteristics of the subtropical regions during winter.

In general, temperature effects on the tropical summertime *H* budget (Figures 2.12) above 750 hPa describes the ascending branch of the Hadley Cell; a balance of *H* losses via latent heat release versus *H* gains via adiabatic expansion. Vertical heat divergence associated with the mean flow (~5-10%/day) and transient eddies (~5-10%/day) counteracts some of the *H* increases due to adiabatic expansion (5%/day at 900 hPa and 25-30%/day at 350 hPa). The widespread effect of convection, mean ascent, and condensation by seasonal monsoons is clearly seen by comparing the primary *H* forcing components in the summertime tropical (Figures 2.11-2.12) and subtropical calculations (2.9-2.10). The vertical distribution of the components are quite similar between regions, with the individual components having smaller magnitudes in the subtropics.

The NH wintertime results for the tropics (Figures 2.12b) are similar to those for the summertime albeit with less condensation and adiabatic expansion forcing on *H*. The SH wintertime results (Figure 2.12c) vary from the summertime results in that drying by condensation is more present at the boundary layer top (i.e. shallow convection). We note that the hemispheric differences in tropical wintertime *H* forcings are largely the result of differing distances from the position of the ITCZ (i.e. the NH tropical box incorporates more of the ITCZ convection). The *H* budget in the tropics is primarily dependent on upward, large-scale convection, however, tropical eddies are active and are found to add heat and moisture above 700 hPa and to add heat below 800 hPa.

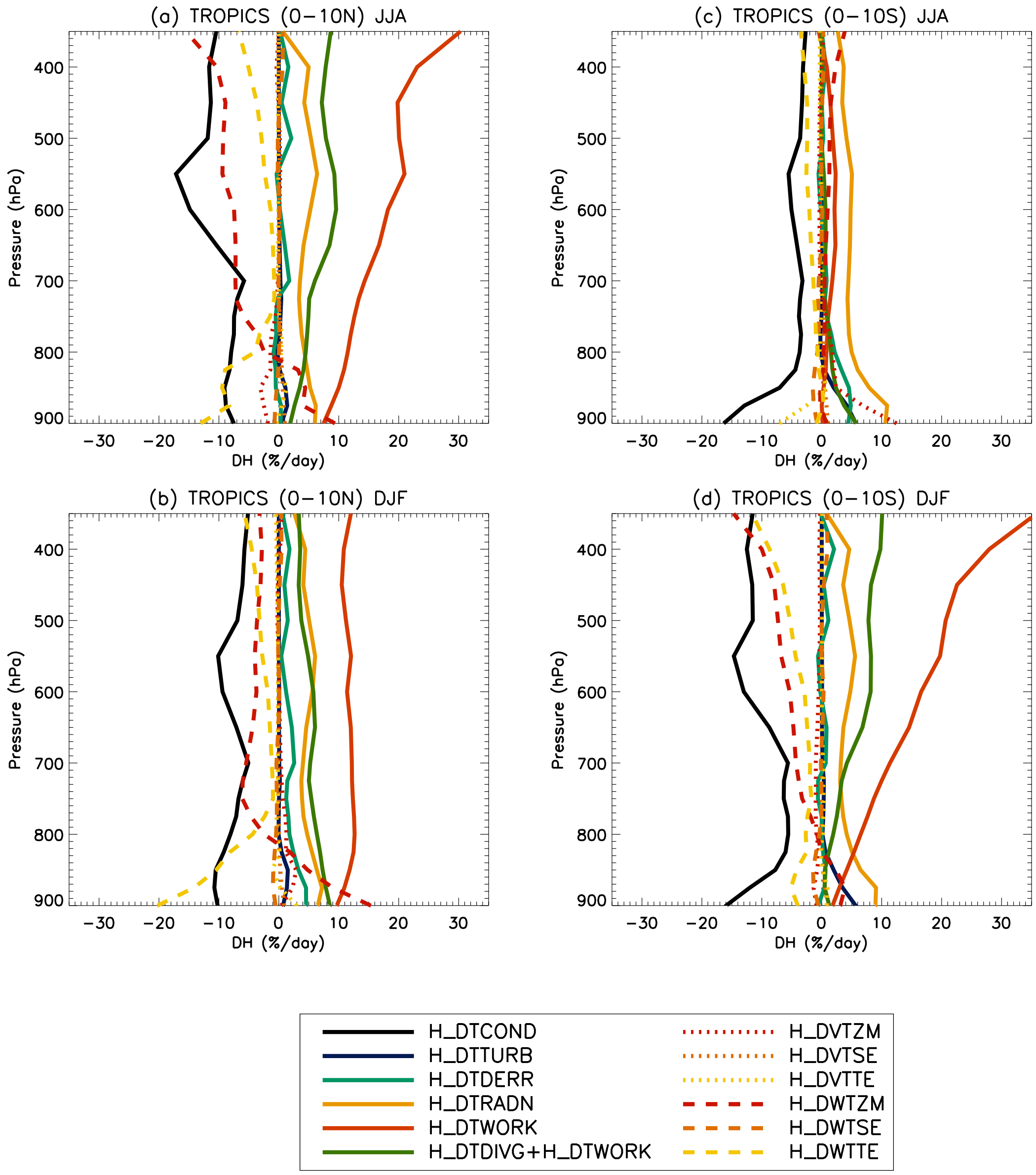

Figure 2.12: As in Figure 2.8, but for the tropical regions (0º-10º).

2.4.5 26 Year Trends in Key Subtropical *H* Forcing Components

Having established the balances in influential processes on regional *H*, significant long-term trends of components influencing the *H* budget are evaluated for the midpoint of atmospheric mass (500 hPa) in the subtropics and in a zone spanning the subtropic and midlatitude borders (30º-45º N/S). These regions are chosen as a focal point for several reasons: relative changes in water vapor concentration are large due to the dry air, and exert substantial variability on climate feedbacks [*Pierrehumbert*, 1999]; the factors which influence *H* vary significantly with season [*Couhert et al.*, 2010]; several modeling studies suggest that changes in atmospheric circulation, and not thermodynamics, exert control over subtropical *H* values [*Galewsky et al.*, 2005; *Galewsky and Hurley*, 2010; *Hurley and Galewsky*, 2010a; *Wright et al.*, 2010]; and lastly, GCM studies have indicated a future widening of the subtropical dry zone in response in global warming as well an increase in moisture convergence poleward of ~40º [*Seager et al.*, 2010; *Wright et al.*, 2010].

In the MERRA dataset, over the subtropics (15º-30º), there are no significant long-term trends in *H* from 1979-2004 during DJF or JJA in the southern or northern hemisphere, yet the primary balancing components do shift significantly in magnitude (Figure 2.13). No significant trends in any processes were found over 15º-30º S during JJA (Figure 2.13d). There are clear oscillations for each term that are likely associated with year-to-year shifts in the atmospheric circulation (e.g., from variations in ENSO), however, the primary focus here is the significant long-term changes in important terms.

For the northern hemisphere, during winter (DJF, Figure 2.13a), the influence of adiabatic compression on decreasing *H* (H_DTWORK) has increased over time

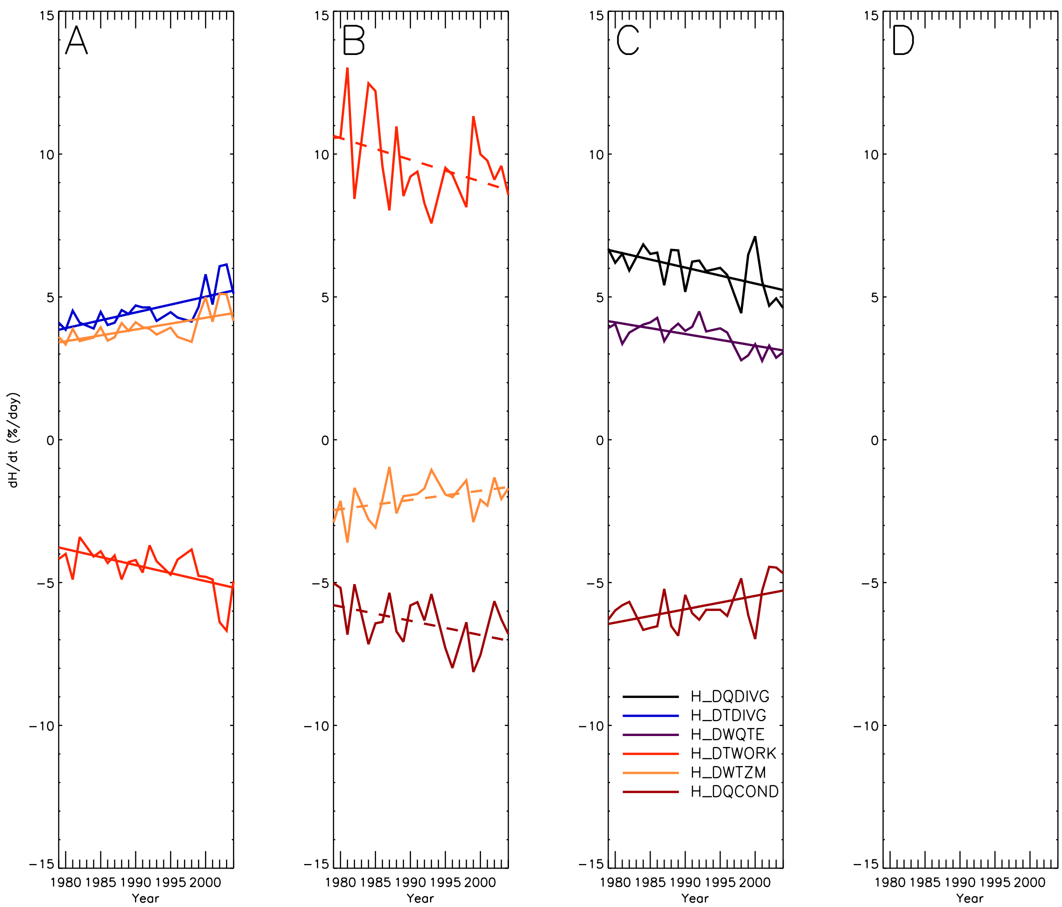

Figure 2.13: Significant trends from 1979-2004 in processes (see legend) that influence the relative humidity budget at 500 hPa from 15º-30º N during DJF (a) and JJA (b), and from 15º-30º S during DJF (c) and JJA (d; no trends found). Solid regression lines indicate statistical significance at the 99% confidence interval (p<.01) while dashed lines indicate 95% confidence (p<.05). Only those processes which have statistically significant trends, and have changed by more than 1%/day over the 26 year period are shown.

[(-0.056 %/day)/year], with a complementary effect from increasing heat divergence within the vertical mean flow [H_DWTZM; (0.41 %/day)/year]. Note that these components were found to be of primary importance to the temperature terms in the *H* balance (Figure 2.9), with each having approximately equal magnitude (~5%/day) to the important moisture components (i.e., condensation and transient eddy moisture convergence; Figure 2.8). The increased effect of subsidence over time in this zone is strong evidence for a strengthening of the descending branch of the Hadley Cell, however, these effect is found here to be balanced over the long-term yield an approximately constant *H*.

The northern hemisphere summer (Figure 2.13b) has three terms with significant trends ($p<0.05$): the magnitude of the humidity tendency due to adiabatic expansion effects is decreasing, the magnitude of the humidity tendency due to condensation effects is increasing (i.e., more negative), and the magnitude of the humidity tendency due to heat convergence effects is decreasing. This suggests a shift in the atmospheric circulation, in that condensation is intensifying as a result of less efficient heating convergence from the mean flow, even though the strength of the mean isentropic uplift is decreasing. Given the northward position of the ITCZ during boreal summer and the well-documented influence of ENSO on the characteristics of the ITCZ (e.g., [*Munnich and Neelin*, 2005]), the large periodic oscillations in the terms over the northern hemisphere (especially H_DTWORK) are likely influenced by these shifts. Indeed, removing the long-term trends, correlations of H_DTWORK with the Multivariate ENSO Index (MEI, [*Wolter and Timlin*, 1998]) yield significant values of 0.44 for NH JJA from 15º-30º and -0.51 from 30º-45º, which indicates that ENSO has a powerful influence on regional subsidence.

The SH hemisphere subtropical summer (Figure 2.13c) shows decreasing effects on *H* resulting from decreases in transient eddy moisture flux divergence (H_DWQTE), with a subsequent reduction in condensation. Given the tendency of the ITCZ to stay close to the equator during austral summer (i.e., away from this zone), this result agrees with work by Seager et al. [2010], that found moisture convergence via transient eddy activity decreasing in time in the dry subtropical zones. We note that *H* effects from subsidence in this region show influence from ENSO [r(H_DTWORK, MEI)=-0.67], but that there is no significant long-term trend in H_DTWORK for subtropical austral summer.

The trends over the 30º-45º latitudinal bands (Figure 2.14) are generally more related to moisture effects than to temperature, and it was shown moisture convergence is quite strong from 40º-60º (Figure 2.7). A strong increase in moisture divergence associated with transient eddies during the boreal [(0.19%/day)/year] and austral [(0.17%/day)/year] winters is seen in Figures 2.14a and 2.14d, respectively, with a compensating effect from condensation. This strengthening of the hydrological cycle over time in the midlatitudes from increased eddy convergence has been found using predictive models [*Seager et al.*, 2010], and has been explained, in a global warming scenario, by simple thermodynamics according to the Clausius–Clapeyron relation [*Held and Soden*, 2006]. While *T* does not significantly increase in the MERRA data at 500 hPa, *q* does for both hemispheric winters from 30º-45º. In addition, *H* increases (by ~1% over the 26 years) over time for austral winter. During summer (Figures 2.14b-c), both hemispheres show slight decreases in moistening effects from transient eddies over time at 500 hPa, which have compensating effects since *H* does not significant change over time. Notably, the hydrological cycle is weakening (i.e., decreasing eddy moisture convergence and associated precipitation) more so in the SH summer from 15º-45º at 500 hPa (Figures 2.13c and 2.14c) than in the NH. This is in broad agreement with modeling studies that show

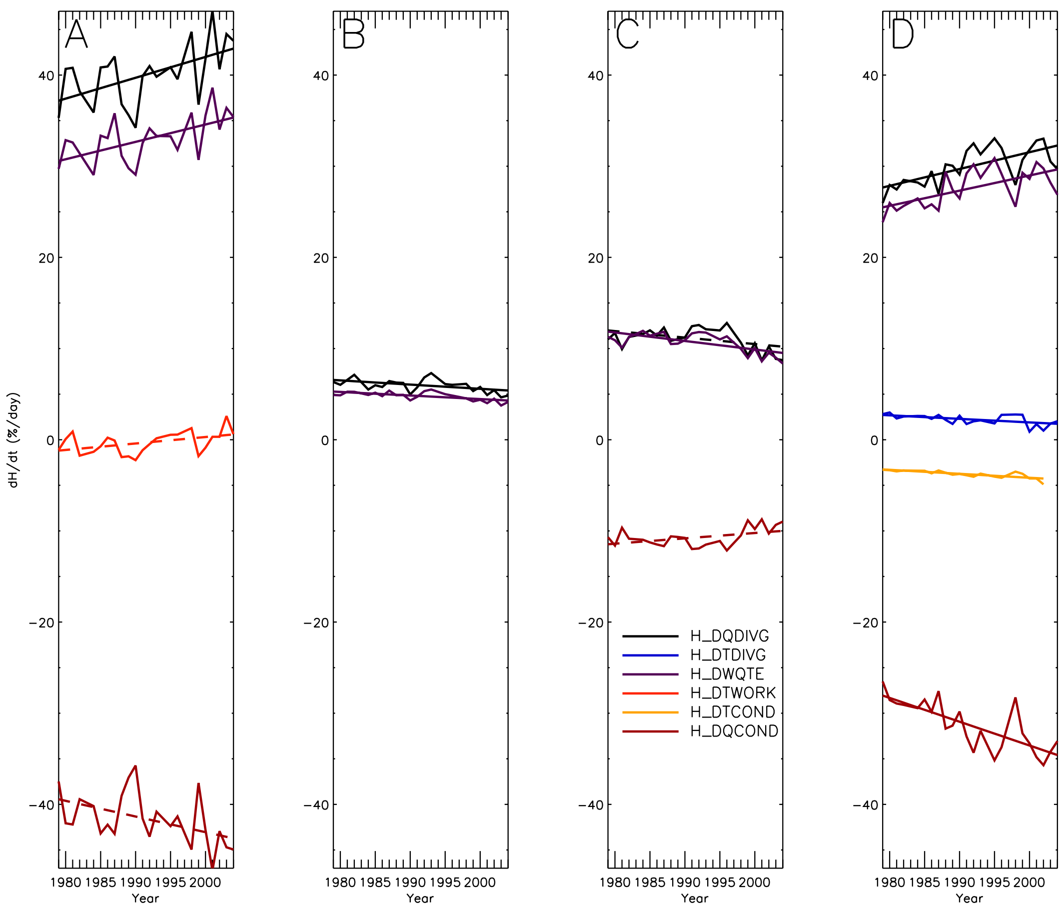

Figure 2.14: Significant trends from 1979-2004 in processes (see legend) that influence the relative humidity budget at 500 hPa from 30º-45º N during DJF (a) and JJA (b), and from 15º-30º S during DJF (c) and JJA (d). Solid regression lines indicate statistical significance at the 99% confidence interval (p<.01) while dashed lines indicate 95% confidence (p<.05). Only those processes which have statistically significant trends, and have changed by more than 1%/day over the 26 year period are shown.

hemispheric asymmetry in hydrologic changes with global climate change [*Mitchell and Ingram*, 1992; *Lorenz and DeWeaver*, 2007; *Sherwood et al.*, 2010a; *Wright et al.*, 2010].

2.5 Conclusions

From the newly available MERRA dataset, intraseasonal variations of q and H are an order of magnitude larger than year-to-year deviations due to frequent air mass exchanges and weather disturbances. From 900-350 hPa and 60º S to 60 º N, intraseasonal deviations in H were found to be more closely linked to deviations in q than to those in T, in agreement with past work [*Peixoto and Oort*, 1996]. The sensitivity of H to changes in q or T increases with latitude and with altitude, with lowest sensitivity to changes in T in the subtropical dry zones, and with lowest sensitivity to changes in q in the near-surface tropics. We find H in the baroclinic zone in the midlatitudes (700-400 hPa, poleward of 45º) is the most sensitive to changes in T and q, and additionally note that intraseasonal deviations of q and T are greatest in this region. Combining the intraseasonal deviations of q and T with monthly mean calculations of H sensitivity to such changes (i.e., f_q and f_T) agrees to within 3% with the true variations in H above 750 hPa.

From 1979-2004, different processes act to balance relative humidity for each region:

<u>Midlatitudes</u>: upper level moisture convergence from transient eddies balances condensation effects, while at lower levels condensation within boundary layer clouds balance turbulent moisture gains. Eddies bring heat in and dry at high levels, while removing heat and raising H at low levels during winter. At all levels, latent heat release acts to lower H, and is held in balance by radiational cooling and adiabatic expansion.

Subtropics: upper level moisture convergence by transient and stationary eddies increase *H*, which is offset by condensation and also by moisture divergence in the mean flow during winter. At low levels, moisture gains from turbulence are offset by drying from moisture divergence during winter and by condensation within boundary layer clouds during summer. The heat budget during summer shows the *H* values increase from adiabatic expansion and radiative cooling, yet decrease from latent heat release and heat convergence by transient eddies.

Tropics: During austral summer and boreal summer/winter, condensation at low and high levels reduce *H*. At upper levels, moisture convergence within stationary and transient eddies, as well as within mean flow, balance these increases while below 800 hPa the balance is achieved through turbulent gains of moisture. The heat budget shows *H* increases from adiabatic expansion and decreases from latent heat release, with heat gains by transient eddies and the mean flow always acting to decrease regional *H*.

These results agree with past work that found the vertical convergence of water vapor by eddies moisten the subtropical *H* minimum (~500 hPa) [*Couhert et al.*, 2010]. Indeed, transient eddies are active in all regions. They add heat and moisture in the mid to upper troposphere in most regions, while eddies in the midlatitudes remove moisture and heat at low levels. While the effects of transient eddy moisture and heat convergence tend to have counteracting effects on subtropical and tropical *H* values, the influence on *H* from transient eddy moisture convergence in the midlatitudes are not balanced heat convergence associated with eddies or with the mean flow. Instead, this moistening leads to precipitation, and thus eddies drive the midlatitude tropospheric hydrological cycle.

While relative humidity is held in approximate balance by different components for each region, the magnitude of the components are changing with time. In the NH subtropics during winter, increased subsidence over time is being held in balance by increasing heat divergence. During NH summer, condensation is decreasing in relation to decreasing eddy moisture convergence. The 30º-45º latitudinal band in both hemisphere shows that the wintertime hydrological cycle is strengthening, while this cycle appears to be weakening during summer over a large portion of the SH (15º-45º). Although there is no significant trend in *H* from 1979-2004 over most of the regions shown (1% increase for JJA 30º-45º S), it is clear that the balancing components are not static over time, and that the components that are changing vary between regions and seasons. Quantifying the influence of large-scale processes on the relative humidity budget, and their changes in time, increases our understanding of how the atmosphere may adjust to future modifications of climate, while increasing awareness of the changes in climate currently underway.

An important result from this analysis is that on intraseasonal timescales, changes in moisture primarily drive changes in relative humidity. While analysis of the large-scale circulation has been shown to provide reasonable estimates of observed relative humidity above 700 hPa (±10%, [*Sherwood*, 1996]), it remains unclear which combination of processes control relative humidity lower in the atmosphere, where smaller-scale events become important. Thus, further characterization of small-scale moistening processes, and their link to large-scale humidity, can provide a valuable contribution to this field. To this end, the information provided by the isotopic composition of water vapor has the potential to cast new light on the nature of atmospheric moistening because the different processes that underlie the moisture budget also imprint signals on the isotopic composition. The additional information provided by isotopic ratios in water vapor is exploited in the remainder of this thesis to resolve moistening processes that aren't straightforward to determine using non-isotopic methods.

3 Chapter 3

Comparison of Atmospheric Hydrology Over Convective Continental Regions Using Water Vapor Isotope Measurements From Space

3.1 Abstract

Global measurements of the 500-825 hPa layer mean HDO/H_2O ratio from the Tropospheric Emission Spectrometer (TES) are used to expose differences in the dominant hydrologic processes in the Amazon, north Australian, and Asian monsoon regions. The data show high regional isotopic variability and numerous values unexpected from classical Rayleigh theory. Correlation analysis shows that mixing with boundary layer air, enhanced isotopic fractionation during precipitation, and subsiding air parcels contribute to intra-seasonal isotopic variability. These local controls explain only 8-30% of total regional variance, which suggests that the isotopes are primarily indicators of moist processes that occur upstream. Seasonal trajectory analysis shows that Rayleigh distillation in a Lagrangrian framework underestimates the observed isotopic depletion during the monsoons, and suggests substantial recycling of water within or below clouds. The trajectory results for the dry seasons reveal that subsiding air parcels periodically introduce isotopically depleted air into the north Australia and Asian monsoon regions, whereas vigorous low-level convection over the Amazon basin acts to quickly enrich and moisten dry subsiding air. The analysis shows variations in the strength of convective detrainment into the lower to mid-troposphere over all regions, which, during the dry seasons of the north Australian and Asian monsoon regions, correlate with increases in relative humidity. This study shows that isotopic measurements provide unique diagnostics of mechanisms that

control the seasonal sources of water, and that these provide a refined understanding of the differences in the characteristics of hydrologic budgets in these monsoonal regions.

3.2 Introduction

The hydrologic regimes of the monsoonal regions of South East Asia, South America and Northern Australia reflect a complex balance of large-scale advective supply of water, surface exchange, and atmospheric condensation, which are important for the regional energy balance and climate [*Salati and Vose*, 1984; *Martinelli et al*., 1996; *Malhi*, *et al*., 2002; *Fu and Li*, 2004; *Sengupta and Sarkar*, 2006; *Juarez et al*., 2007; *Tian et al.*, 2007]. For these regions, the transfers of heat and moisture from the land surface to the atmosphere are substantial, yet these mechanisms are poorly resolved in current land-atmosphere models [*Dirmeyer et al*., 2006]. There is a need to further understand the seasonal variations in the sources of moisture over monsoonal regions to better constrain the surface water budget, identify the fate of precipitation, and establish the relationship between runoff, evapotranspiration, and the recycling of rainfall by cloud processes [*Henderson-Sellers et al*., 2004; *McGuffie and Henderson-Sellers*, 2004].

Measurements of water isotopes are useful for analyzing the sources and history of moisture because the lighter isotopes of water (e.g., H_2O) preferentially evaporate over heavier isotopes of water (e.g., HDO or $H_2^{18}O$), and heavier isotopes preferentially condense. Furthermore, the isotopic composition of ocean waters, and hence the vapor immediately evaporated from the ocean is well known; consequently, comparison of measured isotopic values of moisture with respect to oceanic values can be used to identify fresh vapor versus vapor that has a history of condensation. For example, Dansgaard [1964] and Gat [1996] showed that as oceanic air is advected away from the primary moisture source, isotopic fractionation during condensation causes precipitation to become depleted with respect to the deuterium content. This mechanism (hereafter Rayleigh model) leads to stronger isotopic depletion with higher latitude, altitude, and distance from coast. This model has been successful in explaining high latitude precipitation and also has provided useful insight into prior climatic temperature variations [*Dansgaard*, 1964; *Jouzel et al*., 2003; *Blunier et al.*, 2004; *Fricke and Wing*, 2004]. However, it is not clear if the Rayleigh model is generally appropriate for studies using high frequency (event-based) measurements, nor is it clear if the model is appropriate for explaining the isotopic composition of tropical vapor and precipitation over monsoonal regions.

Over monsoonal regions, precipitation rates and monsoonal circulation patterns are thought to be the dominant controls on the seasonal isotopic composition of water vapor and rainfall [*Hoffman*, 2003]. For example, using the International Atomic Energy Agency Global Network for Isotopes in Precipitation data set (GNIP), Vimeux et al. [2005] found no correlation between the isotopic composition of Amazonian rainfall and local temperature values, but instead correlations between the rainfall's isotopic composition and upstream condensation rates. Additionally, Vuille et al. [2005] found a significant negative relationship between ^{18}O abundance in precipitation and the strength of the Asian monsoon, indicating a connection between increased precipitation rates and isotopic depletion. This connection is known as the "amount effect", which is a term used to describe isotopic depletion during rainfall that is beyond that predicted by Rayleigh distillation. The amount effect is important in all areas experiencing significant monsoonal flows [*Dansgaard*, 1964; *Rozanski et al*., 1992; *Rozanski and Araguas-Araguas*, 1995; *Araguas-Araguas et al*., 1998], and has been documented using isotopic signals in precipitation, including ice and snow in both the Himalaya [*Wushiki*, 1981] and the Andes

[*Grootes et al*., 1989]. However, different mechanisms have been used to explain the amount effect and it is likely that multiple effects are responsible. For example, Dansgaard [1964] and Rozanski et al. [1993] explained that the amount effect of tropical precipitation is primarily due to the high fractional removal of heavy isotopes during intense condensation at high altitudes; they also suggested that re-evaporation of rain drops below the cloud base leads to a high relative loss of heavy isotopes in arid conditions.

Variations in the isotopic composition reflect the history of moist processes for each observed air parcel, which can be used to determine the strength of the contributing processes. Hereafter, the abundance of singly deuterated water relative to common water is expressed in terms of a "delta" value:

$$\delta D = \left[\frac{(HDO/H_2O)_{obs}}{(HDO/H_2O)_{VSMOW}} - 1 \right] \times 1000 \qquad \text{(E3.1)}$$

where HDO and H_2O are proportional to the number of molecules of each species. The ratio $(HDO/H_2O)_{VSMOW}$ is twice the Vienna Standard Mean Ocean Water standard of D/H and is 311.52×10^{-6}. With this definition, one simple description of the effects of condensation on atmospheric water vapor can be given as a Rayleigh distillation. The Rayleigh model for condensation, as introduced by Dansgaard [1964], predicts for the isotopic composition of atmospheric water vapor after condensation, and is given by

$$\frac{\delta D}{1000} = \left(\frac{\delta D_O}{1000} + 1 \right) \cdot F^{(\alpha - 1)} - 1 \qquad \text{(E3.2)}$$

where F is the fraction of initial moisture remaining in the given air mass, α is the effective fractionation factor during formation of raindrops and/or ice crystals at the cloud temperature, and δD_0 is the initial delta value of the vapor. This model describes the increased isotopic depletion as water vapor is continuously removed via condensation

While the Rayleigh model is useful in illustrating some bulk features of atmospheric isotope hydrology and indeed models the isotopic depletion of simple large-scale condensation events credibly, there are processes not included that limit its application for studies of the isotopic balance of water vapor. The effects of air mass mixing, re-evaporation of precipitation, and isotopic exchange of vapor with precipitation act to introduce isotopic variability of the residual vapor beyond that predicted by the simple Rayleigh model [*Webster and Heymsfield*, 2003; *Lawrence et al.* 2004; *Schmidt et al.*, 2005; *Worden et al.* 2007]. Moreover, regional and local effects involving evapotranspiration, turbulent transport, precipitation rates, and ice lofting are thought to further modify the isotopic composition of atmospheric water vapor, leading to distinct regional differences in isotopic composition [e.g., *Araguas-Araguas et al*., 2000; *Hoffman*, 2003; *McGuffie and Henderson-Sellers*, 2004]. For example, the continental gradient in the stable water isotope composition of rainfall is very weak for the Amazon region, and suggests strong local water recycling and the influence of transpiration [*Henderson-Sellers et al*., 2002]. These studies show that a more detailed explanation of the regional hydrology emerges by considering not only the isotopic composition itself, but the degree to which isotopic observations deviate from that predicted by simple expectations (such as that from a Rayleigh model).

The purpose of the present study is to explain the seasonal variation of the hydrologic regime over three tropical continental areas (the Amazon, north Australia, and Asian monsoon regions) in which seasonal monsoon circulations dominate. Of particular interest is providing an assessment of the contributions from advection, local and upstream convection, *in situ* condensation, recycling of vapor within regions of organized convection, and evapotranspiration. The analysis makes use of the near-global lower to middle troposphere HDO/H_2O ratio data from the Tropospheric Emission Spectrometer (TES) [*Worden et al*., 2006]. With this data, analyzing isotopic exchange during turbulent mixing and intense condensation exposes the limitations of simple explanations based on Rayleigh distillation. In order to enable interpretation of the regional hydrology from isotopes, the meteorological processes which control the isotopic composition must first be established. By examining and contrasting the hydrologic budget inferred from the isotope measurements with budgets computed from non-isotope methods, insight is gained into those hydrological processes that are common to and those that are different between the three tropical continental regions.

3.3 Annual and seasonal distribution of TES δD

The HDO/H_2O data from TES on NASA’s Aura spacecraft offers a unique global-scale view of the isotopic composition of water vapor. TES is a Fourier transform spectrometer that measures the infrared energy emitted by Earth's surface and by gases and particles in Earth's atmosphere. TES has high spectral resolutions of 0.025 cm^{-1} in limb mode and 0.1 cm^{-1} in nadir mode, which gives it the ability to resolve the shape of individual emission lines. Data used for this study comes from TES’s nadir mode, which observes a horizontal area of approximately 5.3 km x 8.3 km. Accurate estimation of the isotope ratio results from a joint retrieval algorithm that allows partial cancellation of systematic errors common to both HDO and H_2O [*Worden et al*., 2006]. Additional selection of the data is required to ensure only high quality and physically meaningful retrievals are used [*Worden et al*., 2007]. TES data used in this study comes from 249 days from August 2004 to December 2006. Two seasonal data sets are created from data retrievals from December to February (DJF) and June to August (JJA) dates, respectively. The DJF data contain 78 days; 39 days from 2004-2005, 25 days from 2005-2006, and 14 days from 2006. The JJA data contain 55 days; 2 days from 2004, 17 days from 2005, and 34 days from 2006. Aura orbits sixteen times each day while recovering approximately 500-3000 high quality profiles of atmospheric δD. A reduction of 5% on the volume mixing ratio of HDO has been used in this study to calculate the final δD values in order to account for an unknown bias in the spectroscopic line strengths [*Worden et al*., 2007]. The TES retrieval has typically around 1 degree of freedom in the vertical with an error of ±10‰ on calculated δD values [*Worden et al*., 2006], and the retrieval is most sensitive to a thick layer in the lower troposphere. As such, we restrict our analysis to lower troposphere mean values.

The annual, mass-weighted average values over the layer 500-825 hPa for temperature, specific humidity, and δD from TES are shown in Figure 3.1. Figure 3.1a shows a poleward decrease in annual temperature with weak longitudinal variations along the equator, while Figure 3.1b indicates that tropical continental areas and the Pacific warm pool contain the greatest amounts of water vapor in the 500-825 hPa layer average. The highest specific humidity values also coincide with areas known to experience frequent and intense convection (e.g., the Pacific Warm Pool), which suggests that water vapor is being moved vertically into the 500-825 hPa column from below. The TES annual δD values (Figure 3.1c) show detail of the isotopic effects of convection and condensation. The general poleward decrease in annual δD values reflects continual isotopic depletion occurring as water moves poleward, cools, and condenses. In the

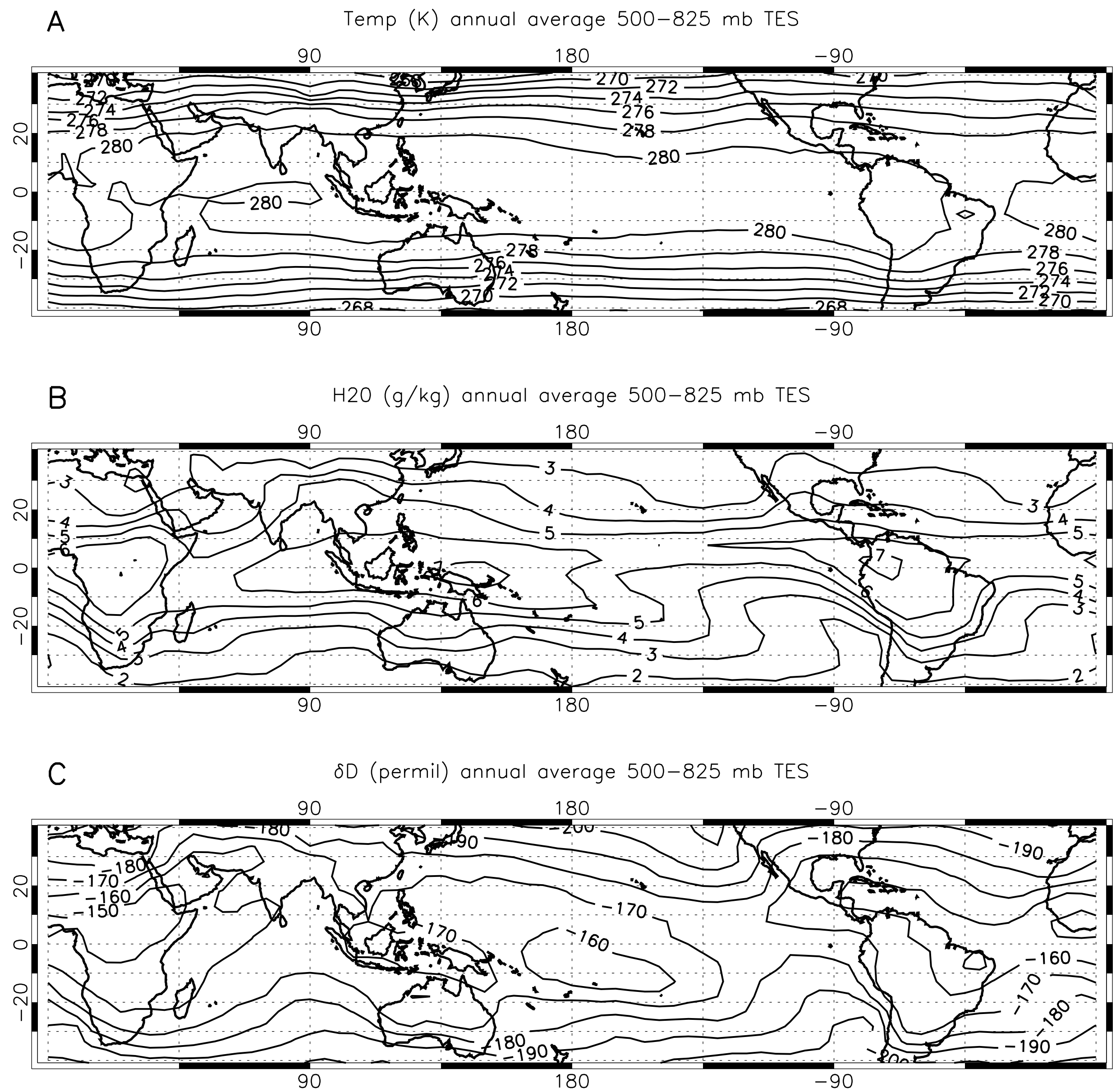

Figure 3.1: TES annual average a) temperature, b) specific humidity, and c) δD for the layer 500-825 hPa over Aug. 2004 to Dec. 2006. Contour intervals are 2 K (a), 1 g/kg (b), and 10 ‰ (c).

tropics, Worden et al. [2007] suggest that higher δD values are indicative of water vapor, which has been exposed to evaporation from the ocean and is therefore isotopically "heavy", being lofted into the 500-825 hPa layer from below. However, Figure 3.1c shows that areas known to have the strongest convection in the annual mean (i.e., the Amazon and the Pacific warm pool), do not necessarily have the highest δD values in the annual mean. This may suggest that in the areas of strongest convection, isotopic depletion by intense condensation offsets the enrichment from surface evaporation. In order to expose the underlying causes of these differences, the regional balances between advection, moist convection, condensation, and the isotopic composition of atmospheric waters must be established.

Figure 3.2 shows seasonal differences, defined as the December-February (DJF) average minus the June-August (JJA) average, in temperature, specific humidity, and δD. The DJF-JJA temperature differences (Figure 3.2a) maintain zonal symmetry outside the tropics, while asymmetry arises in the equatorial regions due to the seasonal shift in the atmospheric convergence zones and differences in the land-sea temperature contrasts. What emerges in Figure 3.2b is a strong hemispheric symmetry with more water vapor over continents during the monsoonal wet seasons with evidence of downstream advection to nearby oceanic areas. The seasonal differences in δD (Figure 3.2c) show that the Amazon and N. Australian regions, where strong monsoonal rains characterize the regional climate, have large seasonal variation in the isotopic composition. A significant seasonal difference in mean δD values is not seen over the Asian monsoon region. Further, the seasonal differences in δD over N. Australia and the Amazon basin are of opposite sign, even though these regions are at similar latitudes and both experience monsoonal type flow in the same season. Specifically, vapor over the rainforests of the Amazon is more depleted in deuterium during this region's wet season (DJF) than during the dry season

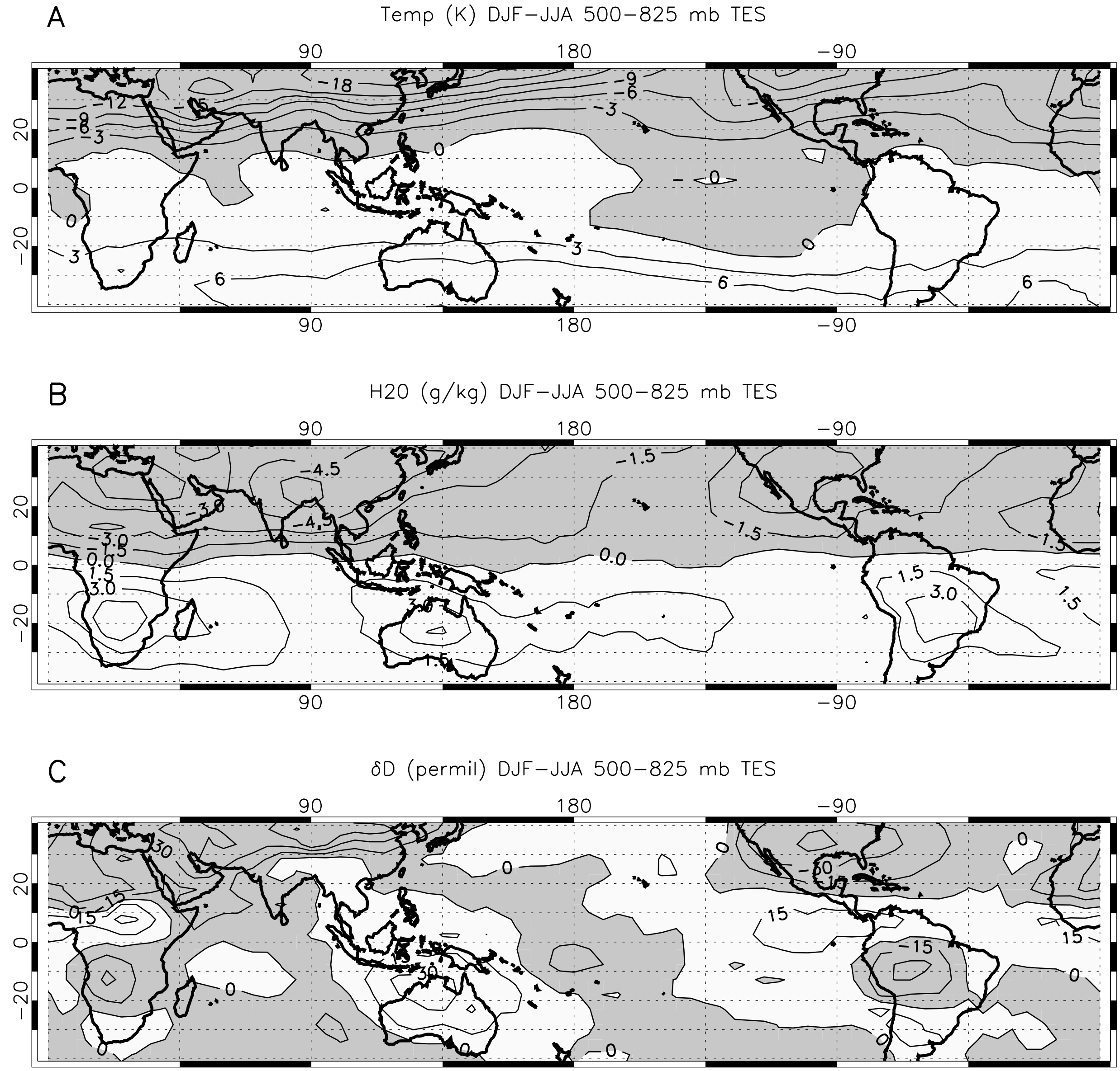

Figure 3.2: TES DJF-JJA difference in a) temperature, b) specific humidity, and c) δD for the layer 500-825 hPa over Aug. 2004 to Dec. 2006. Grey shading indicates negative values, and contour intervals are 3 K (a), 1.5 g/kg (b), and 15 ‰ (c).

(JJA), where as the opposite is true for the more arid N. Australian region. These δD anomalies over different land surfaces with well-defined monsoonal seasons immediately suggest differences in the balance of processes contributing to the hydrological balance in each region.

3.4 Local controls on isotopic composition

3.4.1 Data Selection

To establish the importance of local processes relative to large-scale influences (specifically advection), the relationship between the measured isotopic composition and meteorological parameters that capture the strength of the local processes are examined. Of interest are the associations between δD values and local temperature, specific humidity, relative humidity, precipitation rate, lapse rate, and large-scale horizontal moisture flux. These relationships indicate the importance of condensation, entrainment of recently evaporated air, and large-scale advection. Each quantity is derived from the TES observations as 500-825 hPa layer mean values, with two exceptions. First, precipitation rates are taken from the Global Precipitation Climatology Project (GPCP) daily average rainfall rates and spatially interpolated to the locations of the TES observations. Second, the scalar moisture flux values were found by integrating the product of TES specific humidity and spatially interpolated NCEP horizontal wind speeds over the five TES vertical levels between 500 and 825 hPa. The predictors described above are used for standardized linear and multiple regressions against TES δD values in Tables 3.1 and 3.2, respectively.

Region	*Season*	*Γ*	*RH*	*P*	*V·q*	*T*	*q*
Amazon	*JJA*	**-0.24**	**-0.13**	-0.02	-0.04	0.07	-0.05
	DJF	**-0.15**	**-0.39**	**-0.21**	**0.10**	0.02	**-0.34**
N. Austr.	*JJA*	**-0.28**	**0.16**	0.00	0.02	**-0.12**	**0.17**
	DJF	**-0.32**	**-0.34**	**-0.27**	**-0.26**	-0.10	**-0.35**
Asian Mon.	*JJA*	-0.06	**-0.32**	**-0.16**	**-0.16**	-0.03	**-0.28**
	DJF	**-0.21**	**0.28**	-0.08	**0.27**	**-0.35**	**0.26**

Table 3.1: Standardized, linear regressions of TES δD with lapse rate (*G*), relative humidity (*RH*), precipitation (*P*), scalar moisture flux (*V·q*), temperature (*T*), and specific humidity (*q*). Significance levels over 95%, as determined by Student's t test, are indicated in bold.

Region	*Season*	*100*R²*	*Γ*	*RH*	*P*	*V·q*	*T*
Amazon	*JJA*	**08**	**-0.26 (02)**	**-0.14 (07)**	0.06 (08)	0.01 (08)	0.07 (08)
	DJF	**30**	-0.09 (29)	**-0.62 (09)**	**-0.17 (27)**	**0.20 (26)**	**-0.28 (26)**
N. Austr.	*JJA*	**10**	**-0.24 (05)**	**0.20 (09)**	-0.01 (10)	**-0.19 (09)**	-0.06 (10)
	DJF	**26**	**-0.28 (20)**	**-0.32 (20)**	-0.11 (25)	-0.09 (25)	-0.09 (25)
Asian mon.	*JJA*	**14**	0.03 (14)	**-0.37 (04)**	-0.07 (14)	-0.03 (14)	**-0.19 (12)**
	DJF	**20**	-0.11 (19)	0.00 (20)	-0.09 (19)	**0.24 (18)**	**-0.29 (15)**

Table 3.2: Multiple correlation coefficients (squared and shown in percentage; column 3) and beta weights (defined as the standardized regression coefficients; columns 4-8) for a standardized multiple regression of δD versus five predictors for JJA and DJF. Specific humidity (*q*) has been eliminated from the regression model due to strong correlations between *q* and *RH* across all regions and seasons. Values in parentheses represent the variance in δD explained using a multiple regression model that excludes the respective predictor. Bold values indicate significance at the 95% level, based on the partial correlations of the respective variables.

For the analysis the Amazon is defined to be within the box bounded between 0°S-20°S and 290°-310°E, N. Australia as between 10°S-22.5°S and 120°-140°E, and the Asian monsoon region as between 15°N -30°N and 80°E-100°E. These definitions are mostly continental, although in the case of the N. Australian and the Asian monsoon regions, some oceanic area is included. All individual, and instantaneous, TES observations falling within these regions are used in the analysis. There are approximately equal numbers of daytime and nighttime observations for each region and season.

3.4.2 The Rayleigh Perspective in Monsoon Regions

Variations in water isotope composition are often considered to be simply associated with temperature. For vapor undergoing continual condensation, Rayleigh distillation predicts that δD values should decrease as air parcels cool due to condensation, yet no positive linear or partial correlations are found between δD and temperature for any season over the monsoon regions (Tables 3.1 and 3.2, respectively). This result largely agrees with results based on precipitation isotope data that show strong positive temperature correlations in monthly data outside the tropics and almost no correlation in warmer areas [e.g., *Dansgaard*, 1964]. Moreover, contrary to Rayleigh theory, the linear regression coefficients in Table 3.1 are significant and negative between δD and temperature during the dry seasons of the Asian monsoon (-0.35) and N. Australian (-0.12) regions (explored in detail in Sections 3.4.3 and 3.4.4 below). In order to better explain these variations in the isotopic composition of monsoon vapor, additional models must be added to Rayleigh distillation.

Figure 3.3 shows δD values within each region presented as a function of specific humidity for their respective wet and dry seasons. The wet season for the Amazon and N. Australian regions is shown for the DJF time period and for the Asian monsoon region in the JJA time period. Rayleigh distillation lines originating from air parcels with saturation specific humidity values based on oceanic temperatures of 285 K and 300 K, and initial δD values of -79‰ (approximately that of vapor in equilibrium with the ocean), are shown as black lines. Grey lines representing the enriching effects that mixing relatively moist marine and transpired air with drier air parcels are also shown, and are based on a typical tropical surface temperature of 292 K. A model for this enriching effect is described in the supplemental material of Worden et al. [2007].

Most data are more depleted than both evaporation lines, suggesting that most observations have a history of condensation. The regional dry season data (Figures 3.3a, 3.3c, and 3.3f) are reasonably constrained by the Rayleigh distillation and marine evaporation lines, while the wet season data (Figures 3.3b, 3.3d, and 3.3e) show many δD values that are more depleted than predicted by Rayleigh distillation. These wet season values may be explained by substantial isotopic exchange occurring during heavy rainfall [e.g., *Rozanski et al*., 1993] or by evaporation of falling raindrops [e.g., *Worden et al*., 2007]. However, the large variance in δD values for all regions suggests mixing processes, including turbulent transport and large-scale advection, plays a crucial role in the local isotopic variance. Additionally, the Amazon (Figures 3.3a and 3.3b) and N. Australia observations (Figure 3.3d), where the δD values exceed the δD values of evaporated oceanic water, are likely signals of transpired water since they can be explained by a source with an isotopic composition similar to precipitation in the respective regions.

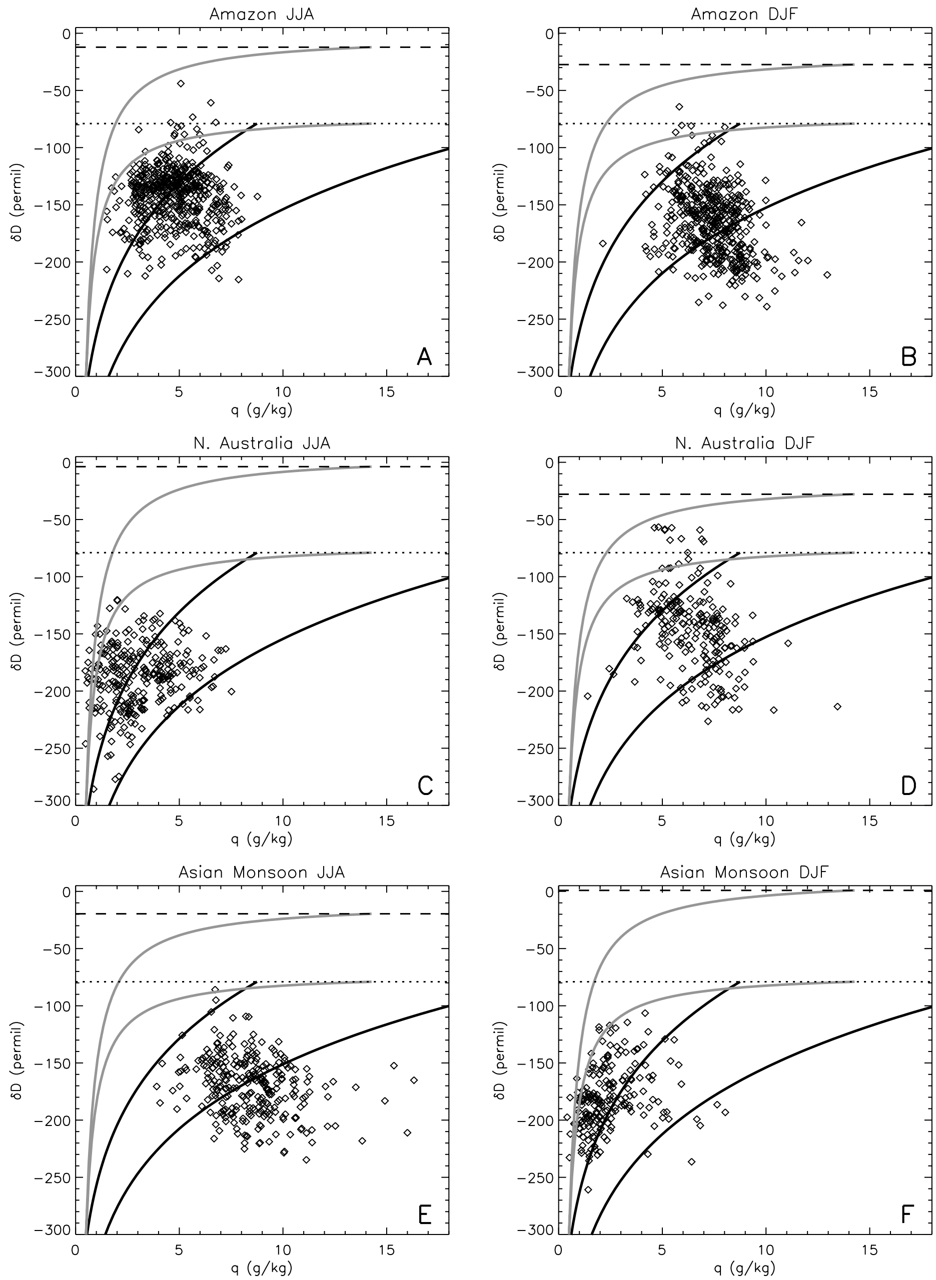

Figure 3.3: Regional δD as a function of specific humidity (q) for a) Amazon JJA, b) Amazon DJF, c) N. Australia JJA, d) N. Australia DJF, e) Asian monsoon JJA, and f) Asian monsoon DJF. Rayleigh distillation lines (black) initialized at common ocean/atmospheric surface layer δD values of -79‰ (black dotted line) with saturation specific humidity values based on surface temperatures of 285 K (left black line) and 300 K (right black line). An evaporation line (lower grey line) is also shown for reference, initialized from an a value for vapor in equilibrium with ocean water (δD value of -79‰) and saturation specific humidity values based on surface temperature of 292.5 K. Average seasonal δD values in precipitation for each region (based on GNIP observations), are also shown (black dash), with mixing lines (upper grey lines) for saturation specific humidity values based on surface temperatures of 292.5 K to indicate the upper bound imposed by transpiration.

3.4.3 Regional effects of condensation and convection on δD

Observations with higher relative humidity are more likely to have experienced recent condensation [*Cau et al.*, 2007], while observations with more negative lapse rates (less stable) indicates that the atmosphere is more likely to have undergone vertical mixing. In the latter case, evaporated moisture near the surface will have been lofted into the lower troposphere. Significant and negative linear regression coefficients for δD regressed against relative humidity are seen during the wet season of each region (Table 3.1), and are very similar in magnitude between regions. These coefficients suggest that local condensation is a significant driver of isotopic depletion, yet a second mechanism can also explain this result. Specifically, low humidity conditions are more likely to drive strong evaporation of less depleted water from the surface, which would allow for increased vertical transport of less depleted moisture into the 500-825 hPa layer. The squares of multiple correlation values indicate that 30%, 14%, and 26% of the variance in wet season δD values is explained by the five predictors for the Amazon, Asian monsoon, and N. Australian regions, respectively (Table 3.2). The explained variance in wet season δD values drops substantially to 9% for the Amazon and 4% for the Asian monsoon region when relative humidity is removed as a predictor in the multiple regression models. The partial correlations between δD and lapse rate are insignificant during these two regions' wet seasons, and further suggest that isotopic depletion by large-scale condensation is the dominant effect on isotopic variability (Table 3.2). Conversely, the explained variance in δD values over the Australian region is reduced to 20% when either the relative humidity or lapse rate predictors (both have negative regression coefficients) are removed from the five-variable, multiple regression model. This result supports a mechanism whereby surface evaporation and the vertical transport of less depleted boundary layer vapor influence the isotopic composition within the 500-825 hPa layer during dry conditions. Therefore, the multiple regression models suggest that condensation is the dominant control on isotopic variability during the wet seasons of the Amazon and Asian monsoon regions, but that convection and condensation are equally dominant during N. Australia's wet season. These differences in regional hydrology are partially responsible for the DJF-JJA δD value difference between regions (Figure 3.2c).

During the dry season, the Amazon shows a significant negative linear relationship between δD and RH (-0.13; Table 3.1), whereas the Australian and Asian Monsoon regions show significant positive relationships (0.16 and 0.28, respectively). The Amazon dry season humidity at the 500-825 hPa level remains high (50-90% higher than the other regions), and the negative relationships between δD with RH and lapse rate may be explained by the mechanisms given for the N. Australian wet season (above). For the drier Australian and Asian Monsoon atmospheres, however, the entrainment of humid and isotopically heavy boundary layer air appears to increase both the δD values and the relative humidity in the 500-825 hPa layer, resulting in the positive linear regression coefficients witnessed in Table 3.1. Additionally, Table 3.1 indicates that the lowest dry season δD values occur during warm, dry, and stable conditions for these two regions, which suggests that subsidence plays a major role in supplying dry air to these regions and controls the most depleted isotopic values. However, the influences of advection affect the interpretation of the Asian monsoon and N. Australian dry season hydrologic systems. This aspect will be thoroughly addressed in Section 3.4.4 and Section 3.5.

Precipitation rates have been found to influence isotopic composition during the monsoonal seasons, and are suggested as one cause of the amount effect [e.g., *Matsuyama et al.*, 2005; *Vuille et al.*, 2005]. Table 3.1 shows significant negative relationships between wet season δD values and GPCP daily rainfall rates for all regions. At first glance, the fact that the strongest standardized linear correlation between δD and precipitation occurs over the drier N. Australian region suggests that the kinetic isotopic effects of rainfall evaporation may be an important part of the amount effect. However, the partial correlations of δD versus precipitation are only significant for the Amazon wet season, where the explained variance in δD drops slightly to 27% when precipitation is removed as a predictor (Table 3.2). The lowest δD values for the wet seasons of all regions (Figures 3.3b, 3.3d, and 3.3e) fall well below Rayleigh distillation predictions, yet the regression results indicate that with the exception of the Amazon region, the amount effect is acting upstream of the areas of interest during the monsoon seasons. The upstream aspect of the monsoonal hydrology will be addressed in Section 3.5.

3.4.4 Regional effects of advection on δD

When the atmosphere is unstable, turbulent mixing and convective transport can occur. If the local advection is strong, however, it will reduce the local signal of convective transport. Scalar moisture flux is used here as a measure of the rate at which the isotopic composition is changed by horizontal advection, and is similar to the advective rate parameter in the work of Noone [2008]. Scalar moisture flux can be considered related to the rate at which local isotopic values approach that of the upstream source. It is useful to note that advection can either enrich or deplete the regional isotopic composition due to the difference between the isotopic composition of the source and the local values. As such, advection differs from both condensation (which always depletes) and the influence of evaporated air from a local source (which usually enriches). Specifically, horizontal advection of depleted air parcels is linked to upwind condensation and hence fractionation, while advection of enriched vapor results if there has been little condensation *en route* from the evaporative source.

Significant linear correlations between δD and scalar moisture flux values are seen for the N. Australian and Asian monsoon wet seasons (-0.26 and -0.16, respectively; Table 3.1). However, the partial correlations between δD and scalar moisture flux values are statistically insignificant for these regions (Table 3.2) as a result of significant positive correlations between moisture flux and relative humidity (0.39 for N. Australia and 0.28 for the Asian monsoon region). These relationships suggest that moisture advection acts to influence δD variability through its influence on humidity during the wet seasons of N. Australian and Asian monsoon regions. Conversely, the significant and positive linear and partial correlations between δD and scalar moisture flux (Tables 3.1 and 3.2, respectively) indicate that strong moisture advection directly influences isotopic variability over the Amazon. However, these relationships also suggest that the lowest δD values, which are depleted beyond Rayleigh predictions, are observed primarily during relatively calm conditions. This association lends support to the argument that rainfall recycling that occurs locally over the Amazon basin acts to produce the anomalously low δD values during the wet season.

The Asian Monsoon dry season shows a positive linear correlation between δD and scalar moisture flux (0.27; Table 3.1), indicating that the horizontal advective source is less depleted than the ambient air. The multiple regression analysis for this region shows that the lowest δD values occur during quiescent and warm synoptic conditions, which suggests that subsidence introduces the lowest δD values. The multiple regression model for the N. Australian dry season suggests that the lowest δD values are largely associated with dry, stable, and windy conditions. It is clear that the stability of the overlying atmosphere dominates the isotopic variability of the

500-825 hPa layer during the N. Australian dry season, since lapse rate associations control approximately half of the explained variance in δD values in the multiple regression model (Table 3.2). However, it remains unclear if the most depleted air parcels arrive from subsidence, or via horizontal advection in this region. This uncertainty is addressed in more detail in Section 3.5 using back trajectory analysis.

3.5 Hydrologic Balance of Tropical Continents

3.5.1 Differences in Seasonal Hydrology Across Regions

Having established how various meteorological processes influence the isotopic composition of tropical continental areas, the task of assessing the regional hydrology of the three study regions with the TES HDO measurements is now tenable. Although the regression and correlation analyses described earlier are useful for gaining initial insight to the local controls on isotopic ratios, only a small percentage of the total variance in each region is captured by the local correlations alone (8-30%; Table 3.2, third column). This result makes clear that the variance in isotopic composition of the remote water sources (both upstream and near-surface) associated with the long-range advection and the entrainment of lower level vapor is important, and must be accounted for to fully explain the observed variance in the regional observations.

A large component of seasonal hydrologic change is associated with changes in advective pathways. To quantify this, back trajectories originating from each TES observation location were calculated using three-dimensional wind fields from NCAR/NCEP Reanalysis data [*Kalnay* *et al*, 1996], and assuming an arrival height of 670 hPa (in the middle of the 500-825 hPa layer). Vertical (“sigma”) velocity is estimated from the horizontal wind fields and surface pressure tendency through integration of the continuity equation to each of the 28 sigma levels in the Reanalysis data. The trajectory model uses tri-cubic interpolation in space and linear interpolation in time to find the wind at the trajectory locations [*Noone and Simmonds*, 1999]. Integration of the trajectory equation uses a fourth order Runge-Kutta scheme and a time step of 20 minutes. The probability distributions of trajectory origins five-days prior to the observations are shown in Figures 3.4-3.6 as the grey shaded region where the likelihood exceeds 5 %/10^6km. Following the work of Noone et al., [1999], the probability distribution is computed by convolving the trajectory points with a Cressman-type weighting function with a mean radius of influence 500 km. The global integral of the probability density field is 100%, and the total seasonal percentage of parcel origins inside each the grey shaded regions in Figures 3.4-3.6 is approximately the number of 10^o longitude by 10^o latitude grid boxes within the contour times 5%. The solid contours in Figures 3.4-3.6 are for quartile analysis, and are discussed in Section 3.5.2 (below).

The origin probability distribution for the Amazon shows that the wet season (DJF; grey shading in Figures 3.4a-b) parcels tend to originate from further north than those of the dry season (JJA; Figures 3.4c-d). The wet season five-day trajectories for the Asian monsoon (JJA; Figures 3.6c-d) and N. Australian (DJF; Figures 3.5a-b) regions are generally less variable in origin locations and shorter in length than those during their dry seasons (Figures 3.6a-b and 3.5c-d, respectively), and are consistent with relatively steady monsoonal flow. Beyond this kinematic result, the δD frequency distributions for the DJF and JJA five-day origin regions, as well as the frequency distributions at the observation sites, are shown in Figure 3.7. The

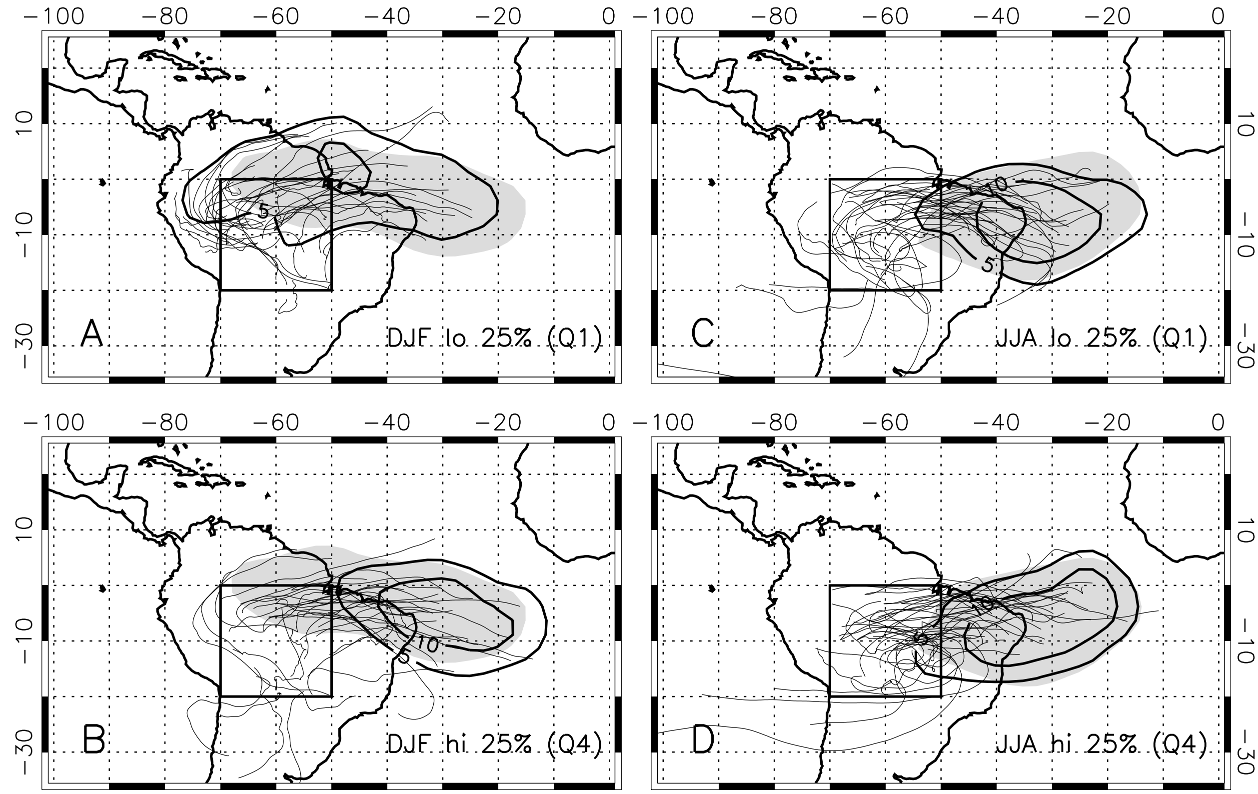

Figure 3.4: Probability distributions of five-day trajectory origins for DJF (a, b) and JJA (c, d) for Q1 (a,c) and Q4 (b,d) δD from the Amazon region. Grey shading indicates 5 %/10^6 km^2 of five-day origins of DJF (JJA) δD values. Black contours indicate 5%/10^6 km^2 and 10%/10^6 km^2 of five-day origins of Q1 (Q4) δD values. Each 10 by 10 degree box represents approximately 10^6 km^2. One in three Q1 (Q4) individual trajectory paths are shown in each case.

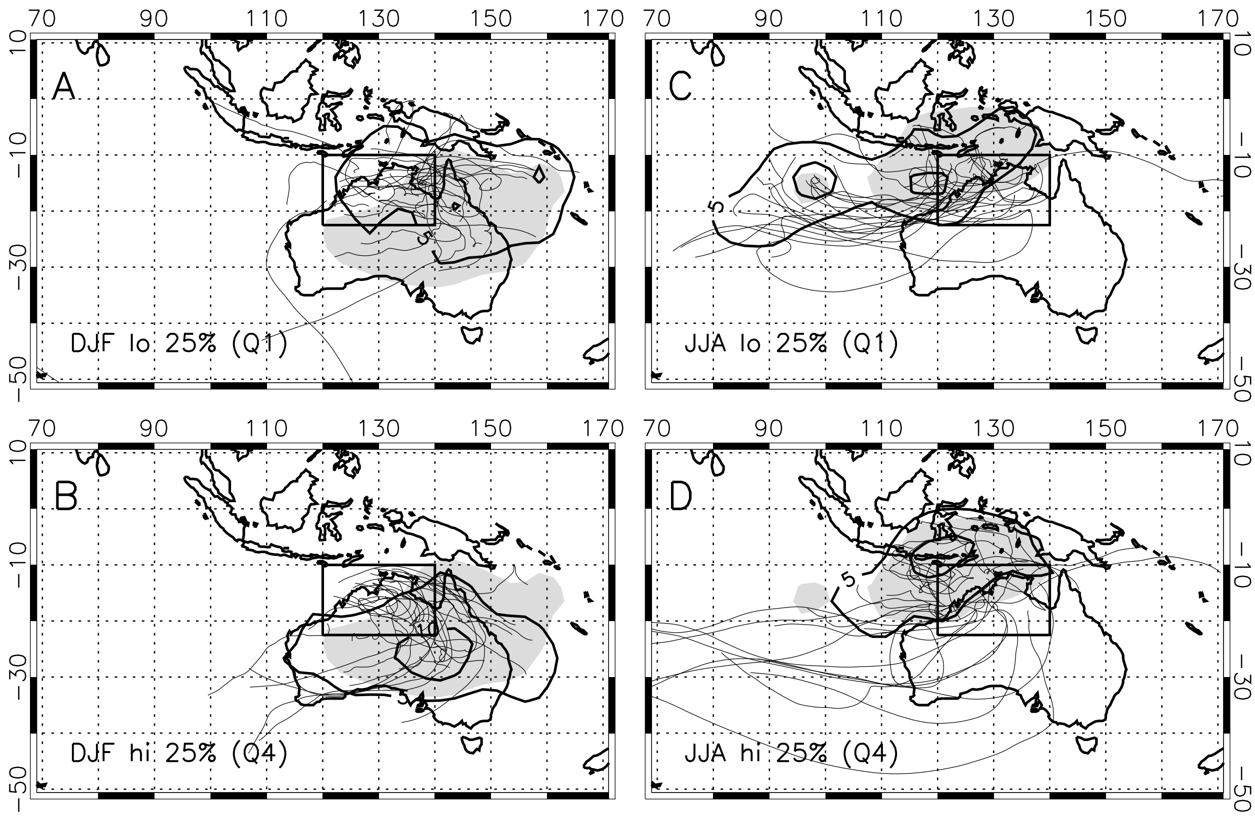

Figure 3.5: as in Figure 3.4 except for N. Australian region; trajectory plots from respective quartiles are overlaid from every second TES observation.

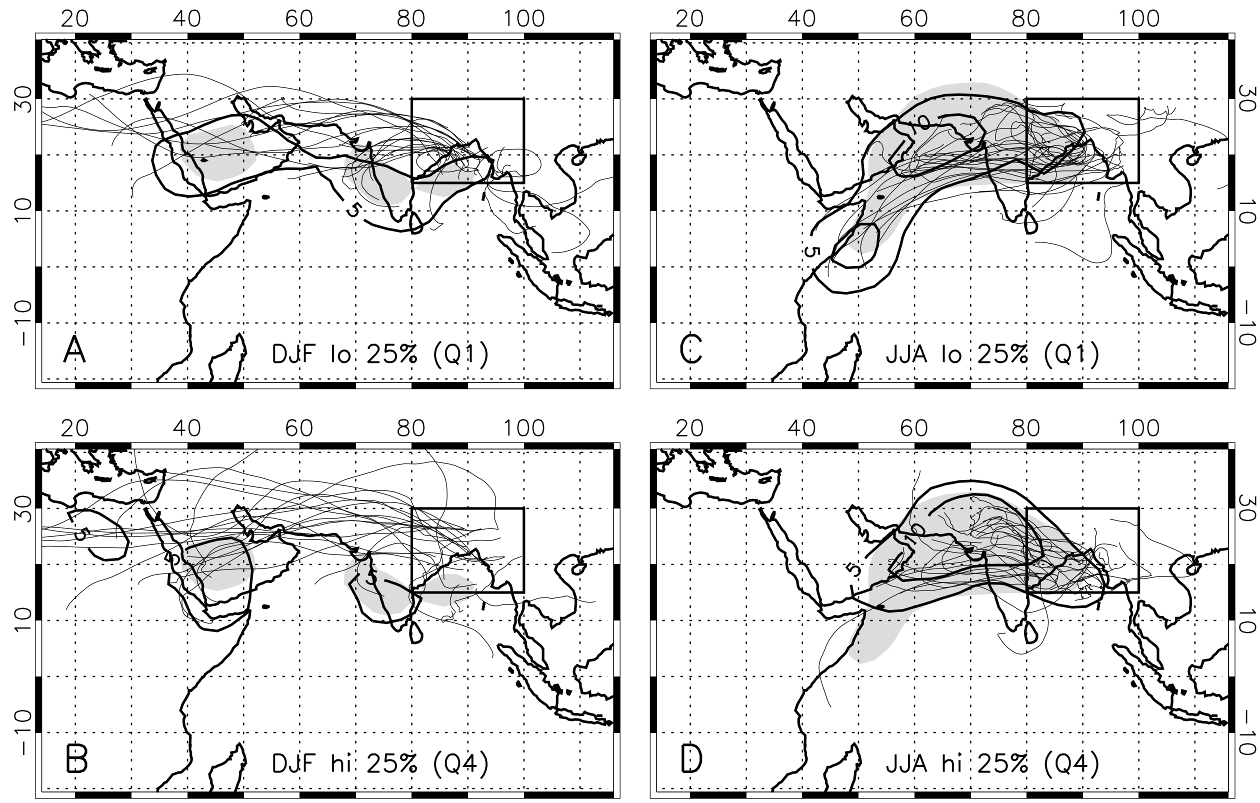

Figure 3.6: as in Figure 3.4 except for Asian monsoon region; trajectory plots from respective quartiles are overlaid from every second TES observation.

frequency distributions of the origin regions are constructed for each season by taking all TES δD values within a 50 km radius of the positions of the five-day back trajectories. The values are adjusted for altitude based on the vertical change in δD found in individual TES δD profiles between 500 hPa and 825 hPa (typically 30‰/km, but different from profile to profile), and the change in height deduced from the trajectory calculation. This origin frequency distribution captures the variation in the seasonal mean distribution of values upstream of the respective regions. This is appropriate for the analysis as it is found in detailed examination of individual five day trajectories that the observed isotope signal is mostly set by moist processes that are associated with the monsoonal areas. This time frame also allows for an accurate diagnosis of large-scale subsidence. Thus, the difference in the distribution from the upstream origin to final observation provides the signature of exchange processes (or lack thereof), which can be understood in detail by considering the conditions experienced by the air parcels during transport.

Along the trajectory path, specific humidity, temperature and geopotential height are found via interpolation from the Reanalysis grid to the three-dimensional trajectory point. For all regions, the wet season air parcels come from much lower in the atmospheric column than those of the dry season, and are generally associated with condensation during ascent (see Section 3.5.2, below). This is evident in the frequency distributions of the origin and observation site δD values for DJF and JJA (Figure 3.7), which show that the five-day origin mass weighted average δD values are less depleted during the wet season than those of the dry season. Very strong isotopic depletion *en route* during the wet season in the Amazon and Asian monsoon regions (a mean isotopic change of -40‰ and -44‰, respectively; Figures 3.7a and 3.7f) exceeds that from Rayleigh distillation expectations (-32‰ and -28‰, respectively), and can be explained by

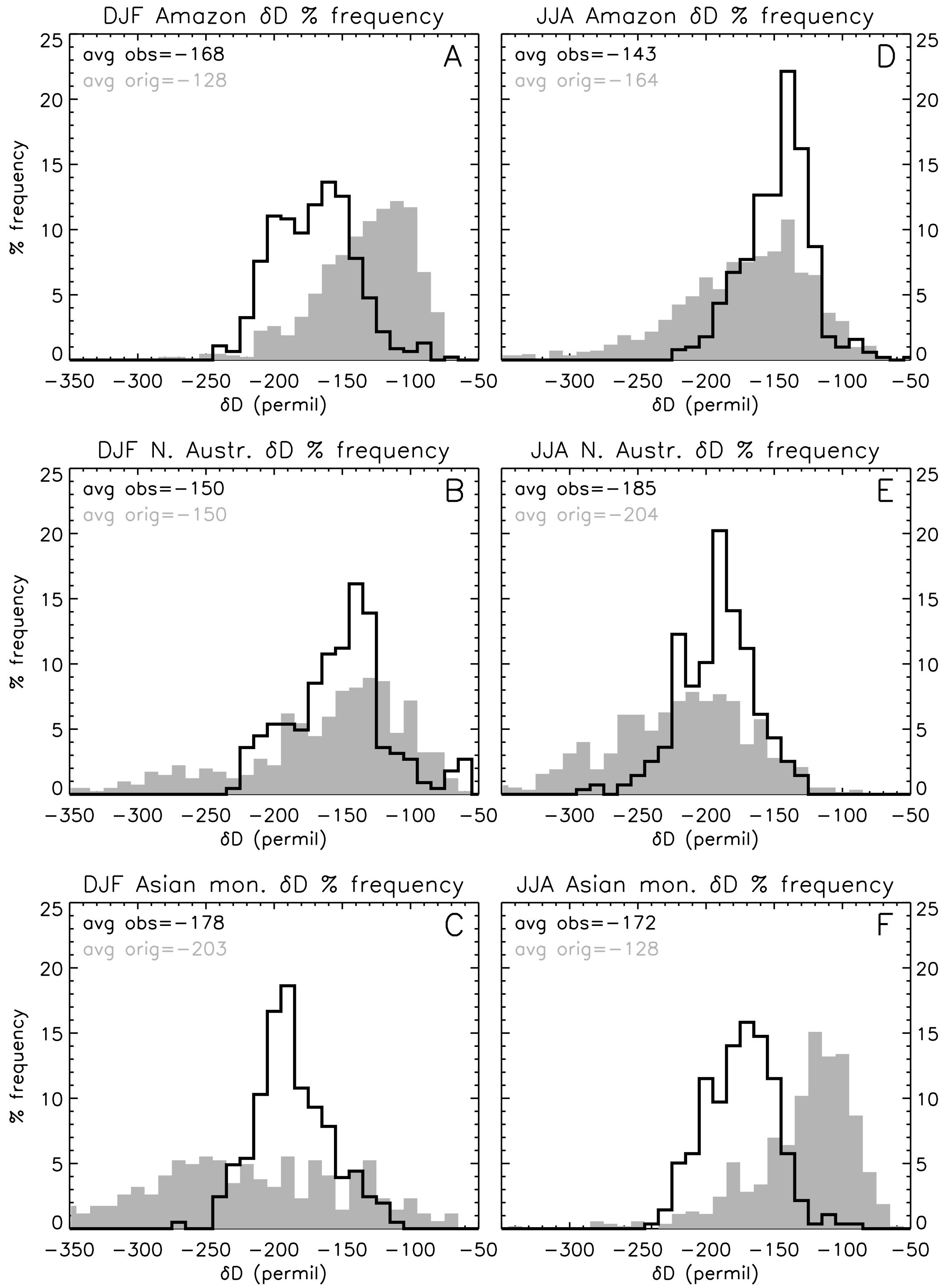

Figure 3.7: Frequency distribution of δD values over the layer 500-825 hPa for DJF (a,b,c) and JJA (d,e,f) seasons for the Amazon (a,d), N. Australian (b,e), and Asian Monsoon (c,f) regions. Grey shading represents δD value distribution within the region close to the five-day back trajectory origins, while black line represents the distribution within the regions.

isotopic exchange during rainfall evaporation [e.g., *Worden et al.*, 2007]. The N. Australian wet season exhibits no change in mean isotopic composition *en route*, although the shape of the frequency distribution changes substantially (DJF; Figure 3.7b). Further, it is evident that condensation is occurring in this region since many δD values are lower than Rayleigh distillation predictions (Figure 3.3d). Thus, rather than indicating that there is no hydrologic exchange along the trajectory paths, this apparent isotopic balance shows mixing with less depleted water from the near-surface, which counteracts the isotopic depletion that results from condensation.

3.5.2 Processes Contributing to Intra-Seasonal Variability

3.5.2.1 Quartile Analysis Configuration

To illustrate the range of atmospheric processes contributing to the distribution of TES δD values, the δD observations in each region are partitioned into the most depleted (Q1) and least depleted (Q4) quartiles. In Figures 3.4, 3.5 and 3.6, a subset of the five-day trajectories within each quartile is shown in each panel (every third trajectory for the Amazon region, and every second trajectory for the N. Australian and Asian monsoon regions). The moisture weighted mean and standard deviation of δD for the lowest (Q1) and highest (Q4) quartiles within both the five-day origin and the final TES observation locations are given for each region in Table 3.3.

To aid in assessing the roles of subsidence and condensation, dry and moist static energy are computed and are useful diagnostics because they are conserved during adiabatic and

			Mean δD		*Stddev δD*		*Δ(δD)*
Region	*Season*	*Quart.*	*origin*	*obs*	*origin*	*obs*	*obs-origin*
Amazon	DJF	Q1	-127	-203	38	11	-76
		Q4	-130	-129	56	17	+1
	JJA	Q1	-153	-175	60	14	-22
		Q4	-176	-113	61	15	+63
N. Austr.	DJF	Q1	-151	-193	69	15	-42
		Q4	-161	-104	82	23	+57
	JJA	Q1	-207	-221	55	17	-14
		Q4	-203	-154	70	13	+51
Asian mon.	DJF	Q1	-203	-214	66	13	-11
		Q4	-198	-143	99	15	+55
	JJA	Q1	-121	-204	32	11	-88
		Q4	-141	-139	40	14	+2

Table 3.3: Mean δD and standard deviations for the upper (Q4) and lower (Q1) quartile parcel five-day origin and observation site locations. The change in δD from origin to site, Δ(δD), is listed in the final column.

pseudoadiabatic processes, respectively [*Back et al.*, 2006]. These quantities have been normalized by the specific heat of dry air at constant pressure (c_p), such that they have units comparable to potential temperature and equivalent potential temperature. Thus, the normalized variables, dry static temperature (DST) and moist static temperature (MST), are defined as

$$DST = T + \frac{g}{c_p} z \qquad \text{(E3.3)}$$

$$MST = DST + \frac{L}{c_p} q \qquad \text{(E3.4)}$$

where T is temperature, g is gravitational acceleration, z is geopotential height, q is specific humidity, and L is the latent heat of vaporization of water. The temperature, dry static temperature, specific humidity, moist static temperature, and geopotential height values within the parcels over the five day approach to the regions are shown in Figures 3.8, 3.9, and 3.10. Note that the vertical axes of each panel in Figures 3.8, 3.9 and 3.10 are scaled to have comparable units of energy such that a vertical displacement in one panel is the same vertical displacement on all others.

3.5.2.2 Wet season processes

During the regional wet seasons, Q1 (most depleted) air parcels originate relatively closer to the equator (Figures 3.4a, 3.5a, and 3.6c) and lower in the atmosphere (Figures 3.8c, 3.9c, and 3.10f) than the Q4 (least depleted) air parcels in all cases. Additionally, the Q1 δD values for the wet seasons show isotopic depletion from the five-day origins to observation sites (δD difference

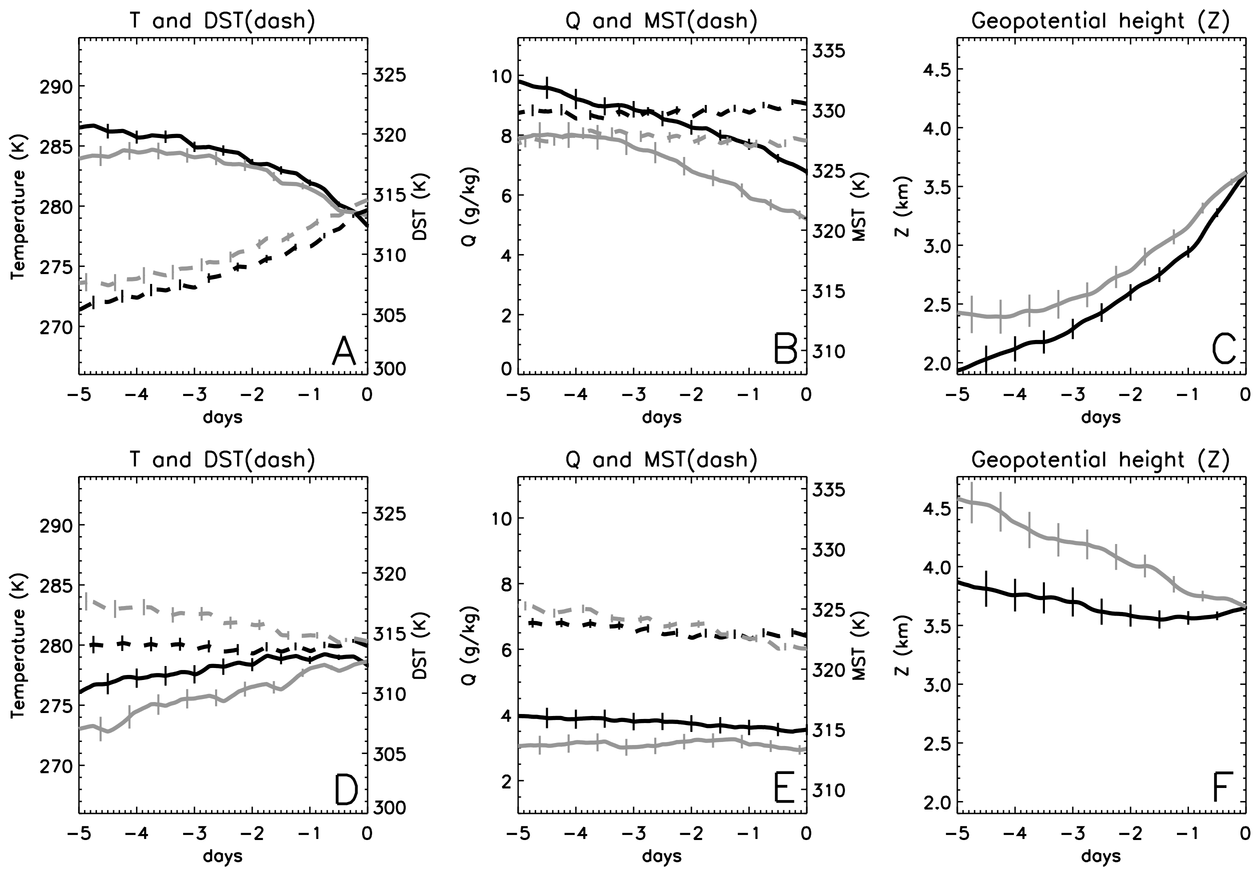

Figure 3.8: Amazon five-day histories along computed trajectories of temperature and dry static temperature (dashed) for DJF (a) and JJA (d), specific humidity and moist static temperature (dashed) for DJF (b) and JJA (e), and geopotential height for DJF (c) and JJA (f). Black lines indicate the mean of Q1 air parcels, while grey lines indicate the mean of Q4 air parcels. In all plots and between each plot, the vertical axes are scaled such that vertical displacements in any panel are "energy conservative", and can be compared to the same vertical displacement in other panels. For example, changes of specific humidity or geopotential height scale exactly with the changes in temperature that MST or DST would experience from such change. Errors bars show the uncertainty (1σ) of the mean.

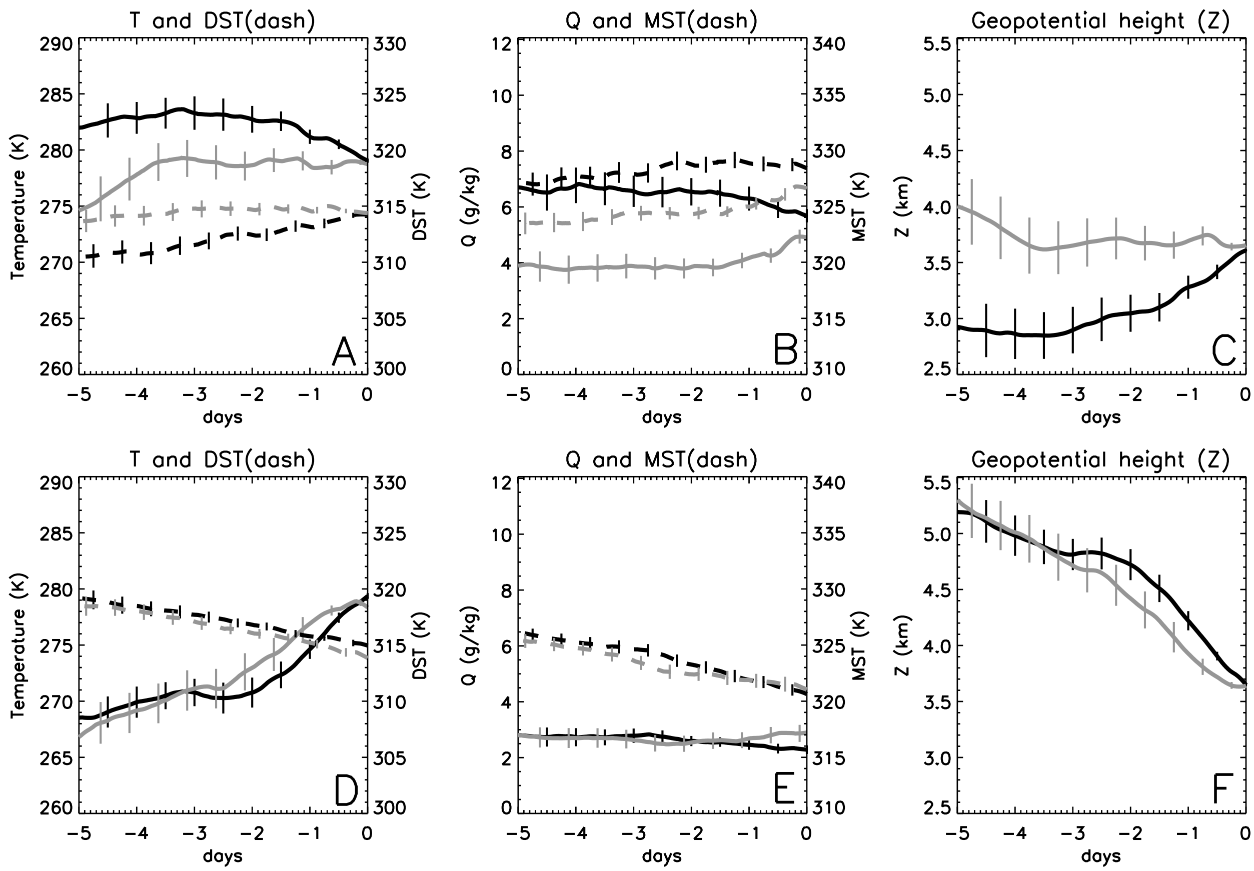

Figure 3.9: as in Figure 3.8 except for N. Australian region

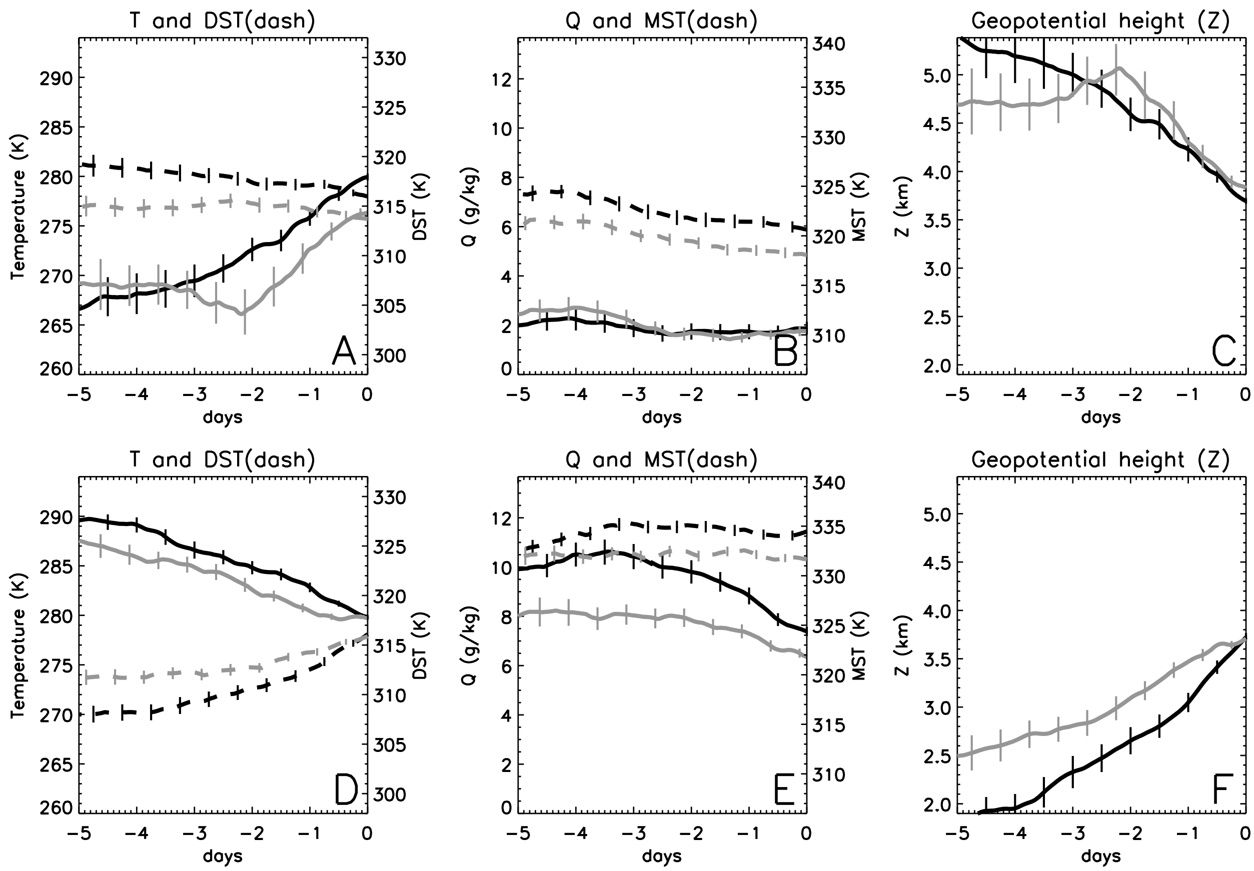

Figure 3.10: as in Figure 3.8 except for Asian monsoon region

of -76‰ for the Amazon, -42‰ for N. Australia, and -88‰ for the Asian monsoon region; Table 3.3). Conditions within the relatively moist Q1 parcels indicate condensation *en route* via decreasing specific humidity values and generally constant MST values (Figures 3.8b, 3.9b, and 3.10e). Using these specific humidity values and the upstream δD values, Rayleigh distillation (Equation 2) consistently results in an underestimation of the observed depletion (-33‰ for the Amazon, -14‰ for N. Australia, and -25‰ for the Asian monsoon region). This mismatch indicates isotopic exchange acting during strong condensation and rainfall during the monsoon season as shown by Worden et al. [2007].

The wet season Q4 air parcels for the Amazon and Asian monsoon regions increase in geopotential height (Figures 3.8c and 3.10f), decrease in specific humidity, and maintain constant MST values (Figures 3.8b and 3.10e) *en route*. This supports condensation, and hence isotopic depletion (Rayleigh distillation predicts 37‰ and 20‰ depletion for the Amazon and Asian monsoon regions, respectively), yet there is almost no change in δD values across the five day path (Table 3.3). Recall that from above, the linear regression coefficients between δD with lapse rate and relative humidity suggest that local convective processes over the Amazon strongly influence the local hydrology (Table 3.1). The present results suggest that along the moisture pathway, a balance between the enrichment caused by supply from convective detrainment and the depletion caused by condensation leads, remarkably, to a nearly constant isotope ratio. Although qualitative in nature, this result illustrates the value of isotopes in identifying multiple exchange processes that can otherwise be overlooked if only the net change in observed moisture is considered.

For the Asian monsoon region, the highest wet season δD values (i.e., Q4) primarily occur during quiescent times, as indicated by low scalar moisture flux (Table 3.1), and the associated air parcels are those which travel primarily over India (Figure 3.6d). These factors suggest a connection between the land surface and isotopic enrichment of the Q4 air parcels, since slowly moving air parcels have more opportunity to mix with air near the land surface. However, due to a lack of correlation between δD values and lapse rates, evidence for a specific mechanism for vertical transport of moisture into the 500-825 hPa layer (e.g., by convection or turbulent transport) cannot be identified. Similar to the Asian monsoon region, the N. Australian wet season Q4 air parcels generally originate closer to the Australian continent and travel more slowly than the Q1 air parcels (Figure 3.5), allowing surface exchange to influence the parcel's isotopic composition (i.e. through convective detrainment). The wet season Q4 air parcel histories for N. Australia do not indicate large-scale condensation, as shown by the increasing specific humidity and MST values over time (Figure 3.9b), and the lack of ascent to the observation locations (Figure 3.9c). These values show a 57‰ enrichment over the five-day period (Table 3.3), which is likely due to convective detrainment of relatively enriched and moist air plumes originating from the boundary layer, as shown by both the correlation between δD and lapse rate (Table 3.1) and by the increase in specific humidity along a constant trajectory height as the parcels approach the TES observation locations (Figure 3.9b).

For all regions, the wet season Q4 δD values indicate moisture derived from the surface plays an important role for the regional hydrology. On the other hand, through enhanced isotopic depletion (i.e., greater than Rayleigh), the Q1 δD values indicate that rainfall re-evaporation also plays a role. Similar processes (i.e., enhanced isotopic depletion through heavy rainfall and isotopic enrichment due to convective detrainment and turbulent transport) add to intra-seasonal isotopic variability in all three regions. However, the effects of isotopic enrichment via convective detrainment are much greater during the wet season of N. Australian than in those of the Amazon and Asian monsoon regions.

3.5.2.3 Dry season processes

For the Amazon and N. Australian regions, the histories of the dry season Q4 air parcels show steady specific humidity values (Figures 3.8e and 3.9e) and decreasing geopotential heights (Figures 3.8f and 3.9f). Additionally, the decreasing DST (Figures 3.8d and 3.9d) are consistent with radiative cooling (cooling of ≈ 1 K/day), and further indicate large-scale subsidence. For the Asian monsoon region, the Q4 trajectories show flow around the Himalayan Plateau two days prior to arrival (Figure 3.6b), followed by subsidence to the observation locations (as seen in Figures 3.10a-c as decreasing DST values, steady specific humidity values, and decreasing altitude).

The dry season Q4 air parcels arrive at the observation sites having become enriched relative to the mass weighted mean values of the source regions (63‰ enrichment for the Amazon, 51‰ for N. Australia, and 55‰ for the Asian monsoon; Table 3.3). This observed isotopic enrichment of the Q4 air parcels is unexpected for large-scale subsidence, yet can be explained by a contribution from even modest, upwards vertical transport of moist, less depleted air into the 500-825 hPa layer (consider the mostly vertical shape of the hyperbolic mixing lines at low specific humidity in Figure 3.3). This argument is supported by the significant and negative coefficients found in the linear regressions of δD and lapse rate (Table 3.1), which suggest an influence from convection or turbulent mixing. Put in this context, the positive correlations between δD and RH for the N. Australian and Asian monsoon regions suggest that the mixing in of low level moisture (through convective detrainment or turbulent transport) is a dominant process in controlling the (low) humidity in the regions. Conversely, because the Amazon dry season atmosphere is often closer to saturation than the other regions, the negative correlation between δD and RH (Table 3.1) suggests either that evapotranspiration is constrained by the humidity of the overlying atmosphere or that frequent condensation is a more dominant depleting effect for the local δD values.

The dry season Q1 air parcels subside towards the TES observation sites over the N. Australian and Asian monsoon regions, while the DST values decrease at a rate consistent with radiative cooling (around 1K/day; Figures 3.9d and 3.10a). The respective Q1 isotopic values change very little under these conditions (Table 3.3), and suggest that the lowest seasonal δD values act as a tracer of subsidence for these two regions. The linear correlations in Table 3.1 support this argument, where the lowest dry season δD values over N. Australia and the Asian monsoon regions occur during warm, dry, and stable periods. For the Asian monsoon region, evidence for subsidence is provided by the positive correlation between δD and scalar moisture flux, which indicates that low δD values are associated with quiescent conditions. For N. Australia, the trajectory lengths are generally shorter for the Q1 δD values than those of the Q4 values (compare Figures 3.5c and 3.5d), suggesting a similar relationship. Conversely, the Amazon dry season Q1 δD values show a depletion of 22‰ *en route*, while the associated air parcel histories support condensation via the steady MST values and slightly decreasing specific humidity values. Hence, variations in the degree of condensation during transport from the upstream origin, and variations in the limitation on local evapotranspiration due to high local humidity, are the primary drivers of intra-seasonal dry season δD variability in this region.

The dry season δD quartile analysis reveals that dry, subsiding air over the N. Australian and Asian monsoon regions is a major part of the regional hydrology, but that occasional mixing with surface-derived moisture acts to partially control humidity in those regions. In contrast, while the Amazon region also experiences large-scale subsidence, powerful low-level convection acts to enrich all subsiding air parcels quickly. Additionally, the Amazon experiences condensation during the dry season, which is far stronger than during the dry season for the other two regions. Thus, the dry season Amazon hydrology is an involved mix of evaporative exchange and condensation, which is unique compared to the dry seasons of the N. Australian and Asian monsoon regions. This complexity is not easily understood without isotopic constraints.

3.6 Conclusions

Isotopic measurements from TES were used to examine the differences in the hydrology of three tropical continental areas. The TES data set used here spans three years and thus provides initial insight to the regional climatology. Some aspects of the balance of hydrologic processes can be resolved using TES isotopic data, providing new opportunities for understanding the movement of water in the climate system. To do so with confidence, the factors controlling the isotopic signals over three geographically different, yet convectively active, continental regions were established. Important regional differences in hydrology emerged by comparison of the dominant seasonal and intra-seasonal controls on mean δD values.

Results show that differences in the seasonal controls (condensation, convection, and subsidence) on the δD values lead to the regional differences in DJF-JJA δD values (recall

Figure 3.2c). The isotopic depletion caused by intense condensation in the Asian monsoon wet season is strong enough to produce δD values approximately equal to those of the subsidence-controlled dry season. For the Amazon, intense condensation produces much lower δD values than does intermittent condensation and convection during the dry season. During the wet season, variations in the strength of monsoonal condensation and boundary layer ventilation events introduce intraseasonal variability in N. Australian δD values, however the interseasonal (i.e., DJF-JJA) δD difference appears to be dominated by the intrusion of isotopically depleted vapor during dry season subsidence.

The lowest δD values observed during all regional wet seasons show isotopic depletion beyond that predicted by Rayleigh distillation. This indicates an "amount effect" on vapor phase stable water isotopes, and that in-cloud isotopic exchange and rainfall evaporation are an important part of the regional hydrologic budget. The study by Vimeux et al. [2005] found no relationship between isotopic values in precipitation with local temperature or local rainfall rates near Bolivia. While the present study also finds no significant correlations between δD values and temperature during the regional monsoons, it does show that rainfall rates affect the δD values of tropospheric water vapor over the Amazon. Thus, this study incorporates and extends the findings of Rozanski et al. [1993] and Worden et al. [2007], by showing that the amount effect primarily occurs upstream of monsoonal regions, but that it also occurs within the regional boundaries of the Amazon.

Results confirm that while Rayleigh distillation is useful in explaining some features in the regional δD values, additional isotopic exchange during heavy monsoonal rainfall and turbulent transport of boundary layer moisture makes the δD distributions over monsoonal areas highly non-Rayleigh in nature. Relatively high δD values during times of weaker stability, as measured by the lapse rate, show that local convection is important for the near surface hydrology of monsoonal regions. The balance between convective moisture transport and the condensation in the region of convection is important for the local surface latent heat budget. Similar results that indicate the importance of convective moisture transport were found in the region of convective clouds in models by Schmidt et al. [2005] and from aircraft observations by Webster and Heymsfield [2003]. In the present study, the local convective effect is most pronounced over both the dry and wet season of N. Australia, as well as during the dry season of the Amazon. Anomalously high dry season δD values over the Amazon indicate that convection transports boundary layer moisture into the overlying atmosphere [e.g., *Worden et al*., 2007], which is likely partially composed of transpired water. This result is in general agreement with the work of Henderson-Sellers et al. [2002].

Future work to estimate the degree of rainfall evaporation and supply of boundary layer air in these regions must incorporate knowledge of the boundary layer δD values. Since the TES instrument is primarily sensitive to H_2O and HDO above the height of the boundary layer (maximum sensitivity is 500-825 hPa), the boundary layer values must be inferred from modeling or from surface measurements of vapor or precipitation. To this end, direct measurement of the isotopic composition of low-level vapor would aid in resolving the amount of continental water recycling which occurs over each region. However, by combining information about standing water, soil and vegetation properties with observed δD values of precipitation, the isotopic composition of moisture from surface fluxes can be inferred, and used to constrain an adequate hydrologic exchange model. The success of the present study, which focuses on process analysis, gives confidence that more sophisticated modeling and assimilation approaches can be used in conjunction with the TES HDO data to assess the global and regional scale hydrology.

4 Chapter 4

Characteristics of Atmospheric Moistening and Dehydration Derived Using Lagrangian Mass Balance From Tropospheric Emission Spectrometer Measurements of HDO and H_2O

4.1 Abstract

The amount and isotopic composition of water vapor measured by the Tropospheric Emission Spectrometer (TES) is used to characterize localized moistening and dehydration of the low to mid-troposphere. A Lagrangrian mass transport model that is constrained by specific humidity values and water isotopic ratios from TES is utilized to estimate atmospheric mixing rates, moistening efficiency, the humidity and isotopic composition of regional source waters, and effective isotopic fractionation occurring during condensation events. Most regions are shown to have moistening efficiency increase with local turbulence and convection, with wintertime subtropical moistening twice as sensitive to these effects as other regions. Over monsoonal areas, however, very intense mixing is found to deplete local source waters through post-condensational exchange, leading to decreased moistening efficiency in the 500-825 hPa layer. The underlying physics that emerge through isotopic analysis implicate reversible moist adiabatic processes (i.e. cloud "burn-off") and warm season post-condensational exchange as dominant moistening features in the subtropical lower- to mid-troposphere, while in the tropics the seasonal reversal of the monsoon dictate the characteristics of convective moistening. The results quantify regional variability in moistening efficiency (i.e., fractional increases in atmospheric moisture) due to localized mixing, which is climatically important because this quantity influences the water vapor feedback. The degree to which the effects of localized

mixing on the large-scale vapor budget are imprinted in the observed regional isotopic composition provides a measure of the usefulness of assimilating satellite observations into more comprehensive isotope-enabled General Circulation Models.

4.2 Introduction

Isotopic fractionations that occur during phase changes introduce variability in the distribution of isotopic ratios in water vapor. At equilibrium, the higher vapor pressure of HDO compared to that of H_2O results in a higher relative concentration of the heavy isotopes (HDO) in the condensed phase [*Dansgaard*, 1964; *Craig and Gordon*, 1965]. The isotopologues of water are also fractionated due to differing rates of diffusive transport during evaporation and condensation events [*Craig and Gordon*, 1965; *Jouzel and Merlivat*, 1984; *Cappa et al.*, 2003]. Thus, observations of water vapor isotopic ratios reveal past moisture exchanges between water phases rather than the state measured by water vapor alone and, in conjunction with a firm understanding of isotopic controls, can therefore lend insight into important atmospheric processes that are not currently well measured.

Numerous processes control the isotopic composition in water vapor, and many important processes are not yet fully understood and quantified [*Angert et al.*, 2008]. It is well known that the standard Rayleigh interpretation of a disconnected, condensing air mass fails to describe the processes that control water isotopic ratios over tropical land [*Worden et al.*, 2007; *Brown et al.*, 2008], and this failure is commonly attributed to stronger isotopic effects from surface fluxes then from distillation [*Hendricks et al.*, 2000; *Noone*, 2008b]. The effects of air mass mixing, re-evaporation of precipitation, and post-condensation isotopic exchange also introduce non-

Rayleigh isotopic variability of the residual vapor [*Webster and Heymsfield*, 2003; *Lawrence et al.*, 2004; *Schmidt et al.*, 2005; *Worden et al.*, 2007; *Brown et al.*, 2008; *Wright et al.*, 2009b; *Field et al.*, 2010]. While comprehensive, isotope-enabled General Circulation Models (GCMs) parameterize many of these processes, it remains a challenge to reproduce the observations from satellite-based, and other, sensors. Recent analyses have responded to this challenge by using satellite-derived ratios of deuterium (HDO) to $H_2{}^{16}O$ (hereafter, H_2O) in water vapor in simple models to provide important fingerprints of atmospheric processes [*Zakharov et al.*, 2004; *Herbin et al.*, 2007; *Payne et al.*, 2007; *Worden et al.*, 2007; *Brown et al.*, 2008; *Noone*, 2008b]. However, further studies of mixing and post-condensational exchange processes, and their effects on the isotopic distribution, are needed to provide more comprehensive assessment of hydrologic cycles using observed water vapor isotopes.

Resolving the balance of moistening processes over convection regions is an important, and active, area of study. In regions of convection, Mapes et al. [2009] showed that the lower troposphere tends to dry out in GCMs while the observations show moistening. Similarly, using trajectory analysis, Wright et al. [2009a] found anomalous moistening in parcels that cross convective regions. Fu at al. [1999] showed strong seasonal variability in the partitioning of moistening from condensate evaporation, horizontal transport, and vertical transport over the convective Amazon region. The isotopic composition of water is sensitive to changes in convective activity and organization [*Lawrence and Gedzelman*, 1996; *Gedzelman et al.*, 2003; *Lawrence and Gedzelman*, 2003; *Lawrence et al.*, 2004], and rainfall re-evaporation during such storms influences tropospheric water vapor isotopic ratios [*Worden et al.*, 2007; *Bony et al.*, 2008; *Risi et al.*, 2008a; *Risi et al.*, 2008b]. This study exploits the sensitivity of isotopic ratios to differential moistening processes during convection to provide a comprehensive assessment of regional low to mid-tropospheric hydrology.

The dominant source of moistening on subsiding air in the intertropical belt is important to resolve since water vapor feedback is very sensitive to fractional increases in water vapor. In subsiding tropical air, Sun and Lindzen [1993] found condensate evaporation to be the dominant moistening process while a study by Yang and Pierrehumbert [1994] found moistening by cross isentropic mixing (i.e. convective mixing) dominant. More recent work [*Couhert et al.*, 2010] showed that convective vertical transport substantially impacted the moistening over subtropical dry regions during the Northern Hemisphere winter, with condensate evaporation playing a secondary role; additionally, this study found that convective transport alone dominated the moistening in the summertime Southern Hemisphere subtropics. Using isotopic analysis, studies have found roughly 20-50% of rainfall evaporating near convective clouds, and that the resultant moistening contributes substantially to mid-tropospheric humidity [*Worden et al.*, 2007; *Wright et al.*, 2009b]. The present study extends our understanding of the dominant regional moistening processes in these climatically sensitive regions by using isotopic analysis to leverage local moistening influences from convective mixing, cloud processes, and post-condensational exchange.

Several studies have shown that local sources of water vapor exert a significant influence on tropospheric water vapor ratios at a variety of scales. For example, Angert et al. [2008] revealed that changes in vertical transport were responsible for a significant proportion of the seasonality of isotopic measurements of water vapor over the eastern Mediterranean, which was not reproduced by an isotope enabled GCM. On a larger scale, Worden et al. [2007] and Brown et al. [2008] found that lower tropospheric water vapor was more enriched over land than over oceans in tropical locales, indicating stronger mixing between the boundary layer and free troposphere over land. These studies provide insight into the dominant processes that control water isotopic ratios, yet the partitioning between local versus large-scale moistening influences on regional isotopic composition in the troposphere has not been thoroughly quantified using observations.

Cloud processes are important for the humidity budget. For example, modeling studies reveal that evaporating cumuli moisten subsiding air at atmospheric levels below 500 hPa [*Gamache and Houze*, 1983; *Betts*, 1990; *Sun and Lindzen*, 1993]. The rehydrating effect of cloud evaporation is often neglected in advection-condensation models [e.g., *Sherwood*, 1996; *Pierrehumbert and Roca*, 1998; *Galewsky et al.*, 2005; *Galewsky and Hurley*, 2010; *Hurley and Galewsky*, 2010b], since this effect is likely to occur during last saturation [*Sherwood et al.*, 2010b]. The degree of regional cloud dissipation is directly related to the precipitation efficiency (defined here as the fraction of cloud water that is converted to precipitation), which has important effects on tropical humidity [*Bony and Emanuel*, 2005], and tropical cirrus formation and the associated radiative balance [*Lindzen et al.*, 2001]. Isotopic ratios found in water vapor are sensitive to precipitation efficiency [*Lee et al.*, 2010; *Noone*, 2010] since net fractionation occurring during reversible moist adiabatic processes (i.e., cloud evaporation) is less than that which occurs when condensate is immediately removed (i.e., a Rayleigh model) [*Merlivat and Jouzel*, 1979]. This study compares net fractionation occurring during cloud processes with precipitation efficiency deduced from moisture loss (found from a mass budget) and Tropical Rainfall Measuring Mission (TRMM) precipitation rates, and thus provides an assessment of the ability of isotopic information in water vapor to deduce important dehydration processes.

The isotopic fingerprint of moisture recycling during intense convection has been found to be related to post-condensational isotopic exchange in studies using models [*Risi et al.*, 2008a; *Wright et al.*, 2009b; *Field et al.*, 2010] and observations [*Worden et al.*, 2007; *Lee et al.*, 2010]. This effect is attributed to additional depletion of residual vapor following condensation that occurs during isotopic exchange with, or evaporation of, precipitation. Risi et al. [2008a] proposed that the anomalously depleted water vapor was reintroduced into the storm via a connection between unsaturated downdrafts and the subcloud layer. The authors also found that this modeled mechanism could quantify the "amount effect", which is isotopic depletion of convective precipitation that exceeds Rayleigh distillation expectations [*Dansgaard*, 1964; *Rozanski et al.*, 1992; *Araguas-Araguas et al.*, 1998] and produces a well documented signal in ice cores near monsoonal regions [*Wushiki*, 1977; *Grootes et al.*, 1989]. This study uses TES observations within a mass budget to illustrate regions where increased net isotopic fractionation rates are evident, and further relates these values to key moistening processes.

The objectives of this study are thus to make use of regional distributions of the isotopic composition of water vapor to identify and explain the dominant, regional moistening and dehydration processes for the mid-troposphere over land and ocean. Results from a Lagrangian mass transport model, which is constrained by HDO and H_2O measurements observed from the NASA Tropospheric Emission Spectrometer (TES), quantify atmospheric mixing timescales, moistening efficiency (defined as the fractional increase in tropospheric humidity due to local moistening), precipitation efficiency, and effective isotopic fractionation occurring during cloud processes, while also serving to explain the seasonal isotopic distributions measured from TES in a simple framework. Results are combined with the moisture budget partitioning described by Trenberth et al. [1999] to quantify contributions of local versus large scale contributions to the isotopic distributions derived from the TES observations. In the following section the TES data specifications and the Lagrangian budget method are described. The components of HDO and H_2O derived in the budget calculations are described in Section 4.3, while constraints on the budget calculations are discussed in Section 4.4. Section 4.5 provides an analysis of regional mixing rates, as well as moistening and dehydration processes. Remarks and conclusions are presented in Section 4.6.

4.3 Methods

4.3.1 TES Data Specifications

TES on NASA's Aura spacecraft provides global-scale observations of the isotopic composition of water vapor in the mid-troposphere with global coverage. Data used for this study comes from the TES nadir observations, which observes a column of the atmosphere with a footprint of approximately 5.3 km x 8.3 km. Additional selection of the Version 3 data is required to ensure only high quality and physically meaningful retrievals are used [*Worden et al.*, 2007]. The TES HDO/H_2O ratio estimates have peak sensitivity near 700 hPa, and the sensitivity decreases with latitude through its dependence on temperature and water amount [*Worden et al.*, 2006]. The precision of the H_2O estimates is ~20% with a wet bias of ~5% for the 500-825 hPa atmospheric layer [*Clough et al.*, 2006]. The precision of ~1.5% on the tropospheric HDO/H_2O ratio is made possible from a joint retrieval algorithm that allows partial cancellation of systematic errors common to both HDO and H_2O; however, a high bias of ~5% in the HDO/H_2O ratios [*Worden et al.*, 2006] is accounted for in this study. Average specific humidity [q, (g/kg)] and isotopic ratio (*R*) values are found at the TES observation locations using mass weighted averages from the respective TES profiles for the 500-825 hPa layer.

4.3.2 Back Trajectory Segments

Moisture budgets are computed along trajectory paths from some upstream location to a final downstream location. In order to constrain this budget, a search is made to find pairs of observations that are connected via back trajectories. The back trajectory model [*Noone and Simmonds*, 1999; *Brown et al.*, 2008] runs from each TES observation location from September, 2004 to March, 2008 (888,158 individual observations, using both Special Observation and Global Survey data) using three-dimensional wind fields from NCAR/NCEP Reanalysis data [*Kalnay et al.*, 1996], and assuming an arrival height of 662.5 hPa (nominally in the middle of the 500-825 hPa layer). TES observations that occur within 90 minutes and within a circle of radius 120 kilometers along the one to three day portions of the back trajectories are found (hereafter crossings), with the values of q and R at the crossings calculated by using mass weighting over a 325 hPa thick layer centered at the parcel pressure level. The result is 173,788 one-to-three day back trajectories with endpoints in three-dimensional space. At these points, mass weighted q and δD values found for a 325 hPa thick layer that is vertically centered on the trajectory end point. Of these, 28,289 trajectories are found in December-January-February (DJF) and 75,885 trajectories are found during June-July-August (JJA). The higher density of JJA trajectories is a result of numerous special observations (additional TES measurements occur during scientific campaigns) over the mid-latitudes of the Northern Hemisphere during summer.

Budgets are evaluated at each point on a 5° latitude by 5° longitude grid over the domain 0°E-360°E and 40°S-40°N using information from all trajectories that arrive within 600 kilometers of the center of the grid point in each season (JJA or DJF). The choice of a 600 km radius yields 90% of the grid points having between 19 and 334 trajectories with a mean of 99 trajectories at each grid point. Results calculated from grid points having less than 10 trajectories are omitted. Figure 4.1 shows the number of trajectories used for the Lagrangian model for each gridpoint on a 5° by 5° grid in each season. Since TES retrievals are more often successful over ocean, there is a higher density of trajectories over water. The unsuccessful retrievals over land surfaces are a result of multi-layer clouds, which cause the infrared emissions from the surface to be obscured and often lead to unusable retrievals. A large portion of the Sahara Desert, a section of interior Australia during DJF, and a northern section of the Gobi desert have fewer trajectories arriving than are needed to constrain the model. However, trajectories that begin in or intersect these regions, and that ultimately arrive in grid points with more available data, give information on the hydrology of those regions when results are mapped onto a grid from the trajectory paths. An example of the seasonal trajectories used to constrain a single grid point estimate (Figure 4.2) illustrates a grid point north of South America during December-January-February (DJF) whose parcels primarily gain water *en route* from the Atlantic Ocean (Figure 4.2b), while also becoming more enriched with HDO (Figure 4.2c).

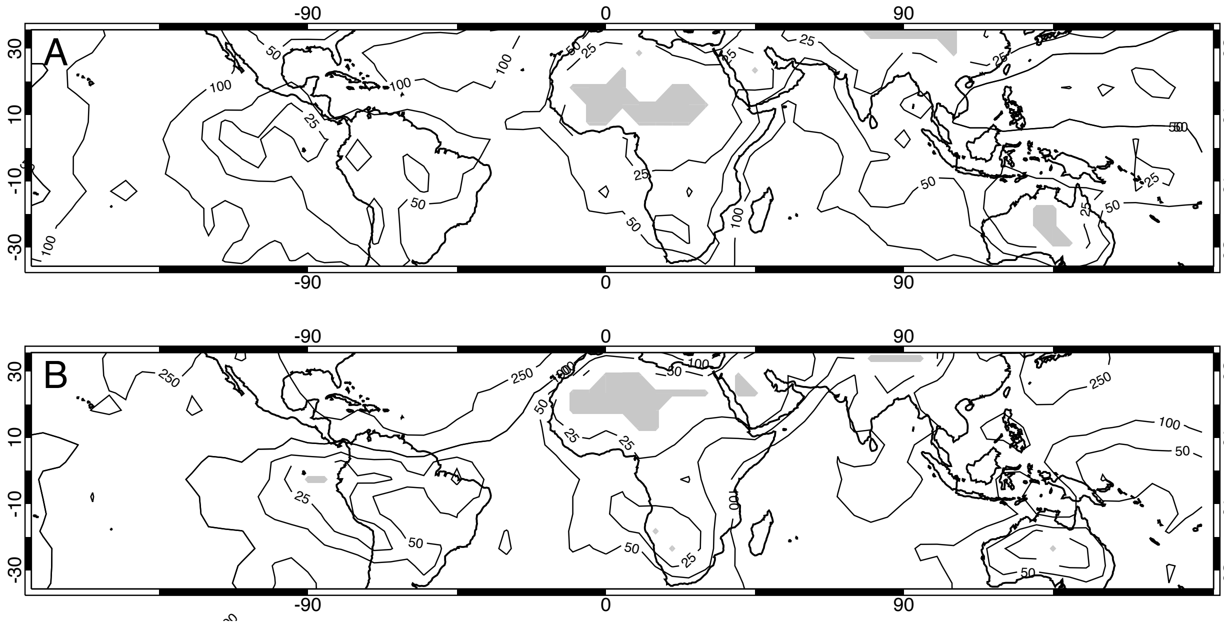

Figure 4.1: Number of seasonal trajectories in the Lagrangian model that arrive within a 600 km circle on a 5° by 5° grid for a) DJF and b) JJA. Grey shading indicates grid points where fewer than ten trajectories are available. Trajectories that arrive at these grid points are not used in this study.

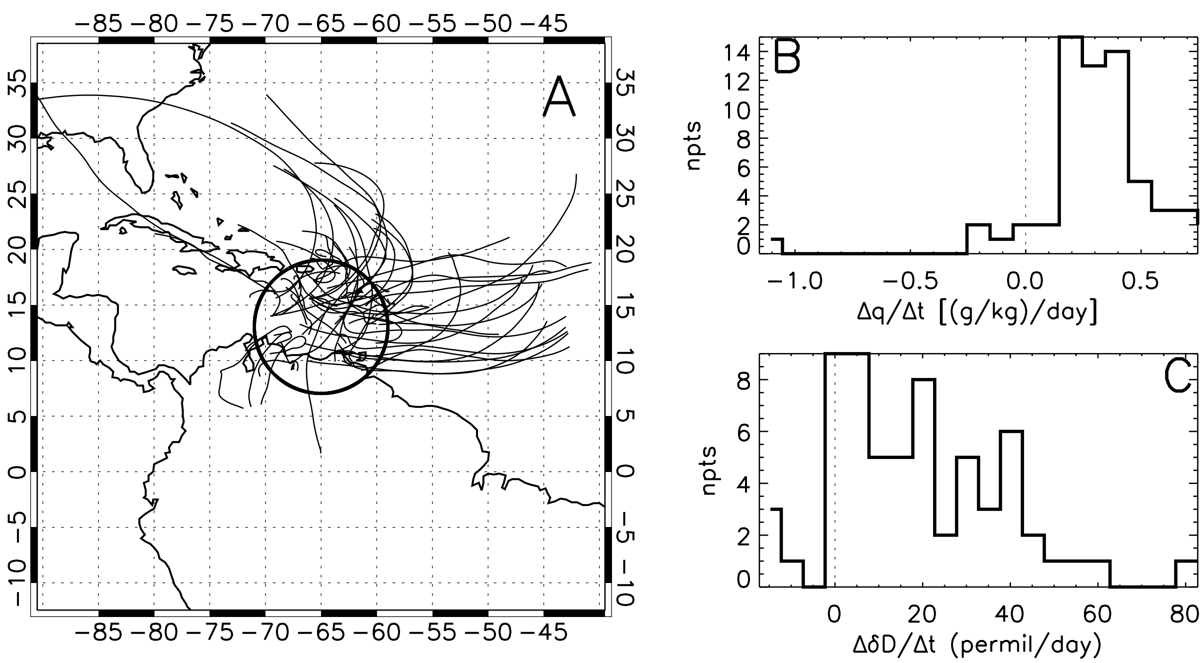

Figures 4.2: Example of individual trajectories used to constrain the isotopic model for one gridpoint (a), with histograms of the changes in moisture (b) and *δD* (c) *en route*.

4.3.3 Lagrangian Mass Transport Model

The Lagrangrian model differs from pure advection-condensation models which have been used extensively for water vapor studies [e.g., *Sherwood*, 1996; *Pierrehumbert and Roca*, 1998; *Galewsky et al.*, 2005; *Galewsky and Hurley*, 2010; *Hurley and Galewsky*, 2010b], because it accounts for mixing processes *en route*. The model allows for exchanges between air parcels and local moisture sources, thereby exposing the effects that convective and turbulent mixing have on the parcels' moisture and isotopic composition.

The H_2O mass mixing ratio (q) along some trajectory evolves as

$$\frac{dq}{dt} = G_q - L_q = k(q_s - q) - aq \tag{E4.1}$$

where G_q is the gain of water vapor into the parcel from a nearby moisture reservoir (q_s), and L_q is the rate of loss of water from the parcel, and finite changes along the trajectory endpoints (i.e., Dq over a trajectory of Δt (days) duration) is of ultimate concern. The calculation of moisture gain is described by two-member mixing while the linear form for moisture loss is identical to that expected for Rayleigh distillation. The rate of moistening and condensation, given by the exchange parameters k and a (in units of days^{-1}), and the source specific humidity parameter, q_s, are free parameters.

For the isotopic composition, it is convenient to construct the budget in terms of the HDO mass mixing ratio (x=Rq, where the mole ratio of isotopologues is R=g[HDO]/[H_2O], and g is the ratio of molecular weights of the two species [i.e., g = 18/20]) in analogy to Equation 4.1 as

$$\frac{dx}{dt} = G_x - L_x = k(x_s - x) - a\alpha x \qquad \text{(E4.2)}$$

where the terms G_x and L_x are the rate of supply of HDO from the source to the parcel, and the loss of HDO from the parcel via precipitation, respectively. Equation 4.2 contains two additional free parameters; the amount of HDO at the source (x_s), and the effective isotopic fractionation during condensation (α).

The continuous Equation 4.1 may be integrated between some initial (q_0) and final (q_{mod}) points along a Lagrangian trajectory path of length Δt, and yields the solution

$$q_{\mathrm{mod}} = q_0\hat{e} + (1-\hat{e})\hat{q} \qquad \text{(E4.3)}$$

where $\hat{q} = kq_s/(k+a)$ and $\hat{e} = \exp[-(k+a)\Delta t]$. In Equation 4.3, q_0 is the specific humidity at the upstream TES observation, while q_{mod} is the final modeled value of specific humidity at the downstream endpoint of the trajectory and is evaluated by selecting free parameters k, a, and q_s.

Similarly, integrating Equation 4.2 along the trajectory path, the isotopic model has the solution

$$x_{\mathrm{mod}} = x_0\hat{e}_x + (1-\hat{e}_x)\hat{x} \qquad \text{(E4.4)}$$

where $\hat{x} = kx_s/(k+a\alpha)$ and $\hat{e}_x = \exp[-(k+a\alpha)\Delta t]$. In Equation 4.4, x_0 is the amount of HDO at the trajectory point upstream, while x_{mod} is the final modeled amount of HDO at the downstream endpoint of the trajectory and similarly to the case for q_{mod} , is evaluated by choosing the parameters k, a, α, and x_s. Using the mass mixing ratios, x_{mod} and q_{mod}, the model isotope ratio is $R_{\mathrm{mod}} = \varepsilon\ (x_{\mathrm{mod}}/q_{\mathrm{mod}})$, where ε is the ratio of the molar weights of H_2O and HDO.

4.3.4 Climatological Statistics

The budget for water is closed following the selection of a, k and q_s, while the isotope budget additionally requires selection of α and x_s. For any single trajectory there are only two measurable quantities (Δq and Δx over the known finite trajectory time, Δt), and as such, the problem is under-constrained and insoluble. However, budgets can be estimated using an ensemble of individual observations to constrain the model in a seasonal mean sense. Thus, seasonal mean values of a, k, q_s, α and x_s are estimated.

Given that numerous individual observations are used over a season to constrain the model, the parameters found from the model represent seasonal mean estimates. Consider some ensemble of parcels, which represent the climatology (e.g., a season, etc.) for a given region. The mean quantities are thus

$$\overline{G}_q = \overline{k(q_s - q)} \qquad \text{(E4.5)}$$

and

$$\overline{L}_q = \overline{aq} \qquad \text{(E4.6)}$$

where the overbar is the traditional arithmetic ensemble mean, and G_q and L_q need not be equal at regional scale (i.e., G_q-L_q is the net moisture divergence for the atmospheric region of interest, taken in this study as the 825-500 hPa layer observed by TES). Defining an appropriate averaging scheme, such that mean rate constants arise,

$$\overline{L_q} = \overline{aq} = \left(\frac{\overline{aq}}{\overline{q}}\right)\overline{q} = \tilde{a}\overline{q} \qquad \text{(E4.7)}$$

thus denotes "~" as the mass weighted mean, where in general, $\tilde{a} \neq \overline{a}$. Similarly, for the mean gain of water into the parcels *en route*,

$$\overline{G_q} = \overline{k(q_s - q)} = \tilde{k}(\overline{q_s} - \overline{q}). \qquad \text{(E4.8)}$$

For the HDO budget a similar ensemble averaging is adopted:

$$\overline{L_x} = \overline{a\alpha x} = \left(\frac{\overline{a\alpha q}}{\overline{q}}\right)\overline{x} = \breve{\alpha}\left(\frac{\overline{aq}}{\overline{q}}\right)\overline{x} = \breve{\alpha}\tilde{a}\overline{x}, \qquad \text{(E4.9)}$$

with $\breve{\alpha}$ a relevant effective (mean) fractionation, which is strictly a loss-rate weighted mean rather than the usual mass weighted mean, and can be determined as

$$\breve{\alpha} = \frac{\overline{a\alpha q}}{\tilde{a}\overline{q}}. \qquad \text{(E4.10)}$$

Similarly for the gain of HDO into the parcels *en route*, the averaged definition is

$$\overline{G_x} = \overline{k(x_s - x)} = \tilde{k}(\overline{x_s} - \overline{x}). \tag{E4.11}$$

Thus, the challenge is to determine the climatological mean values of the model parameters ($\tilde{a}$, $\tilde{k}$, $\overline{q}_s$, $\overline{x}_s$, $\breve{\alpha}$) that best match the ensemble of observations that comprise the observed climatological mean specific humidity ($\overline{q_{obs}}$) and isotopic ratio ($\overline{R_{obs}}$) at the trajectory end points.

4.3.5 Parameter Estimation Approach

The problem of estimating the model parameters can be written as a minimization of the mismatch between downstream observed values (q_{obs} and R_{obs}) and the modeled values (q_{mod} and R_{mod}), given the observed upstream values of (q_0 and R_0) to initialize the mode given by Equations 4.3 and 4.4. The use of an error function that includes mass weighting is a requirement for recovering the mass and (loss) rate weighted parameters. Hence, using the individual trajectory solutions over a given region found from Equations 4.3 and 4.4, we define a cost function J, such that

$$J = \sqrt{\frac{\sum_{obs} \Theta^2 \left\{ f \left[\frac{q_{\mathrm{mod}} - q_{obs}}{q_{obs}} \right]^2 + (1-f) \left[\frac{R_{\mathrm{mod}} - R_{obs}}{R_{obs}} \right]^2 \right\}}{\sum_{obs} \Theta^2}}, \tag{E4.12}$$

where Θ is defined as the average value of q for each individual trajectory, and from observation, $\Theta=(q_0+q_{obs})/2$. The parameter f determines the relative importance of q and R and is taken here as 0.5. Notice that it is within the calculation of the modeled values that the five free model parameters appear. Minimization of the cost function, J, proceeds through iterative sequential application of the Brent [1972] method in five dimensions. Upon minimization, the optimal values for the parameters ($\tilde{a}$, $\tilde{k}$, $\overline{q}_s$, $\overline{x}_s$, $\breve{\alpha}$) are selected and used in calculation of $\overline{G}_q$, $\overline{G}_x$, $\overline{L}_q$ and $\overline{L}_x$, and consequently the isotopic ratio of water entering (R_G) and leaving (R_L) the atmospheric region of interest is found. In order to aid analysis, the final modeled isotopic ratios are converted to "delta" form:

$$\delta D=\left[\frac{R_{obs}}{R_{VSMOW}}-1\right]\cdot 1000, \qquad \text{(E4.13)}$$

where the ratio R_{VSMOW} is twice the Vienna Standard Mean Ocean Water standard (D/H ratio) and is $311.52\text{x}10^{-6}$.

The cost function value (J) at the solution (i.e. the minimum) is a measure of the variance in changes in isotopic composition and moisture amount amongst the individual water transport pathways (Equation 4.12). The choice of a linear model (Equations 4.1 and 4.2) ensures that the cost function is sufficiently smooth such that a global minimum can be found, and testing shows the solution is insensitive to the initial guesses. Figure 4.3 shows an example of the variations in the cost function values as a function of the five free parameters in the model for a single grid point. The variations in the cost functions due to changes in each parameter are shown in Table 4.1 for different regions. For each grid point, values are calculated as the percent increases in the cost function values (from their global minimum values) with a 10% change for each given parameter. The curve of the cost function with respect to each variable is asymmetric (Figure 4.3), thus perturbing in the positive and negative directions, and evaluating the change in magnitude of the cost function with each perturbation, is required to achieve a mean sensitivity of the cost function in the range of each parameter. The cost function is more sensitive to perturbations in moisture source and source isotopic composition than for any other parameter. Additionally, the tropical continental regions exhibits the highest sensitivity of the cost function with respect to all parameters, and is thus the most well constrained region for this model. Indeed there is an approximate 10% change in the cost function with the imposed 10% change in the q_s and R_s in the summer time for tropical land. This suggests that these quantities are the most robust estimates, and that analysis of these quantities can proceed with more confidence than the other three parameters. Neither of the remaining 3 parameters (k, a and α) stand out as particularly well or poorly constrained. However, the least constrained regions are over ocean in the midlatitudes, which is likely associated with the larger variability that is typical in those regions.

The distribution of the cost function minima (Figure 4.4) illustrates in which geographic regions we can be more confident that the seasonal mean estimates represent the net moisture processes that occur along the individual trajectories. The cost function values at the solution point (i.e. minimum) quantify the degree to which the individual q and R values at the trajectory arrival point vary from the respective modeled values using the seasonal mean parameters. In Figure 4.4, the numerical values are a measure of the standard deviation between individual trajectories values. However, the uncertainties on the mean estimates can be approximated by dividing by the square root of the number of trajectories resolved for each point. Given that the average number of trajectories per grid point is ~100, the uncertainty on the mean estimates are

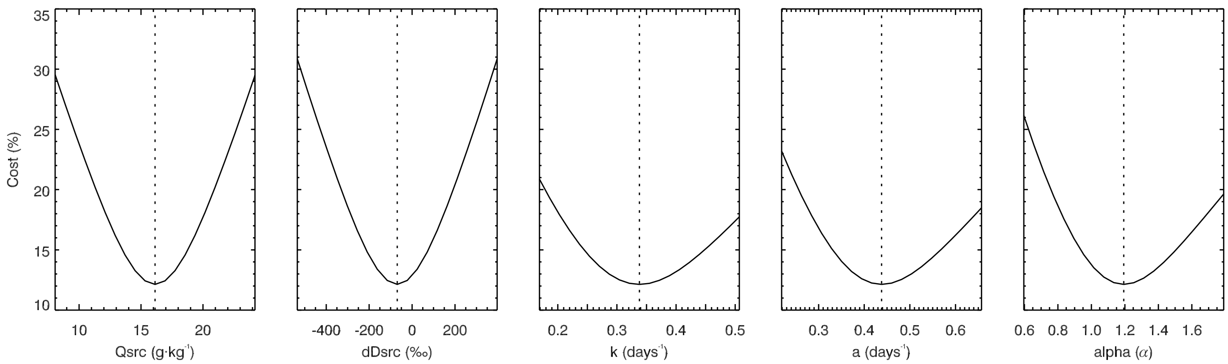

Figure 4.3: Cost function values versus free model parameters for an individual grid point. Dashed lines indicate the values of the parameters at the cost function minima.

	DJF			JJA		
NH	*30°-40° N*	*15°-30° N*	*0°-15° N*	*30°-40° N*	*15°-30° N*	*0°-15° N*
q_s	1.4 (1.7)	1.6 (1.6)	**3.3** (**4.6**)	1.9 (**3.0**)	**4.4** (**4.3**)	**6.6** (**10.0**)
R_s	1.6 (2.0)	1.9 (1.9)	**3.6** (**4.9**)	2.1 (**3.3**)	**4.7** (**4.7**)	**7.0** (**10.6**)
k	0.5 (0.6)	0.7 (0.7)	1.1 (1.7)	0.7 (1.3)	1.6 (1.5)	1.7 (2.2)
a	0.7 (0.7)	0.6 (0.6)	1.2 (1.4)	0.7 (1.1)	1.6 (1.8)	1.9 (2.7)
α	0.9 (0.9)	0.7 (0.7)	1.4 (1.6)	0.8 (1.2)	1.8 (2.1)	2.3 (**3.2**)
SH	*30°-40° S*	*15°-30° S*	*0°-15° S*	*30°-40° S*	*15°-30° S*	*0°-15° S*
q_s	1.1 (1.1)	2.0 (**3.4**)	**4.3** (**9.2**)	1.6 (1.7)	1.6 (1.7)	**3.4** (**4.6**)
R_s	1.3 (1.4)	2.3 (**3.8**)	**4.7** (**9.8**)	1.9 (2.1)	1.9 (2.1)	**3.7** (**5.0**)
k	0.4 (0.5)	0.8 (1.3)	1.5 (1.9)	0.6 (0.6)	0.7 (0.8)	1.3 (1.9)
a	0.5 (0.4)	0.7 (1.4)	1.6 (2.2)	0.8 (0.8)	0.6 (0.7)	1.3 (1.8)
α	0.7 (0.5)	0.8 (1.7)	1.9 (2.7)	1.0 (1.0)	0.7 (0.8)	1.5 (2.0)

[a]Values without parentheses are for ocean and those in parentheses are for land. Bold values show where there is at least a 3% change in the cost function for the 10% perturbation in the parameter.

Table 4.1: Average percent increase in the cost function from solution minima for a ±10% change in each model parameter for DJF and JJA.[a]

roughly an order of magnitude lower than the values shown in Figure 4.4, and are explicitly calculated in Section 4.3.6, below. Areas where the seasonal variance in moisture and isotopic composition changes *en route* is small will have a cost function minimum that is low. The tropical regions generally show low cost function minima, with the lowest values occurring over the monsoonal regions. This is consistent with a highly predictable, and long-term seasonal surge of tropical moisture. On the other hand, the baroclinic midlatitude regions show relatively higher cost function minima. This is likely a result of synoptic scale disturbances introducing variability in moisture and isotopic composition changes among the interseasonal trajectories. Our analysis focuses on the tropics and subtropics, where the estimates are better constrained.

4.3.6 Mean and Error Estimates by Ensemble Method

Uncertainties on the estimated parameters are determined via a Monte-Carlo method based on the known error estimates for q and R found from the TES retrievals. The retrieval error estimates of q and R at both the upstream and arrival sites (i.e., the trajectory endpoints) are multiplied by normally distributed random numbers with ±1 standard deviation and then added to the original TES q and R values of each trajectory in order to create the 500 member Monte Carlo ensemble. This approach is consistent with the TES error estimates, which assume Gaussian statistics in the retrieval. Using these normal distributions (N = 500, σ = retrieved error), final estimates of the mean and uncertainty at each grid point are calculated as the mean and standard deviation of the 500 ensemble members. Since the gain and loss terms act over the duration of the trajectory length, the parameter estimates are mapped along the ensemble of trajectory paths rather than being assigned just to the location of the end point on the 5º by 5º

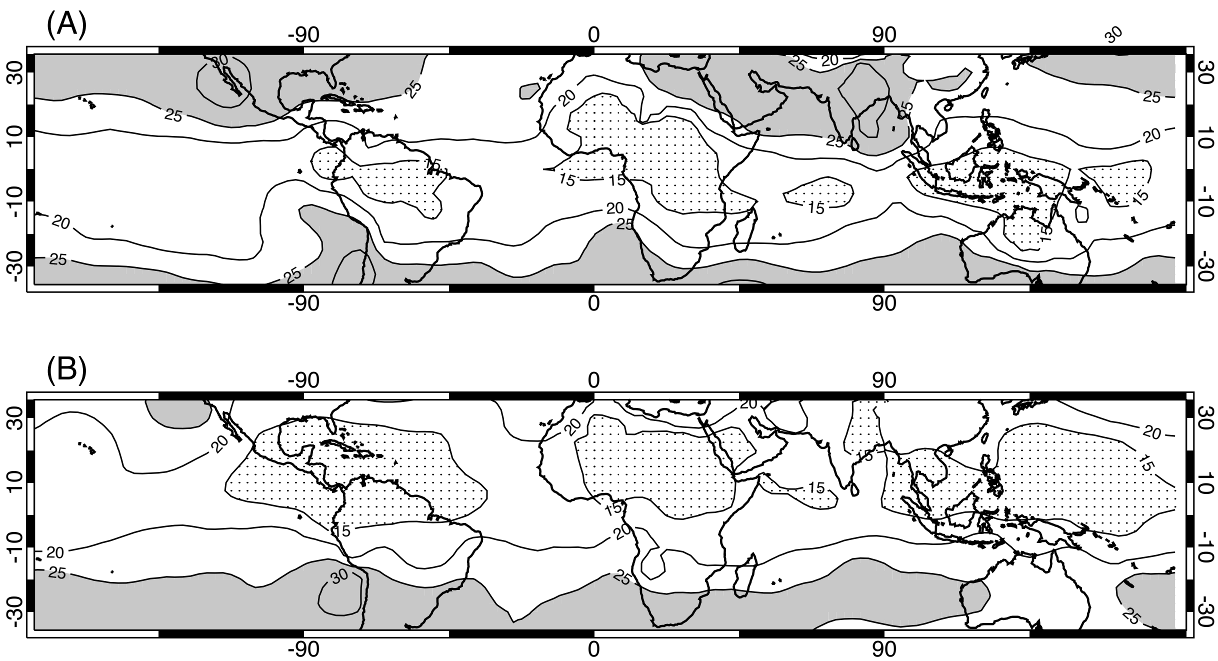

Figure 4.4: Cost function minima (%) for a) DJF and b) JJA. Areas with the cost function minimum values exceeding 25% are grey shaded, while areas with values below 15% are stippled.

grid. The estimates associated with the trajectories are binned onto a 2.5º by 2.5º grid using a Cressman weighting interpolation scheme with an effective mean radius 600 km.

Table 4.2 shows mean values for land and ocean zones for several parameters, along with the average errors of the means that occur as a result of the ensemble averaging explained above. Average errors of the mean are calculated as $\overline{\sigma} = \sigma/\sqrt{n}$ where n is the number of ensemble members, and σ is the standard deviation amongst the 500 ensemble members. In Table 4.2, land regions show a greater error (roughly twice as large) on the means than the oceanic regions. This discrepancy is largely due to fewer observations over land, which is a result of lower quality retrievals occurring more often over land due to multi-layer clouds and surface emissivity anomalies [*Worden et al.*, 2004]. However, the fractional error on the mean of all parameters is less than 1%. The uncertainty on the calculated δD values of the moisture losses and gains (δD_G and δD_L) are largest, at roughly 2-6‰.

Beyond uncertainty, other potential sources of error are associated with the spatial and temporal distribution of the trajectories, and that TES measurements are biased toward mostly clear sky conditions. Although TES measures mostly clear sky conditions, the dominant, seasonal moistening processes that occur for each region are recorded in the isotopic distribution in the (residual) vapor nonetheless. For instance, it would be expected that clear sky, residual moisture immediately following a large storm would remain relatively depleted in HDO (e.g., from isotopic ‘rainout’) when compared with the mean isotopic composition. It is this aspect of the isotopic distribution that provides information beyond that attained from water vapor measurements alone.

Tropical Regions (0º to 15º)

Parameter	Units	land mean	land error	ocean mean	ocean error
Q_s	g/kg	12.8	0.16	12.1	0.07
dD_s	‰	-124	2.01	-137	1.01
$1/k$	days	3.17	0.05	3.79	0.03
$1/a$	days	3.21	0.08	3.10	0.03
α	unitless	1.080	0.006	1.069	0.002
G	(g/kg)/day	2.17	0.04	1.87	0.02
L	(g/kg)/day	2.27	0.04	1.97	0.02
$G-L$	(g/kg)/day	-0.09	0.01	-0.10	<0.01
dD_G	‰	-97	5.63	-112	2.24
dD_L	‰	-83	4.77	-106	2.03

Subtropical Regions (15º to 32.5º)

Parameter		land mean	land error	ocean mean	ocean error
Q_s	g/kg	9.49	0.07	8.85	0.03
dD_s	‰	-142	1.15	-154	0.57
$1/k$	days	4.06	0.03	4.31	0.01
$1/a$	days	3.45	0.06	3.24	0.02
α	unitless	1.066	0.003	1.053	0.001
G	(g/kg)/day	1.56	0.02	1.31	0.01
L	(g/kg)/day	1.62	0.02	1.22	0.01
$G-L$	(g/kg)/day	-0.06	<0.01	0.09	<0.01
dD_G	‰	-121	2.97	-138	1.05
dD_L	‰	-114	2.72	-133	1.19

Midlatitude Regions (32.5º to 40º)

Parameter		land mean	land error	ocean mean	ocean error
Q_s	g/kg	7.88	0.03	5.50	0.01
dD_s	‰	-157	0.82	-169	0.49
$1/k$	days	3.95	0.02	3.82	0.01
$1/a$	days	2.98	0.03	2.90	0.01
α	unitless	1.059	0.002	1.062	0.001
G	(g/kg)/day	1.26	0.01	0.83	<0.01
L	(g/kg)/day	1.26	0.01	0.89	<0.01
$G-L$	(g/kg)/day	0.01	<0.01	-0.06	<0.01
dD_G	‰	-137	2.44	-150	1.07
dD_L	‰	-133	1.64	-140	0.94

[a]See Section 4.3.6. Values represent combined DJF and JJA averages.

Table 4.2: Means, and uncertainties on the means, for the Monte-Carlo ensemble.

4.4 Budget Constraints

4.4.1 Changes in Moisture Along the Trajectories

Figure 4.5 shows the mean Lagrangian changes in moisture [$\Delta q/\Delta t$ in units of (g/kg)·day^{-1}] derived from trajectory crossings, which are identical to *G-L* values calculated *a posteriori* using the estimated parameters. In broad terms, moisture losses tend to occur over the monsoonal regions, while moisture gains primarily occur in the subtropics. Comparisons (Figure 4.6) between the trajectory $\Delta q/\Delta t$ values with first, NCEP-NCAR Reanalysis seasonal moisture flux convergence (hereafter MFC) values for the 500-825 hPa layer, and second, collocated Reanalysis $\Delta q/\Delta t$ show map correlation coefficients of 0.73 and 0.92, with normalized root mean square differences of 9.8% and 5.0%, respectively. The MFC values were smoothed using a radius of 600 kilometers for consistency with the Lagrangian model's native resolution. The collocated NCEP $\Delta q/\Delta t$ values are found simply by replacing the trajectory endpoint TES q values with those from the Reanalysis, and recalculating the moisture budget using the methods in Section 4.3. Zonal mean values derived from the (TES) trajectory budget are generally higher by 0.05-0.1 (g/kg)/day, with smaller differences between TES-derived values and the two datasets during JJA from 0º-10ºS and 20º-30ºN, during DJF from 13º-40ºN, and at the latitudes of zero moistening during both seasons.

An exact agreement between the TES $\Delta q/\Delta t$ and the NCEP MFC is not expected due to spatial and temporal sampling biases, however the comparison demonstrates the Lagrangian model's ability to represent the seasonal mean hydrologic cycle. These sampling biases are reduced by using the collocated values, where differences here primarily occur through

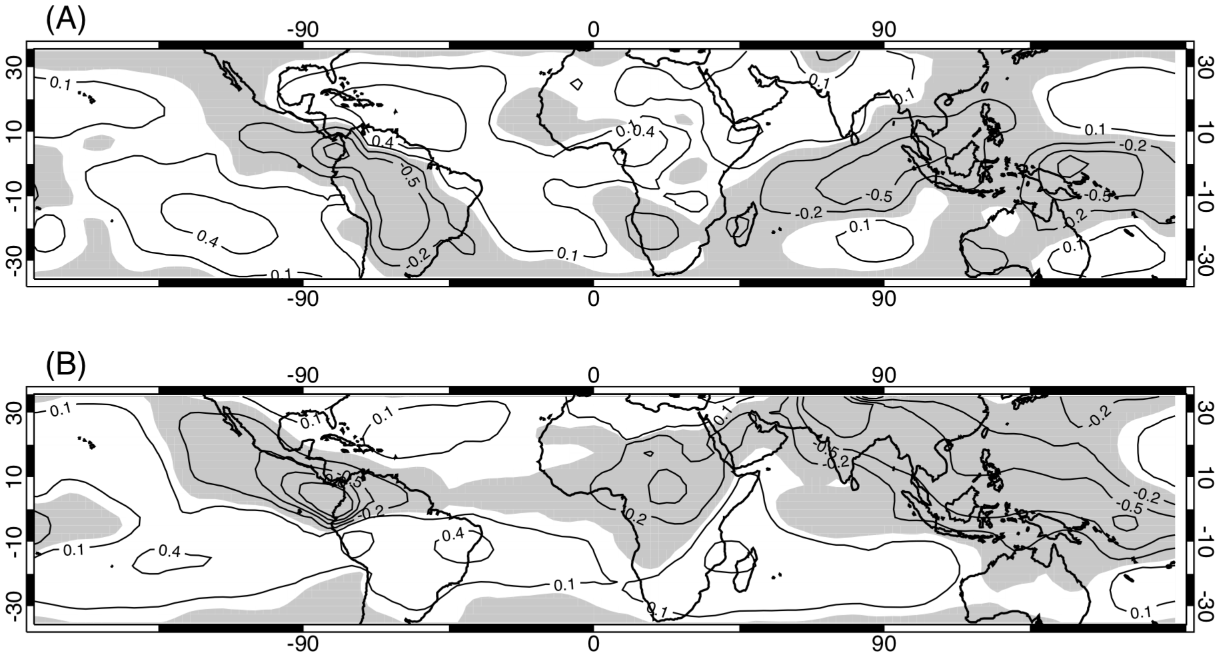

Figure 4.5: Average rate of change in specific humidity for the set of trajectories arriving at each grid point for a) DJF and b) JJA. Line contour interval is 0.3 $g \cdot kg^{-1} \cdot day^{-1}$. Grey shading indicates negative values.

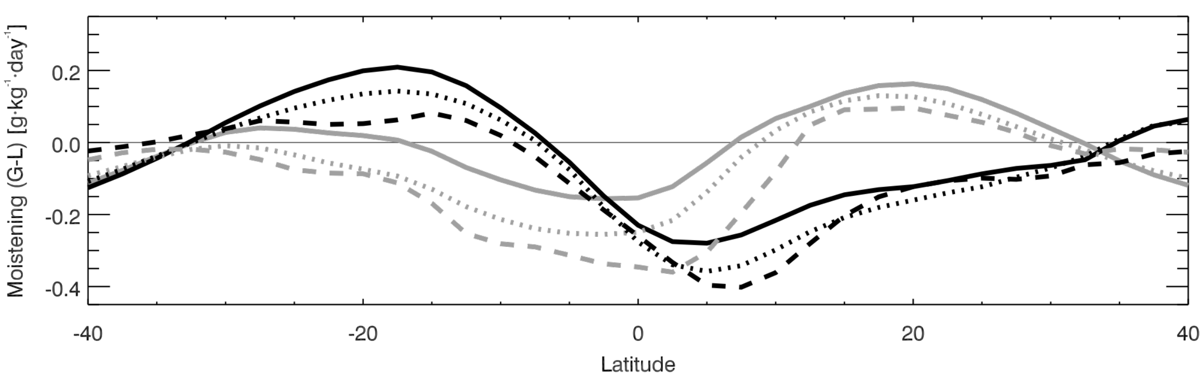

Figure 4.6: Model *G-L* values (solid), 500-825 hPa net convergence values from the NCAR/NCEP Reanalysis (dashed), and NCAR/NCEP reanalysis $\Delta q/\Delta t$ (collocated with TES retrievals; dotted) during DJF (grey) and JJA (black).

differences in vertical moisture profiles. Fractional differences between TES and Reanalysis specific humidity values at 662.5 hPa over the ranges 15ºS-15ºN, 15º-32.5ºN/S, and 32.5º-40ºN/S are 7.9% (TES more humid), 9.9%, and -2.2%, respectively. TES water vapor validations with Cryogenic Frostpoint Hygrometers have shown TES measurements to be 5-10% higher below 700 hPa, and 5-40% higher between 300 and 700 hPa [*Shephard et al.*, 2008]. However, Trenberth and Guillemot [1998] showed the NCEP-NCAR Reanalysis to be too dry in the tropics when compared with NASA Water Vapor Project (NVAP) data. Nonetheless, Figure 4.6 and the map correlation coefficients provide confidence that the main seasonal features of the water cycles from 40ºS to 40ºN are captured in the simple trajectory budget model.

4.4.2 Changes in Isotopic Composition Along the Trajectories

The average rate of change in mean δD (‰/day) for each set of trajectories is shown in Figure 4.7 and one can immediately see differences in the spatial distribution compared to $\Delta q/\Delta t$ values (cf., Figure 4.4), which is an indication of the unique information provided by the isotopes. R-squared values between $\Delta q/\Delta t$ and $\Delta \delta D/\Delta t$ for combined winter (JJA for 0º-40ºS, DJF for 0º-40ºN) and summer hemispheres (opposite winter) are 0.36 and 0.47, respectively. This confirms that several different processes, and not simple Rayleigh theory, dictate the spatial distribution of isotopic ratios and water vapor in these seasons. The δD values generally decrease along the moisture pathways in the area in the Intertropical Convergence Zone, but also predominantly near land regions known to experience a significant seasonal rainy season (i.e., for DJF, the Amazon Basin, northern Australia, and the Congo Basin; for JJA, Central America, Central Africa, and southeastern Asia). In these very humid regions, isotopic depletion by distillation along moisture pathways is an expected part of the regional hydrology (Recall Chapter 2, [*Brown et al.*, 2008]).

Outside of these regions, and poleward of the tropics, the δD values increase on average along the trajectories. The increases are largest over the winter subtropical oceans, an area known for large surface evaporation rates and marine cumulus [*Trenberth and Guillemot*, 1995]. In general, a steep vertical isotopic gradient in the background water vapor exists on long timescales because of the integrated history of condensation, and follows the background thermal structure [*Ehhalt et al.*, 2005]. As such, these isotopic increases *en route* over the subtropics are likely linked to low-level mixing of isotopically heavy boundary layer air with very dry and isotopically depleted subsiding air parcels; warm convection over short timescales brings enriched vapor relative to the background isotopic composition. From the model parameters, the timescales of this enrichment effect, the resultant fractional increases in regional tropospheric water vapor, and the seasonal contribution to the mean regional isotopic composition can be examined.

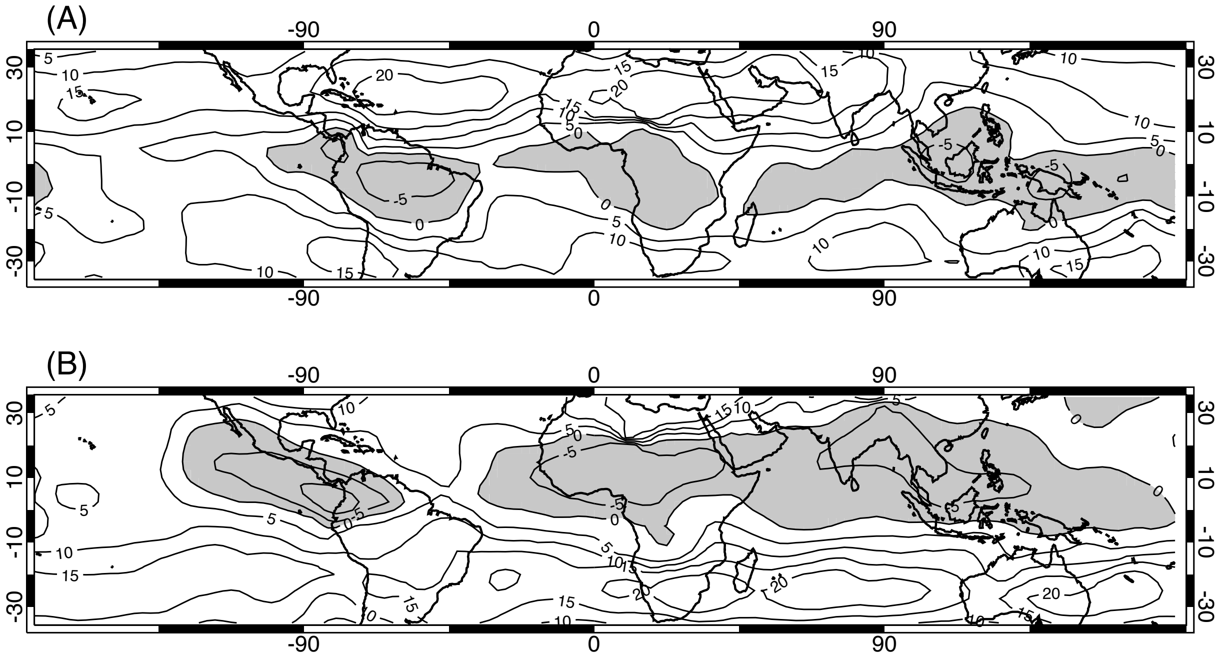

Figure 4.7: Average rate of change in δD values for the set of trajectories arriving at each grid point for a) DJF and b) JJA. Line contour interval is 5‰/day. Grey shading indicates negative values.

4.5 Moisture Sources and Exchange Processes

4.5.1 Source Moisture Amount and Isotopic Composition

Derived source specific humidity (q_s) values are shown in Figure 4.8, and each value represents the mean humidity of the airmass with which the parcels mix *en route*. Specifically, q_s is the humidity to which the atmosphere would approach through mixing in the absence of sinks. While from inspection of Equation 4.1, it is tempting to consider q_s as the saturation specific humidity at the source (i.e., as in evaporation from the ocean), these values need not be those at the surface, but can describe the humidity of residual vapor following condensation (i.e., detrained from convection), or that associated with lateral mixing. The most humid source reservoirs (i.e., q_s) exist in climatologically moist and convectively active regions, which is consistent with an expectation that these locations provide a mechanism for vertical transport to the parcels over a one to three day timeframe (e.g., the Amazon Basin, Southern Africa, and Indonesia for DJF; and China, India, and the Caribbean Sea for JJA).

The spatial patterns of the δD_s values (Figure 4.9) are similar to the q_s values in Figure 4.8 but with differences in the positions of maximum values and the steepness of the spatial gradients. For example, over the Amazon during DJF, there is a southward shift in δD_s maxima compared to q_s maxima. Since transpired water generally emerges unfractionated from that found within soil water [*Flanagan et al.*, 1991], and is typically much less depleted than marine boundary layer moisture, this southward shift in δD_s maxima may reflect moistening influences from transpired water. While this is in agreement with a study by *Trenberth et al.* [1999], that found local evapotranspiration has much greater influence on atmospheric humidity over the

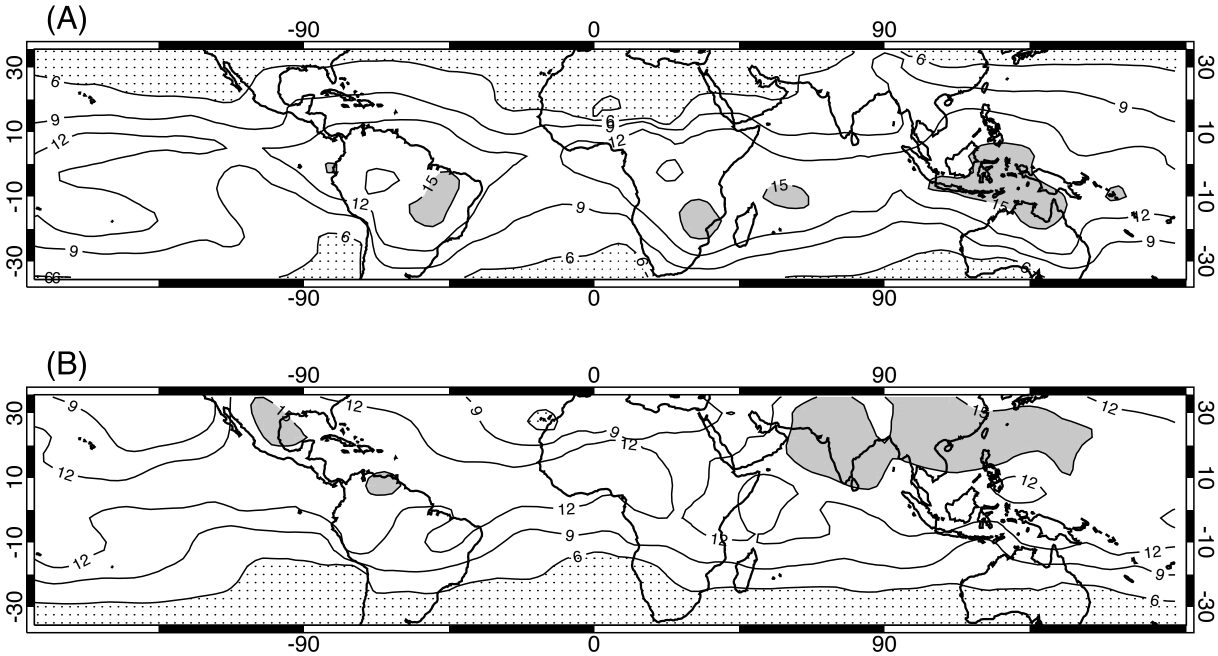

Figure 4.8: Average source specific humidity (q_s) for the set of trajectories arriving at each grid point for a) DJF and b) JJA. Line contour interval is 3 g/kg. Values greater than 15 g/kg are shaded, while those below 6 g/kg are stippled.

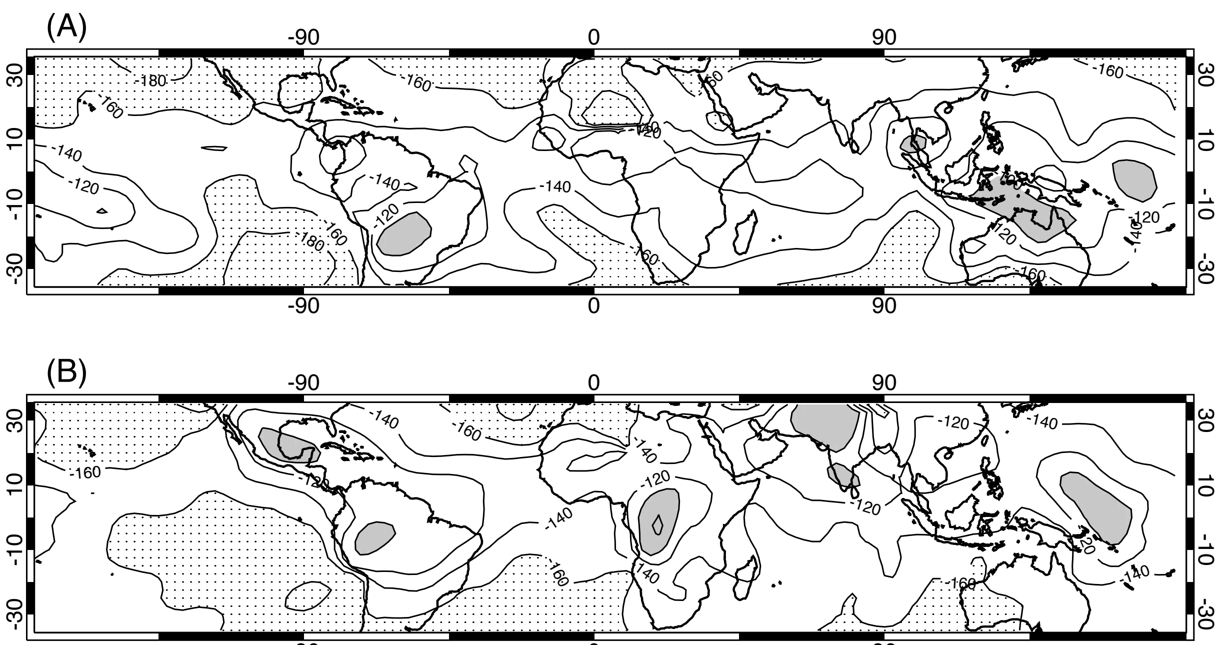

Figure 4.9: Mean isotopic composition of the source waters *(δD_s)* for the set of trajectories arriving at each grid point for a) DJF and b) JJA. Line contour interval is 20‰. Values greater than -100‰ are shaded, while those below -160‰ are stippled.

southern parts over the Amazon Basin during the wet season, the native resolution of the Lagrangian budget calculations (~600 km) prevents specific attribution. The δD_s values above -100‰, which are consistent with those expected in marine boundary layer moisture [*Craig and Gordon*, 1965], are seen over convective and moist regions: the Amazon Basin, the Congo Region, the Pacific Warm Pool, the Yucatan, and southwest of the Gobi Desert during JJA; and over the southern Amazon and Indonesia during DJF. Outside of the tropics, and especially in the subtropical high-pressure regions, δD_s values are lower, indicating source moisture with more history of condensation. The lowest δD_s values (-180‰ to -200‰) occur in areas known for seasonal subsidence (e.g., near the descending arm of the Walker Cell during both seasons, the Sahara Region during DJF, and the oceanic region west of California).

4.5.2 Local Mixing and Moistening Rates

The mixing timescales (Figure 4.10) are derived from the model as the inverse of the mixing rate parameter, k, and are the e-folding timescale for the mixing between the source and parcel moisture. The strongest mixing occurs, on average, over tropical land ($1/k$ =3.18 days, Table 4.1) and the weakest mixing occurs over the subtropical oceanic region (4.31 days). The average over summertime tropical land is even shorter (2.68 days), indicating more vigorous mixing during maximum seasonal heating. The absolute strongest mixing occurs over the terrestrial tropical convective regions (<2 days; stippled in Figure 4.10); over the Amazon Basin and the Congo Region during DJF, and over Central America's western coast, the Nile Basin in northeastern Africa, the Asian Monsoon region, and the Philippine Sea during JJA,. These values coincide with each region's monsoonal season, which is characterized by strong convection

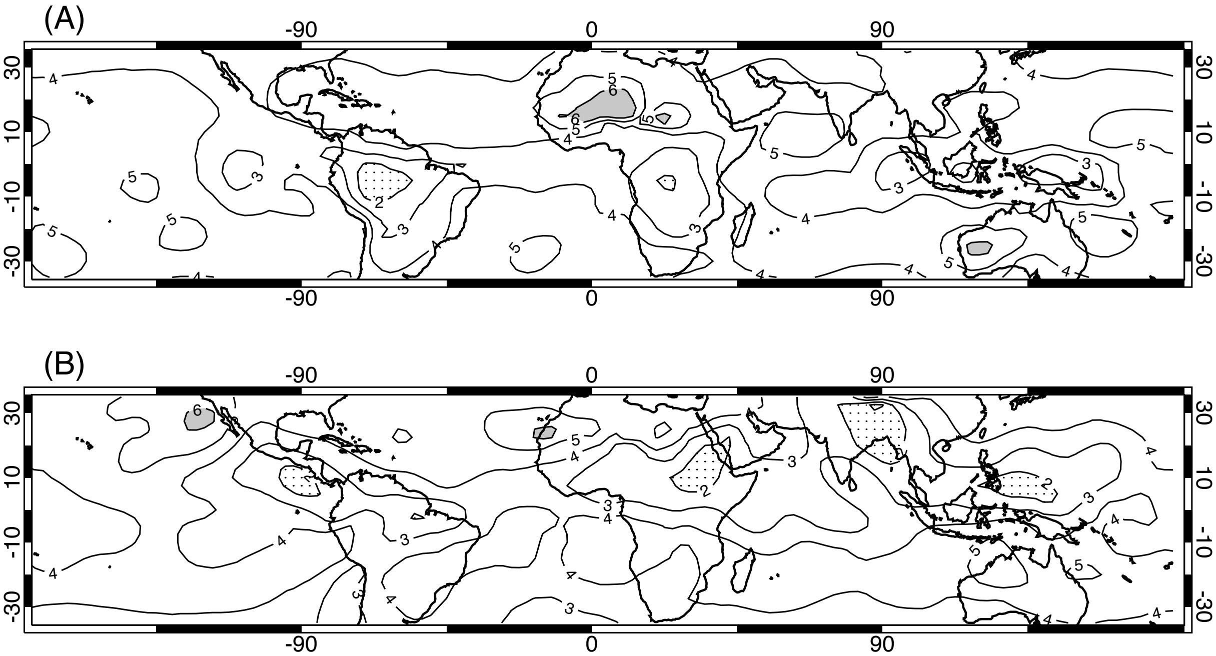

Figure 4.10: Mean mixing timescales (1/*k*) for the set of trajectories arriving at each grid point for a) DJF and b) JJA. Line contour interval is one day. Values greater than 6 days are shaded, while those below 2 days are stippled.

and high detrainment rates. Although the least depleted source moisture (high δD_s) and the fastest mixing rates (low $1/k$) are both found within monsoonal regions, their precise positions differ within the regions (compare Figures 4.9 and 4.10) . Instead, the fastest mixing in the monsoonal regions occurs with a more depleted source, which is linked to strong local distillation effects and is further evaluated in Section 4.5.3 (below).

Long mixing timescales occur in regions characterized by strong seasonal subsidence. Weak mixing in the model is generally seen over the subtropical high-pressure regions, with the weakest mixing ($1/k$>6 days, dark contouring in Figure 4.10) found over the Sahara desert's western coast during and California's west coast during JJA, and in western Australia and the central Saharan desert during DJF. In all cases except for the central Sahara region, these slow mixing rates coincide with local upwelling zones, and are consistent with low sea surface temperatures stabilizing the lower atmosphere and preventing significant low level mixing and convective transport. The low mixing rates in the central Sahara during DJF are consistent with seasonal subsidence found along the downwelling branch of the Hadley Cell. The slow mixing rates and low δD values in these regions confirm that little direct (i.e., dry) mixing occurs between the parcels and boundary layer moisture, which is expected in these regions known for seasonal subsidence.

Mixing timescales identify those regions where there is significant exchange between the source moisture and the parcels, however a moistening efficiency, M, that describes the fractional increase in large-scale moisture due to local processes can be defined as

$$M = \frac{G\Delta t}{\bar{q}}, \quad \text{(E4.14)}$$

where $\overline{q}$ is the average specific humidity value along the moisture transport pathways (i.e. the 500-825 hPa layer), G is the moistening rate (Equation 4.1), and Δt is set to one day. The relationships between regional moistening efficiency and mixing rates for each region during summer and winter are shown in Figure 4.11. During winter (Figure 4.11b), significant negative correlations (>99% confidence level) for all regions (r=-0.53, -0.27, and -0.17 for the subtropical, tropical, and midlatitude regions, respectively) show that regional moistening efficiency increases as mixing strengthens. Linear regressions show M decreases by 9.7%, 4.1%, and 2.4%, respectively, with one day increases in the mixing timescales. Thus, the efficiency of moistening for the 500-825 hPa layer in the wintertime subtropics is more than twice as sensitive to increases in mixing (e.g., shallow convection, turbulent exchange, or convective detrainment) than other regions. The wintertime subtropics represent a major global source of water for the 500-825 hPa layer (Figure 4.5), and are shown here to be sensitive to changes in local mixing.

During the summer (Figure 4.11a), significant correlations between M and mixing timescales are -0.36, 0.26, and -0.34 [regression slopes (%/day) of -2.8, 1.8, and -5.2] for the subtropical, tropical, and midlatitude regions, respectively. Thus, during the summer, the subtropical (midlatitude) M values are less (more) sensitive to mixing rates than during the winter. Winter M values are higher than summer by 8.7% in the subtropics and by 1.2% in the midlatitudes. Summertime tropical moistening efficiency decreases with increased mixing, although the effect is far more pronounced over land (r=0.54; slope=4.2%/day). Here, the summertime mixing rates increase as convection deepens [as inferred from correlating TES cloud top pressure measurements and $1/k$ (r=0.39, n=1584)], and M significantly decreases with decreasing cloud top pressure (r=0.51). Since the mean of tropical cloud top pressure

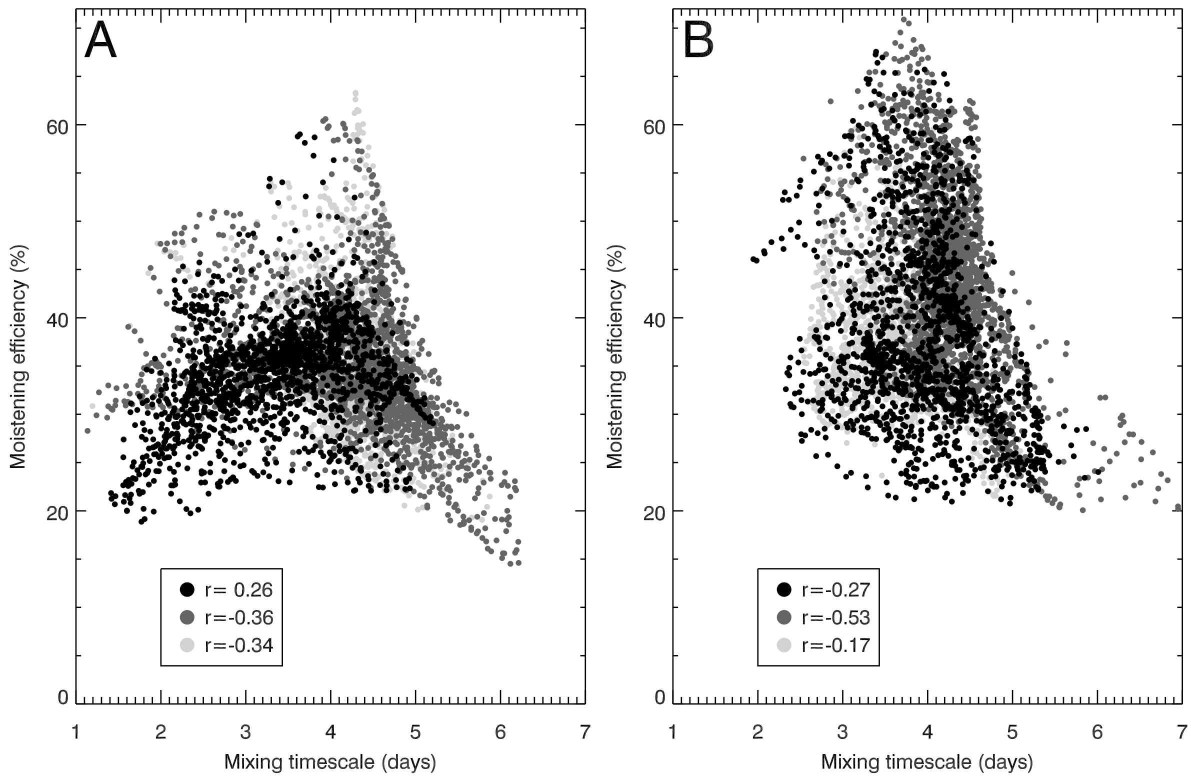

Figure 4.11: Scatterplots of moistening efficiency versus mixing timescale values for the tropics (0º-15ºN/S, black), subtropics (15º-32.5ºN/S, dark grey), and midlatitudes (32.5º-40º, light grey) during a) summer and b) winter. Correlations in legend are statistically significant at the 99% confidence level.

measurements associated with the lowest (highest) 25% of *M* values is 466 (507) hPa, the average values of *M* in the 500-825 hPa layer may be marginally sensitive to the level of convective detrainment. Additionally, during tropical summer, *M* decreases as the large-scale vapor transport increases (r=-0.72), in agreement with past results over monsoonal regions (e.g., *Trenberth et al.* [1999]). By using isotopic information in the following section, however, the decrease in *M* over tropical land is shown to be partially controlled by intense local mixing, which leads to a drier and more depleted local moisture source than previously recognized.

4.5.3 Source Moisture Mechanisms

There are a variety of moistening processes that can contribute to the regional source waters (q_s): simple mixing by shallow convection or turbulence, reversible adiabatic (cloud) processes, convective detrainment, and re-moistening by rainfall evaporation. The dominant moistening processes can be examined by comparing the derived estimates of δD_s and q_s with predictions based on mixing and distillation. Labeled mixing lines Figure 4.12 are initialized from a land source (i.e. transpiration) or from a source typical of marine boundary layer conditions. The transpiration mixing line, initialized from Global Network of Isotopes in Precipitation (GNIP) δD precipitation values in each region, assumes rainfall is transpired unfractionated [*Flanagan et al.*, 1991; *Still et al.*, 2009] and then mixed with much drier air, and therefore represents an upper limit to the δD value of moisture influenced by transpiration. The marine mixing line also assumes direct mixing, and is initialized with oceanic boundary layer air, assuming a relative humidity of 80% and SST of 27ºC.

The amount of isotopic fractionation that occurs during condensation is recorded in the residual water vapor. Three condensation processes (Figures 4.12; labeled) are represented: moist adiabatic [condensed water is not removed from the system and thus continuously exchanges with the vapor (i.e. a reversible process and less fractionation)], Rayleigh distillation [condensed water is instantly removed from the system (i.e. non-reversible)], and 'super-Rayleigh' distillation (additional fractionation during condensation and removal of condensate) [*Noone*, 2010]. 'Super-Rayleigh' distillation can represent any in-cloud processes that lead to higher effective isotopic fractionation rates than those expected from vapor pressures differences of HDO and H_2O [*Rozanski et al.*, 1993], including the effects of reintroduced residual vapor resulting from post-condensational exchange [*Worden et al.*, 2007; *Risi et al.*, 2008a; *Wright et al.*, 2009b]. The rates of different moistening processes emerge by partitioning into bins based on the source data by mixing timescales (*1/k*): Q1 is the quartile of data with the lowest 25% of regional mixing times, Q4 indicates the quartile with the 25% highest, and Q2+Q3 is the middle 50% of the distribution. While this partitioning is sensitive to geographical variations in mean climate, use of this partitioning over the land and ocean over specific latitudinal bands during specific seasons ensures that the analysis is also sensitive to the variations of moistening processes in regions with similar climate.

During tropical summer, the average source water (Figure 4.12a) is more humid and less depleted over land (q_s=14.6 g/kg; δD_s=-133‰) than ocean (Figure 4.12b: 13.9 g/kg; -140‰), with stronger mixing over land ($1/k$=3.1 days) than ocean (3.8 days). This is consistent with increased terrestrial humidity and convection during the monsoon. All mixing bin contours overlap the remoistening line, indicating that source waters formed from post-condensational

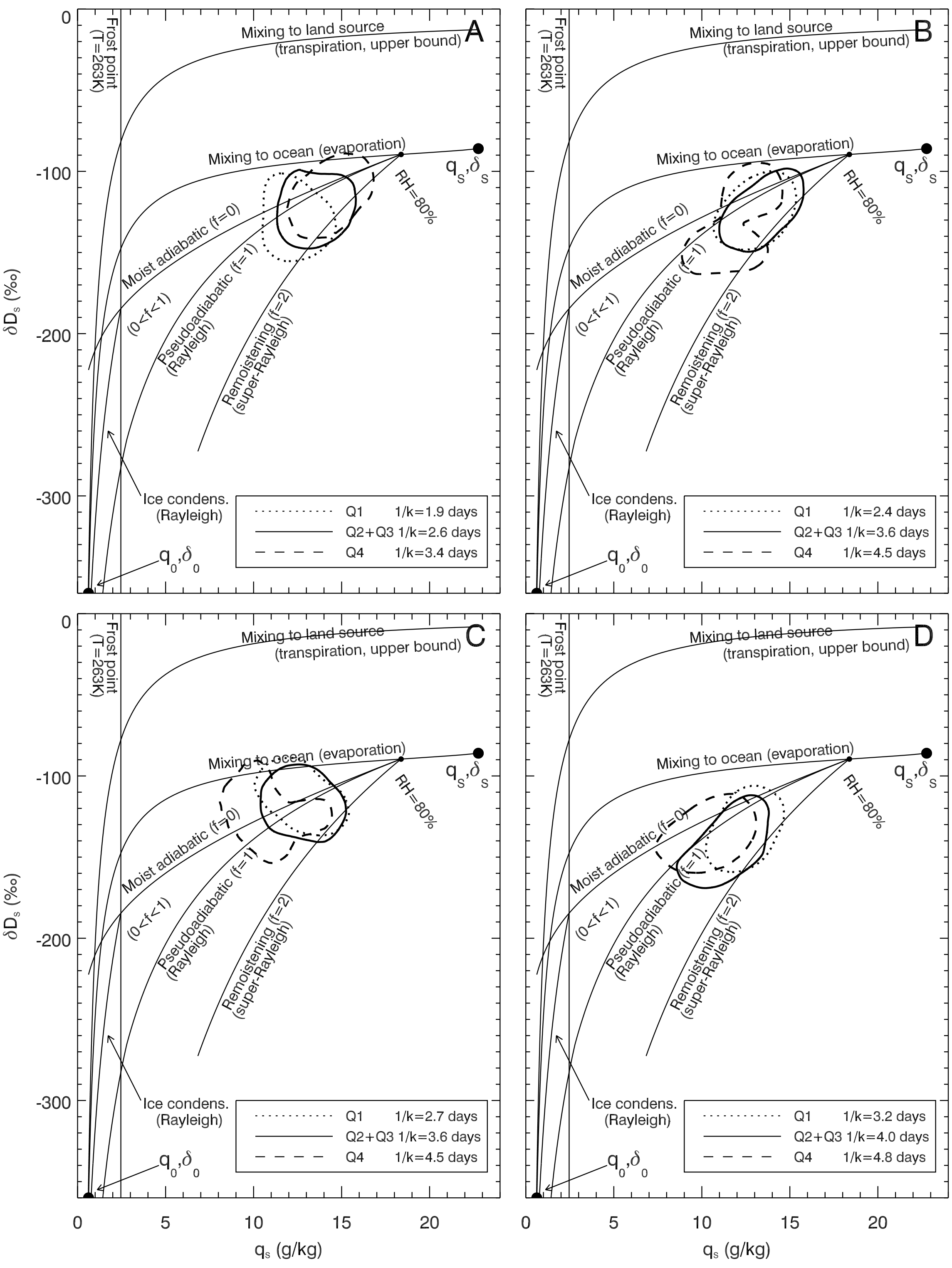

Figure 4.12: δD_s versus q_s over tropical (0°-15°N or S) regions: summertime land (a) and ocean (b); and wintertime land (c) and ocean (d). Labeled lines indicate mixing and distillation processes (see Noone [2010]) assuming the dominant global source of water is evaporation from the ocean (RH=80%, SST=27ºC). Contours surround bins (1g/kg by 10‰) where 2% or more of the data within each 1/*k* partition (Q1, Q2+Q3, and Q4) are found.

exchange are important during tropical summer. Over land, the source waters become more depleted, and less humid, as mixing rates increase [$r(1/k, \delta D_s)$=0.42; $r(1/k, Q_s)$=0.59; n=349)].

The regional relationships between mixing rate and source moisture humidity (Figure 4.13) illustrate that this tendency is specific to tropical regions with very strong mixing ($1/k < 3$ days ; Figure 4.13a). This mechanism is consistent with previous work by Lawrence et al. [2004], which found anomalously depleted oceanic boundary layer moisture near organized convective storms. Thus, as convective mixing increases, the local source moisture is increasingly influenced by drier, and more depleted, moisture from the storms (e.g., Risi et al. [2008a]), leading to decreased moistening efficiency in the 500-825 hPa layer (Figure 4.11a). The moistening over the summertime tropical ocean (Figure 4.12b) is similar to that over land (e.g., moist convection and post-condensational exchange) with some exceptions: the least humid source waters are associated with the slowest mixing (Q4); the source isotopic composition becomes slightly more enriched as mixing increases; and, moistening efficiency is fairly consistent between partitions (Q1, 32%; Q4 34%). Thus, the source waters do not generally become drier and more depleted as mixing intensifies, as is the case over land. The depleting and dehydrating effect during intense tropical mixing is found to have a critical mixing timescale, where the positive correlation between mixing timescale and moistening efficiency becomes insignificant in paired data beyond $1/k$=2.3 days, and in fact significantly negative beyond 2.8 days (see shape in Figure 4.11a). Paired data below $1/k$=2.3 days yields a strong positive correlation (r=0.56, n=192) and a 13.6% increase in M per day increase in $1/k$. Thus, it is only in very strong mixing conditions, which are found primarily over summertime tropical land, that source waters become drier, more depleted, and less efficient in locally hydrating the 500-825 hPa layer.

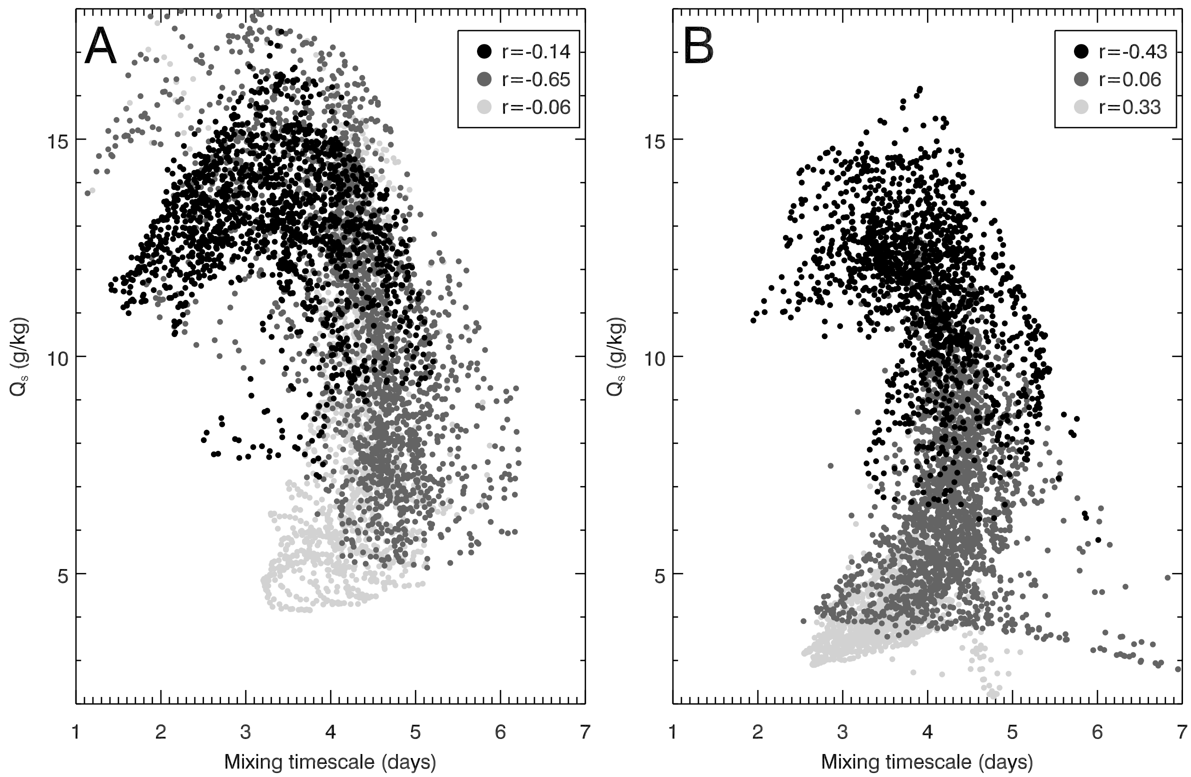

Figure 4.13: Scatterplot of source moisture versus mixing timescale for the tropics (0º-15ºN/S, black), subtropics (0º-15º-32.5ºN/S, dark grey), and midlatitudes (32.5º-40º, light grey) during a) summer and b) winter. Except for the midlatitude region during summer (a), regional correlations in legend are statistically significant at the 99% confidence level.

Over tropical land during winter (Figure 4.12c), slow mixing often occurs with moisture formed from cloud evaporation, as shown by the Q4 data encompassing the reversible moist adiabatic exchange line. More than 50% of the total moistening (*G*) occurs via this process, with the remaining moistening occurring through precipitating clouds. In contrast, ~90% of moistening (*G*) over ocean (Figure 4.12d) occurs through precipitating storms, with more areas showing post-condensational exchange. This situation is reflective of the winter monsoon, where the high heat capacity of the ocean waters allows residual warmth to drive convection. The winter monsoon shows that storms with high isotopic 'rainout' and strong mixing are the most efficient at hydrating the 500-825 hPa layer [$r(M, 1/k)$=-0.30; $r(M, \delta D_s)$=-0.59; n=1235], in contrast to the summer monsoon over land. However, as during summer, this effect is partially masked by moisture advection, since moistening efficiency tends to decrease as the large-scale moisture transport (i.e., the upstream parcel humidity) increases.

Moistening processes vary substantially with mixing rates in the summertime subtropics (Figures 4.14a-b). Strong mixing (Q1 bin) is associated with source moisture derived almost entirely from an air mass with a history of post-condensational exchange, and accounts for 36% (37%) of the summertime moistening over land (ocean). Much of the source moisture with this isotopic signature is found near the (rainy) Asian and North American monsoon regions. Over subtropical land, 50% of *G* is derived from source moisture processed through shallow convection (i.e. little fractionation of marine boundary layer moisture; Q2+Q3 bin), while over the ocean the effects of shallow convection are limited. Moistening by cloud evaporation (Q4) is more prominent over land, and provides 15% of total *G* over land compared to 9% over ocean. In agreement with the results from Couhert et al. [2010], this study finds evidence for substantial gains of moisture into the summertime subtropical parcels over land via convective processes, and additionally resolves that half of that moistening over land occurs through boundary layer clouds. In addition, the quantification of post-condensational exchange to local moistening extends previous work that found rainfall re-evaporation to be a significant source of atmospheric moisture near convective clouds [*Worden et al.*, 2007].

Local moistening over land has a stronger influence on total subtropical moistening (land + ocean) during summer (36%) than winter (27%). There is little difference in mixing strength over ocean and land during the winter (Figures 4.14c and 4.14d), and most of the data suggest cloud evaporation (i.e., a reversible moist adiabatic process) is the dominant moistening process. Even with relatively depleted and dry source moisture when compared with other regions, the moistening efficiency (M) values in this region are high (42% over land; 45% over ocean) since the overlying atmosphere is extremely dry. Fractional increases in water vapor amounts (as in M) in this region substantially impact the global water vapor feedback [*Pierrehumbert*, 1999], thus local moistening from cloud evaporation over the wintertime subtropics is of importance to the global energy balance.

4.5.4 Dehydration Mechanisms

At equilibrium, differences in the vapor pressures of HDO and H_2O results in a higher relative concentration of the heavy isotopes (HDO) in the condensed phase [*Dansgaard*, 1964; *Craig and Gordon*, 1965]. Following the work of Noone et al. [2010], the calculation of isotopic fractionation during equilibrium conditions (α_e) is found here by using the vapor pressure differences of HDO and H_2O found at the average dewpoint temperature for each individual trajectory. The difference between net isotopic fractionation (α) found from the mass budget

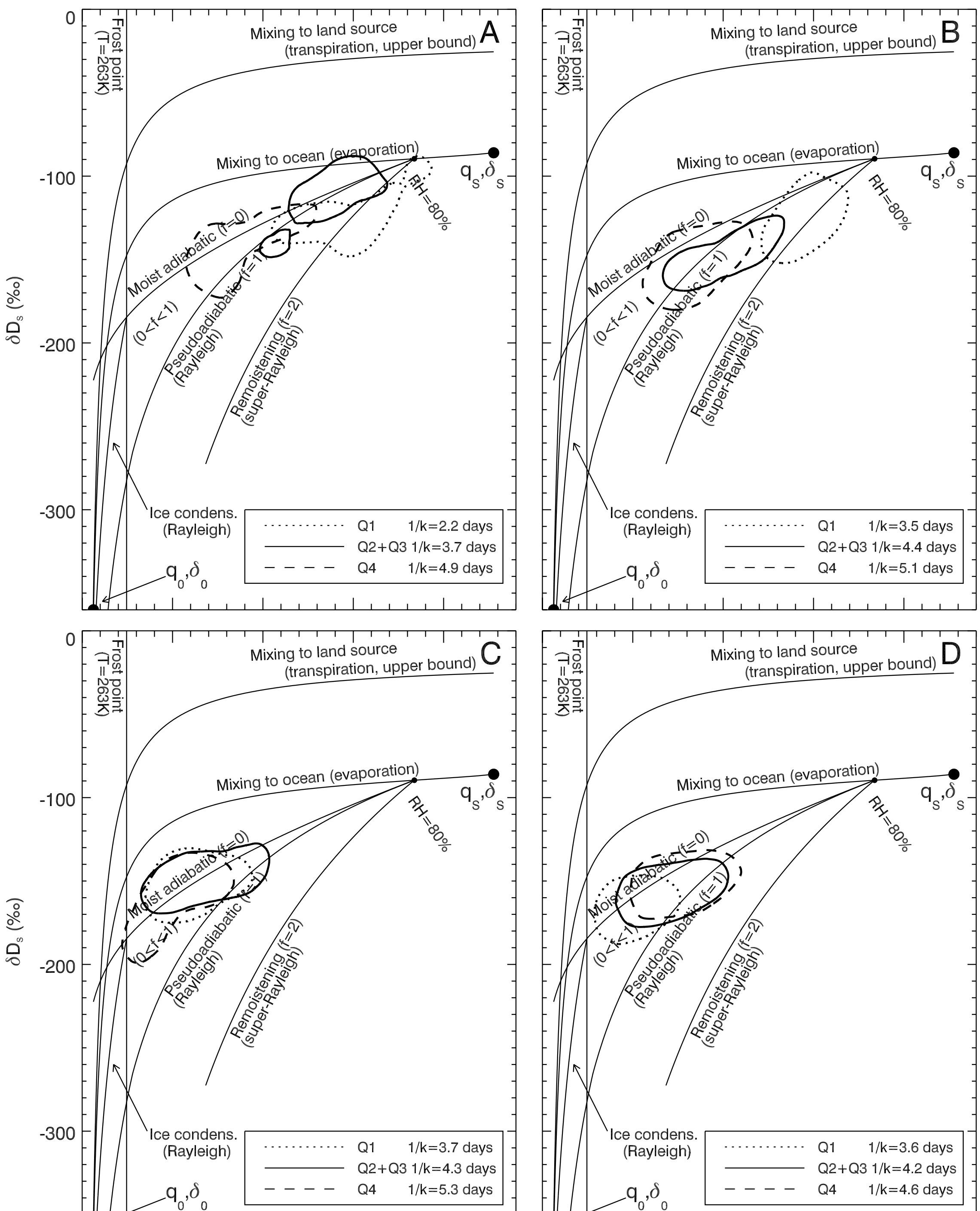

Figure 4.14: As in Figure 4.12, but for the subtropical (15°-32.5°N or S) regions.

model and α_e (Figure 4.16) gives a measure of the reversibility of cloud processes (i.e., cloud dissipation) and post-condensational exchange [*Noone*, 2010].

The spatial distribution of α-α_e (Figure 4.15) shows higher effective fractionation (α-α_e positive, dark shading) over monsoonal regions (e.g., the Amazon Basin and Northern Australia during DJF; the Asian Monsoon, Central African, and Central American regions during JJA), which is in agreement with the spatial distribution of excess depletion in residual vapor (i.e., beyond Rayleigh expectations) found from past analyses of TES observations [*Brown et al.*, 2008] and of models that utilize post-condensational effect schemes [*Wright et al.*, 2009b; *Field et al.*, 2010]. Worden et al. [2007] used enhanced fractionation found in TES data to quantify rainfall evaporation as a one-way distillation process, which is valid for large drops falling through very dry air. However, this study finds enhanced fractionation primarily occurring over moist regions, thus quantification of post-condensational exchange below the cloud base would require additional information of the drop size spectrum and isotopic composition of the sub-cloud air [*Bolin*, 1958], which is beyond the scope of this study. As such, the spatial relationships between strong effective fractionation rates and local moistening processes are highlighted here. During the hemispheric summers and from 40ºN-40ºS, α-α_e significantly increases with increased mixing [r(α-α_e, $1/k$)=-0.37; n=4752] and significantly decreases with increasing moistening efficiency [r(α-α_e, M)=-0.42; n=4752]. Considering just the tropical regions during summer, r(α-α_e, $1/k$)=-0.34 and r(α-α_e, M)=-0.59 (n=1872). This illustrates that anomalous depletion reaches its maximum over highly convective regions where moistening efficiency is low. These relationships suggest that reduced localized moistening and strong convective mixing are requirements for non-Rayleigh isotopic depletion of water vapor. This is in agreement with the processes proposed by Risi et al. [2008a] to explain strong isotopic depletion during

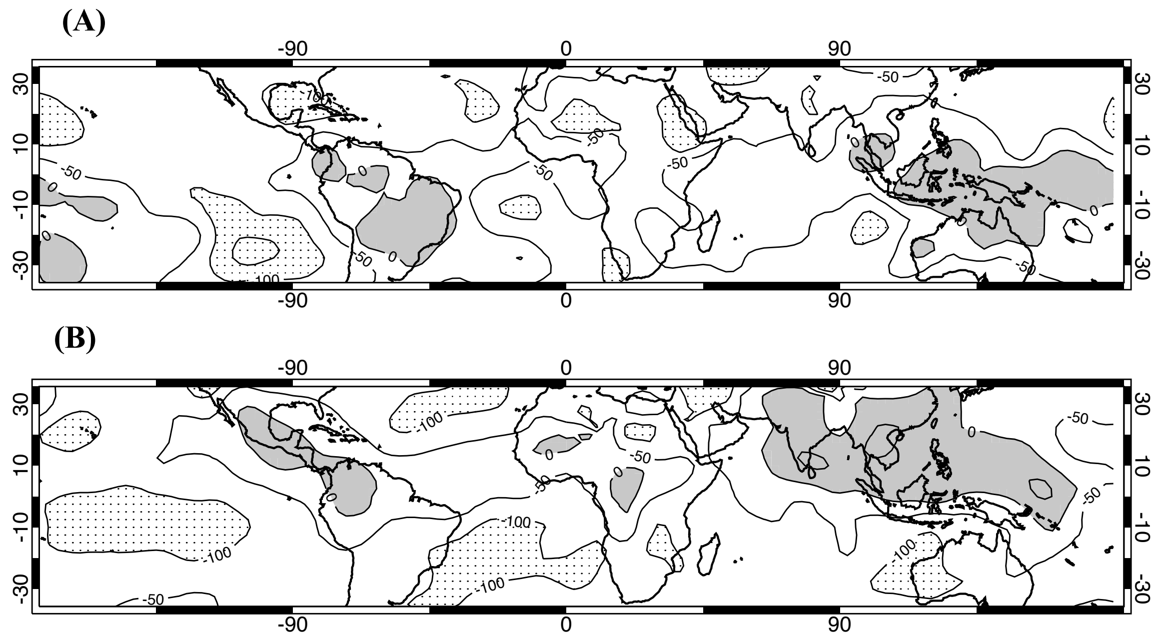

Figure 4.15: The difference between effective and equilibrium fractionation factors, (α-α_e, ‰) for (a) DJF and (b) JJA. Dark shading indicates regions where α-α_e is greater than zero, while stippling indicates regions where α-α_e is less than -100‰. Contour interval is 50‰.

convection, which required a substantial (recycling) connection between unsaturated downdrafts and the sub-cloud layer and thus a reduced local source of moisture.

Reversible moist processes, where condensate is not removed from the system but instead remains in isotopic equilibrium with the vapor, reduce effective fractionation rates [*Merlivat and Jouzel*, 1979]. The above correlation analysis revealed that α-α_e is lowest in regions with weak mixing but high local moistening efficiency. Figures 4.12 and 4.14 illustrated that reversible processes are commonly a moisture source during weak mixing, and we speculate that this is the result of the dissipation of low-level boundary layer clouds [*Lee et al.*, 2010].

Utilizing a similar decomposition as in work by Noone [2010], the relationship between the effective and equilibrium fractionation factors can provide an approximation of precipitation efficiency (precipitation divided by cloud water). By assuming the cloud liquid is in equilibrium with the surrounding vapor, and that the isotopic composition of precipitation removed from the system is identical to that of the cloud water, the effective fractionation is found as

$$\alpha = \frac{\alpha_e}{\alpha_e(1-f)-f} \qquad \text{(E4.15)}$$

where f is the precipitation efficiency. Solving for the precipitation efficiency,

$$f = \frac{\alpha_e(\alpha-1)}{\alpha(\alpha_e-1)}. \qquad \text{(E4.16)}$$

Indeed Equation 4.16 is the relationship used for the distillation lines in Figure 4.12 and 4.14, and is used here to estimate precipitation efficiency from the effective and equilibrium fractionation factors. However, there are limitations to this application. The derivation of Equation 4.16 [*Noone*, 2010] results from considering the loss of 'total' water (vapor + liquid) during a dehydration process, while the α values describe the fractionation between phases during that process. As the amount of liquid at the upstream trajectory point is not known here, the estimation of f is only used to show the sensitivity of α-α_e to changes in precipitation efficiency calculated by other means. Given this, the limits of Equation 4.16 show that when α=α_e then f=1 as in Rayleigh process and when α=1 then f=0 as in a reversible moist adiabatic process. Noted above, a positive α-α_e value is likely indicative of post-condensational exchange, which is a process that requires additional information to quantify appropriately. Positive α-α_e values suggest a seemingly unphysical result from (E4.16). In practice, these are associated with a limitation in the simple parcel model and suggests an additional moisture source, for example, vapor resulting from evaporation of ice or more complex cloud-scale exchanges. As such these regions are masked in the following comparison.

Making use of TRMM monthly mean precipitation data (version 3B43, [*Huffman et al.*, 1995]), a mass weighted precipitation rate (P_{TRMM}) is found using the levels in the TES retrieval (500-825 hPa). Precipitation efficiency is then calculated simply as P_{TRMM}/L, and compared to the proxy deduced from Equation 4.16 (Figure 4.16). While in Figure 4.16, the proxy value of f (solid) is globally lower than that found using the TRMM data (dashed), the meridional pattern is reproduced reasonably and the agreement poleward of 25º during winter (black lines) is good. These regions are where source moisture is greatly influenced by evaporation of shallow and stratiform cloud (Figure 4.14c and 4.14d). This result confirms that the evaporation of boundary layer clouds has a strong local effect on subtropical moistening and moistening efficiency. While the comparison shown in Figure 4.16 has limitations, including the use of monthly mean TRMM

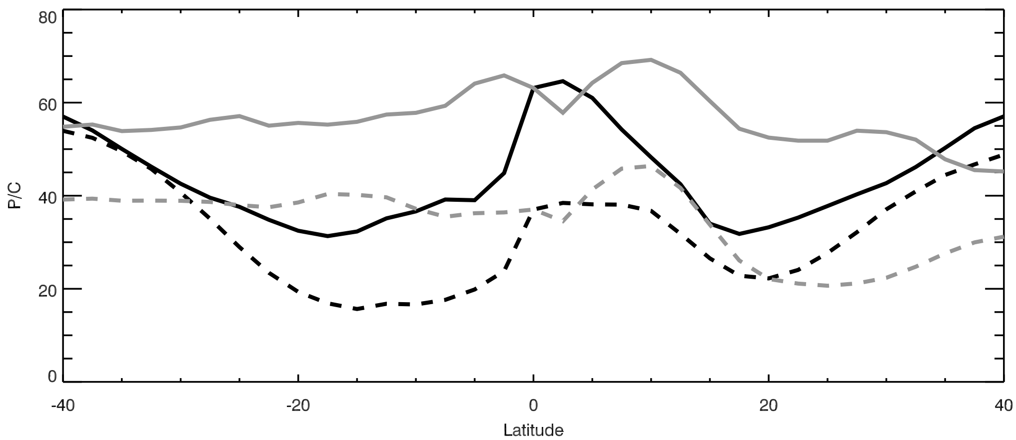

Figure 4.16: Zonal mean precipitation efficiency found as TRMM precipitation divided by model condensation (P_{TRMM}/L, dashed) and as a proxy using effective and equilibrium fractionation [as in (E4.16), solid] for summer (grey) and winter (black).

precipitation instead of collocated precipitation data, the spatial agreement found here using a very simple Lagrangrian model provides confidence that more advanced models can utilize isotopic fractionation to quantify precipitation effectively.

4.6 Conclusions

Moistening characteristics of the 500-825 hPa layer emerged in this analysis by identifying the isotopic composition and humidity of moisture which mixes into passing air parcels, the formation processes which led to these moisture sources, the timescales over which this mixing occurs, and the resultant fractional increases in large-scale humidity values associated with local moisture sources. Local moisture sources were found to (a) contribute substantially to the large-scale moisture field; (b) to be associated primarily with vapor detrained from precipitating cloud systems in the moist tropical regions, with vapor resulting from post-condensational exchange and reversible processes in the summertime subtropics, and with vapor associated with reversible processes over dry tropical land and over the wintertime subtropics; and (c) to have the largest impact on fractional moisture gains (i.e., moistening efficiency) in the wintertime (dry) subtropical regions (15º-25ºN/S).

Trenberth [1999] found that in the tropics, strong large-scale moisture transport limits the effects of local sources on moistening efficiency values, which is confirmed here. However, during summer over tropical land (i.e., monsoonal) regions, isotopic analysis revealed that as mixing rates increase, the isotopic composition of the source moisture becomes more depleted. In these areas of heavy rainfall, strong isotopic fractionation and dehydration during intense (moist) convective storms decrease the humidity of the source moisture, which subsequently limits moistening efficiency. This mechanism is similar to that modeled by *Risi et al.* [2008a], where moisture associated with highly depleted and unsaturated downdrafts were found to be re-entrained into convective storms, leading to anomalous depletion of subsequent rainfall (i.e., contribute to an "amount effect") that forms from the increasingly depleted moisture source. Evidence for this mechanism in TES data was recently found near convective clouds in the western Pacific Ocean [*Lee et al.*, 2010]. Future work with TES data will thus have the potential to enhance our understanding of the amount effect, by using the isotopic composition of water vapor to evaluate the atmospheric dynamics and cloud microphysics that must occur to produce very depleted rainfall in monsoonal regions.

Results show post-condensational exchange as an important component (>35%) to local moistening over the summertime subtropics, which raises the total local fraction of water in the 500-825 hPa layer by approximately 5% over a one day timeframe. This moistening process is also active during tropical summer, but has limited effects on the large-scale humidity. That post-condensational exchange is important for atmospheric hydrology and is identifiable using isotopic methods aligns with recent work [*Worden et al.*, 2007; *Brown et al.*, 2008; *Wright et al.*, 2009b; *Field et al.*, 2010]. This process is found to be associated with increased mixing rates in the summertime subtropics which, in speculation, may result from increasing rainfall evaporation affecting local buoyancy/stability and thus acting to increase local turbulence and exchange. There remains a clear need to further decipher the different characteristics of post-condensational exchange, and the effects on lower tropospheric humidity, in dry versus moist regions using datasets supplemented with isotopic information. Such work will be useful for improving parameterizations in current climate models, which currently produce drier lower tropospheric air than observed during convective storms [*Mapes et al.*, 2009].

Convective processes, and atmospheric mixing, are important for earth's hydrologic cycle, yet resolving the regional characteristics of these processes is difficult using the basic state that water vapor provides. We have shown that isotopologues of water vapor, as seen from satellites, help to constrain these characteristics through their ability to record past condensation and evaporation events. In addition, we have shown that the effective fractionation calculated during dehydration, when compared to that expected in a Rayleigh process (i.e., equilibrium fractionation), is sensitive to the precipitation efficiency and hence the reversibility of moist processes. Using these properties and simple modeling, this study has shown a large range of processes act to form moisture that ultimately mixes into the large scale flow at different regional rates. While the tropical regions have active convection, strong mixing, and large gross moistening values, the local effects on the large-scale humidity are modest. In contrast to the tropics, vapor associated with reversible processes (i.e. cloud "burn-off") dominates local moistening in the dry subtropics, and the resultant local gross moistening, while modest in magnitude compared to that in the tropics, contributes significantly to the (low) large-scale humidity. Moistening efficiency (M) in this region is currently found to be twice as sensitive to mixing rates as other areas, and the variability of mixing rates is captured in the intraseasonal variance of regional δD values. Thus, future satellite measurements of isotopic composition in these areas are particularly important to identify changes in the regional hydrology as they occur, and are climatically important since changes will affect the water vapor feedback and hence radiation budget.

5 Chapter 5

Conclusions

Tropospheric humidity has a number of interesting and important controls (Figure 1.3), which are shown in this study to vary in their strength and relative importance between regions and seasons. The results from Chapter 2 show transient eddies are important for the relative humidity budget by exchanging heat and moisture in all regions. Transient eddies have the strongest effect on relative humidity in the midlatitudes, which are the regions where the average meteorological conditions make relative humidity most sensitive to perturbations in temperature and moisture. Both hemispheres show an increasing effect on relative humidity from transient eddy moisture convergence, as well a decreasing effect on relative humidity from increasing condensation over time in the midlatitudes. While this indicates a strengthening of the hydrologic cycle, the opposing effects of increased condensation and moisture convergence have maintained a relatively constant regional relative humidity from 1979-2004. Similarly, in the NH subtropics, increased relative humidity effects from subsidence (shown in Figure 1.3 as large, downward arrow in center) have opposed increased relative humidity effects from heat divergence over the 26 year period. While the relative humidity effects from subsidence at 500 hPa are modulated by ENSO, the long-term trend is more likely related to a fundamental shift in the atmospheric circulation. This is a result that would be missed by evaluating relative humidity itself, since there are no significant trends in mean relative humidity in these regions due to the compensatory nature of the trends in the influential processes.

An important result from Chapter 2 is that deviations in relative humidity are more influenced by changes in moisture than those in temperature over intraseasonal timescales. In addition, Sherwood et al. [2006] noted that the effects of unresolved small-scale moistening processes must be important for maintaining low-level humidity. Thus, Chapters 3 and 4 shift focus to characterize moistening and dehydration processes that underlie the humidity budget, using the additional information provided by isotopic ratios in water vapor as the primary tool.

Given the expectations from past isotopic modeling and observational work, Chapter 3 evaluates the isotopic budget over seasonally convective monsoonal regions to maximize the seasonal and intraseasonal variations in isotopic signals and substantiate the primary atmospheric processes that control them. Correlation analysis revealed that mixing with boundary layer air, enhanced isotopic fractionation during precipitation, and subsiding air parcels contribute to intraseasonal and interseasonal isotopic variability, with the relative strength of each process varying with geographic location. For example, non-Rayleigh isotopic depletion during the Amazon and Asian monsoon regional wet seasons, which is related to post-condensational exchange, does not dictate the interseasonal δD signal in both regions. Instead, increased low-level atmospheric stability and dry season subsidence over the Asian monsoon region introduces equally low δD values as those caused by heavy monsoonal rains, while active convection during the Amazonian dry season ventilates less depleted boundary layer air and leads to a strong negative DJF-JJA δD signal. The northern Australian monsoon shows while strong intraseasonal variance in δD is due to variations in the strength of monsoonal condensation and boundary layer ventilation events, dry season subsidence introduces very isotopically depleted air and leads to a strong positive DJF-JJA δD signal. These regional analyses use several external datasets to corroborate that interseasonal and intraseasonal variations in moist processes are captured in the distribution of δD values found from TES.

The correlation analysis in Chapter 3 revealed that local controls explain only 8-30% of total regional variance in observed δD, and found that the isotopes are primarily indicators of moist processes that occur upstream of the observations. As such, an evaluation of the changes in the isotopic distributions on approach to monsoonal regions was performed, with the conclusions validated through comparison with moist process histories calculated from NCEP-NCAR Reanalysis. The non-Rayleigh nature of the changes in the isotopic distributions made clear that turbulent transport of boundary layer moisture, subsidence, and post-condensational exchange must be accounted for to explain the observations. While explanation of the isotopic distributions was a necessary first step towards understanding the TES observations, the results of Chapter 3 ultimately provided confidence that information in the distribution of HDO/H_2O may be explicitly extracted to expose moist processes that are not captured in Rayleigh-like models.

To accomplish this task, the analysis described in Chapter 4 utilizes a Lagrangrian mass budget model, constrained by both specific humidity and HDO/H_2O values from TES, to quantify atmospheric moistening, mixing, and dehydration rates. The isotopic information found from the mass budget is used in conjunction with a theoretical framework (Figure 1.4) to expose the regional processes which form the dominant local moisture sources as well as the conditions during condensation. Evaluation of the relationship between the dehydration and source processes with local mixing rates, and the resultant fractional increases in the large scale humidity field, enabled a unique characterization of the strength and nature of atmospheric moistening and dehydration.

The results of Chapter 4 showed regional variability in the impact of local moistening on the large-scale moisture field. Notably, these local moistening effects are not resolved in advection-condensation models, which have been used extensively in explaining the water vapor distribution. Local moistening was found to be associated primarily with vapor processed by precipitating cloud systems in the moist tropical regions, with vapor resulting from post-condensational exchange and reversible processes in the summertime subtropics, and with vapor associated with reversible processes over dry tropical land. The largest impact of local moistening on fractional moisture gains (i.e., moistening efficiency) were found in the wintertime (dry) subtropical regions, where the dominant source is vapor processed through non-precipitating boundary layer clouds. While some vapor from direct ventilation of the boundary layer moistens the 500-825 hPa layer over the wintertime tropical and summertime subtropical regions, the vast majority of local moistening in all regions is provided by vapor with a history of condensation.

Dehydration mechanisms are found from comparisons of effective fractionation and temperature-dependent, equilibrium fractionation rates, and the regional variance in the conditions during condensation emerged clearly by using these data-derived fractionation rate differences in conjunction with a theoretical framework put forth by Noone [2010] (see Figure 1.4). The results indicate post-condensational exchange is an important part of the hydrology over monsoonal regions, which agrees with recent modeling [*Risi et al.*, 2008a; *Wright et al.*, 2009b; *Field et al.*, 2010] and observational [*Worden et al.*, 2007] work. The analysis presented strong evidence for a link between isotopic depletion of the source moisture, intense mixing, and non-Rayleigh (high) fractionation rates. This is in agreement with recent modeling work [*Risi et al.*, 2008a] where highly depleted residual vapor (following condensation) recycles during strong convection via unsaturated downdrafts, forming an increasingly depleted moisture source for subsequent rains.

The Lagrangian framework allows for a measure of reversibility in cloud systems when effective isotopic fractionation rates are lower than those expected during equilibrium conditions. From the differences in effective versus equilibrium fractionation, a proxy for precipitation efficiency is formed and compared to the ratio of mass-weighted TRMM precipitation rates over the 500-825 hPa layer to the calculated condensation (*L*). While disagreements in the magnitude of the results exist, the meridional patterns of the proxy and ratio P_{TRMM}/L are similar, which provides confidence that the HDO/H_2O values are sensitive to precipitation efficiency. Precipitation efficiency maxima are found in the ITCZ and wintertime midlatitudes (~45-65%; 40º N/S), with minima found in the wintertime subtropics (~20-30%; 20º N/S). This pattern agrees with work that found precipitation efficiency maxima in warm, convective regions [*Li et al.*, 2002]. Good agreement between the proxy and P_{TRMM}/L are found poleward of 25º during winter (low precipitation efficiency), where the source moisture analysis reinforced that vapor associated with cloud dissipation/evaporation provides local moistening. These robust results are important, as this is a climatically important region since fractional variations in water vapor are large and have strong effects on the water vapor feedback.

This study parsed large-scale humidity budgets (i.e., the relative humidity budget from MERRA or the moisture budget from TES) into individual components, and extracted important information about the nature and strength of humidity processes that is unattainable by considering just the mean state. In addition, the insights in atmospheric moistening gained here through isotopic analysis break ground for more sophisticated modeling approaches using satellite isotopic data, which may further advance our understanding of global and regional scale humidity. While there are clear limitations to the extent of analysis currently possible with single layer HDO/H_2O measurements, future increases in vertically resolved measurements would allow for a much more comprehensive view of the characteristics of atmospheric hydrology, and provide a much needed check on the treatment of water vapor in modern General Circulation Models.

Bibliography

Angert, A., J. E. Lee, and D. Yakir (2008), Seasonal variations in the isotopic composition of near-surface water vapour in the eastern Mediterranean, *Tellus B,* **60**(4), 674-684.

Araguas-Araguas, L., K. Froehlich, and K. Rozanski (1998), Stable isotope composition of precipitation over southeast Asia, *J. Geophys. Res.,* **103**, 28,721-28,742.

Araguas-Araguas, L., K. Froehlich, and K. Rozanski (2000), Deuterium and oxygen-18 isotope composition of precipitation and atmospheric moisture, *Hydrol. Process.,* **14**, 1341-1355.

Back, L. E., and C. S. Bretherton (2006), Geographic variability in the export of moist static energy and vertical motion profiles in the tropical Pacific, *Geophys. Res. Lett.*, **33**, L17810.

Bellucci, A., S. Gualdi, and A. Navarra (2010), The Double-ITCZ Syndrome in Coupled General Circulation Models: The Role of Large-Scale Vertical Circulation Regimes, *J. Clim.,* **23**(5), 1127-1145.

Bengtsson, L., P. Arkin, P. Berrisford, P. Bougeault, C. K. Folland, C. Gordon, K. Haines, K. I. Hodges, P. Jones, P. Kallberg, N. Rayner, A. J. Simmons, D. Stammer, P. W. Thorne, S. Uppala, and R. S. Vose (2007), The need for a dynamical climate reanalysis, *Bull. Am. Meteorol. Soc.,* **88**(4), 495-501.

Betts, A. K. (1990), Greenhouse Warming and the Tropical Water-Budget, *Bull. Am. Meteorol. Soc.,* **71**(10).

Bloom, S. C., L. L. Takacs, A. M. DaSilva, and D. Ledvina (1996), Data assimilation using incremental analysis updates, *Mon. Weather Rev.,* **124**(6), 1256-1271.

Blunier, T., and J. Schwander, J. Chappellaz, F. Parrenin, J.M. Barnola (2004), What was the surface temperature in central Antarctica during the last glacial maximum?, *Earth Planet. Sc. Lett.*, **218**(3), 379-388.

Bolin, B. (1958), On the use of tritium as a tracer for water in nature, paper presented at Proceedings of 2nd International Conference on Peaceful Use of Atomic Energy, 336-343.

Bony, S., and K. A. Emanuel (2005), On the role of moist processes in tropical intraseasonal variability: Cloud-radiation and moisture-convection feedbacks, *J. Atmos. Sci.,* **62**(8), 2770-2789.

Bony, S., C. Risi, and F. Vimeux (2008), Influence of convective processes on the isotopic composition (delta O-18 and delta D) of precipitation and water vapor in the tropics: 1. Radiative-convective equilibrium and Tropical Ocean-Global Atmosphere-Coupled

Ocean-Atmosphere Response Experiment (TOGA-COARE) simulations, *J. Geophys. Res.,* **113**(D19).

Boyle, J. S. (2000), Comparison of Variability of the Monthly Mean Temperature of the ECMWF and NCEP Reanalyses and CCM3 and CSM Simulations, Technical Report UCRL-ID-137580, Lawrence Livermore National Lab, Livermore, CA.

Brent, R. P. (1972), *Algorithms for minimization without derivatives*, xii, 195 p., Prentice-Hall, Englewood Cliffs, N.J.

Brown, D., J. Worden, and D. Noone (2008), Comparison of atmospheric hydrology over convective continental regions using water vapor isotope measurements from space, *J. Geophys. Res.,* **113**(15).

Cappa, C. D., M. B. Hendricks, D. J. DePaolo, and R. C. Cohen (2003), Isotopic fractionation of water during evaporation, *J. Geophys. Res.,* **108**(D16).

Cau, P., J. Methven, and B.J. Hoskins (2007), Origins of dry air in the Tropics and Subtropics. *J. Clim.,* **15**, 2745-2759.

Chen, G., and H. Lin (2005), Impact of El Nino/La Nina on the seasonality of oceanic water vapor: A proposed scheme for determining the ITCZ, *Mon. Weath. Rev.,* **133**(10), 2940-2946.

Clough, S. A., M. W. Shephard, J. Worden, P. D. Brown, H. M. Worden, M. Luo, C. D. Rodgers, C. P. Rinsland, A. Goldman, L. Brown, S. S. Kulawik, A. Eldering, M. Lampel, G. Osterman, R. Beer, K. Bowman, K. E. Cady-Pereira, and E. J. Mlawer (2006), Forward model and Jacobians for Tropospheric Emission Spectrometer retrievals, *IEEE Trans. Geosci. Remote Sens.,* **44**(5), 1308-1323.

Colman, R.A., (2003), A comparison of climate feedbacks in general circulation models. *Clim. Dyn.*, **20**, 865–873.

Couhert, A., T. Schneider, J. L. Li, D. E. Waliser, and A. M. Tompkins (2010), The Maintenance of the Relative Humidity of the Subtropical Free Troposphere, *J. Clim.,* **23**(2), 390-403.

Craig, H., and L. I. Gordon (1965), Deuterium and oxygen 18 variations in the ocean and the marine atmosphere, in *Stable Isotopes in Oceanographic Studies and Paleotemperatures*, edited by E. Tongiorgi, pp. 9-130, Lab. di Geol. Nucl., Pisa, Italy.

Dai, A. (2006), Recent climatology, variability, and trends in global surface humidity, *J. Clim.,* **19**(15), 3589-3606.

Dansgaard, W. (1964), Stable Isotopes in Precipitation, *Tellus,* **16**(4), 436-468.

Davenport, S. (2009), Migration of the ITCZ, *Weather,* **64**(9), 222-226.

Dee, D. P. (2005), Bias and data assimilation, *Q. J. Roy. Meteor. Soc.,* **131**(613), 3323-3343.

Dee, D. P., and S. Uppala (2009), Variational bias correction of satellite radiance data in the ERA-Interim reanalysis, *Q. J. Roy. Meteor. Soc.,* **135**(644), 1830-1841.

Dessler, A. E., and S. M. Davis (2010), Trends in tropospheric humidity from reanalysis systems, *J. Geophys. Res.,* **115**, D19127.

Dirmeyer, P.A., R.D. Koster, and Z. Guo (2006), Do global models properly represent the feedback between land and atmosphere?, *J. Hydrometeorol.,* **7**, 1177-1198.

Ehhalt, D. H., F. Rohrer, and A. Fried (2005), Vertical profiles of HDO/H2O in the troposphere, *J. Geophys. Res.,* **110**(D13), D13301.

Field, R. D., D. B. A. Jones, and D. P. Brown (2010), The effects of post-condensation exchange on the isotopic composition of water in the atmosphere, *J. Geophys. Res.,* **115**, D24305.

Flanagan, L. B., J. P. Comstock, and J. R. Ehleringer (1991), Comparison of Modeled and Observed Environmental-Influences on the Stable Oxygen and Hydrogen Isotope Composition of Leaf Water in Phaseolus-Vulgaris L, *Plant Phys.,* **96**(2), 588-596.

Fricke, H., and S.L. Wing (2004), Oxygen isotope and paleobotanical estimates of temperature and $\delta^{18}O$ – latitudinal gradients over North America during the early Eocene, *Am. J. Sci.,* **304**, 612-635.

Fu, R., B. Zhu, and R. E. Dickinson (1999), How do atmosphere and land surface influence seasonal changes of convection in the tropical amazon?, *J. Clim.,* **12**(5), 1306-1321.

Fu, R., W. Li (2004), The influence of the land surface on the transition from dry to wet season in Amazonia, *Theor. Appl. Climatol.,* **78**(1-3), 97-110.

Galewsky, J., A. Sobel, and I. Held (2005), Diagnosis of subtropical humidity dynamics using tracers of last saturation, *J. Atmos. Sci.,* **62**(9), 3353-3367.

Galewsky, J., and J. V. Hurley (2010), An advection-condensation model for subtropical water vapor isotopic ratios, *J. Geophys. Res.,* **115**, D16116.

Gamache, J. F., and R. A. Houze (1983), Water-Budget of a Mesoscale Convective System in the Tropics, *J. Atmos. Sci.,* **40**(7), 1835-1850.

Gat, J.R. (1996), Oxygen and hydrogen isotopes in the hydrologic cycle, *Ann. Rev. Earth Planet. Sci.,* **24**, 225-262.

Gedzelman, S., J. Lawrence, J. Gamache, M. Black, E. Hindman, R. Black, J. Dunion, H. Willoughby, and X. P. Zhang (2003), Probing hurricanes with stable isotopes of rain and water vapor, *Mon. Weather Rev.,* **131**(6), 1112-1127.

Grootes, P. M., M. Stuiver, L. G. Thompson, and E. Mosleythompson (1989), Oxygen Isotope Changes in Tropical Ice, Quelccaya, Peru, *J. Geophys. Res.,* **94**(D1), 1187-1194.

Guan, B., N. P. Molotch, D. E. Waliser, E. J. Fetzer, and P. J. Neiman (2010), Extreme snowfall events linked to atmospheric rivers and surface air temperature via satellite measurements, *Geophys. Res. Lett,* **37**, L20401.

Held, I. M., and B. J. Soden (2000), Water vapor feedback and global warming, *Annu. Rev. Energ. Env.,* **25**, 441-475.

Held, I. M., and B. J. Soden (2006), Robust responses of the hydrological cycle to global warming, *J. Clim.,* **19**(21), 5686-5699.

Henderson-Sellers, A., K. McGuffie, and H. Zhang (2002), Stable Isotopes as Validation Tools for Global Climate Model Predictions of the Impact of Amazonian Deforestation, *J. Clim.*, **15**, 2664–2677.

Henderson-Sellers, A., K. McGuffie, D. Noone, and P. Irannejad (2004), Using Stable Water Isotopes to Evaluate Basin-Scale Simulations of Surface Water Budgets, *J. Hydrometeorol.*, **5**, 805–822.

Henderson-Sellers, A., M. Fischer, I. Aleinov, K. McGuffie, W.J. Riley, G.A. Schmidt, K. Sturm, K. Yoshimura, and O. Irannejad (2006), Stable water isotope simulation by current land-surface schemes: Results of iPILPS Phase 1, *Global Planet. Change*, **51**, 34-58.

Hendricks, M. B., D. J. DePaolo, and R. C. Cohen (2000), Space and time variation of delta O-18 and delta D in precipitation: Can paleotemperatnre be estimated from ice cores?, *Global Biogeochem. Cycles,* **14**(3), 851-861.

Herbin, H., D. Hurtmans, S. Turquety, C. Wespes, B. Barret, J. Hadji-Lazaro, C. Clerbaux, and P. F. Coheur (2007), Global distributions of water vapour isotopologues retrieved from IMG/ADEOS data, *Atmos. Chem. Phys.,* **7**(14), 3957-3968.

Hoffmann, G. (2003), Taking the Pulse of the Tropical Water Cycle, *Science,* **301**, 776-777.

Huffman, G. J., R. F. Adler, B. Rudolf, U. Schneider, and P. R. Keehn (1995), Global Precipitation Estimates Based on a Technique for Combining Satellite-Based Estimates, Rain-Gauge Analysis, and Nwp Model Precipitation Information, *J. Clim.,* **8**(5), 1284-1295.

Hurley, J. V., and J. Galewsky (2010a), A Last Saturation Analysis of ENSO Humidity Variability in the Subtropical Pacific, *J. Clim.,* **23**(4), 918-931.

Hurley, J. V., and J. Galewsky (2010b), A last-saturation diagnosis of subtropical water vapor response to global warming, *Geophys. Res. Lett,* **37**, L06702.

Jouzel, J., and L. Merlivat (1984), Deuterium and O-18 in Precipitation - Modeling of the Isotopic Effects during Snow Formation, *J. Geophys. Res.,* **89**, 1749-1757.

Jouzel, J., F. Vimeux, N. Caillon, G. Delaygue, G. Hoffmann, V. Masson-Delmotte, and F. Parrenin (2003), Magnitude of isotope/temperature scaling for interpretation of central Antarctic ice cores, *J. Geophys. Res.*, **108**(D12), 4361.

Juárez, R.I.N., M.G. Hodnett, R. Fu, M.L. Goulden, and C. von Randow (2007), Control of Dry Season Evapotranspiration over the Amazonian Forest as Inferred from Observations at a Southern Amazon Forest Site, *J. Clim.*, **20**, 2827–2839.

Kalnay, E., M. Kanamitsu, R. Kistler, W. Collins, D. Deaven, L. Gandin, M. Iredell, S. Saha, G. White, J. Woollen, Y. Zhu, M. Chelliah, W. Ebisuzaki, W. Higgins, J. Janowiak, K. C. Mo, C. Ropelewski, J. Wang, A. Leetmaa, R. Reynolds, R. Jenne, and D. Joseph (1996), The NCEP/NCAR 40-year reanalysis project, *Bull. Am. Meteorol. Soc.,* **77**(3), 437-471.

Kirk, A. (1987), Southern-Hemisphere Energy Fluxes from Analyses with Special Respect to the Weddell Sea Region (Antarctica), *Meteorol. Atmos. Phys.,* **37**(3), 171-182.

Lawrence, J. R., and S. D. Gedzelman (1996), Low stable isotope ratios of tropical cyclone rains, *Geophys. Res. Lett.,* **23**(5), 527-530.

Lawrence, J. R., and S. D. Gedzelman (2003), Tropical ice core isotopes: Do they reflect changes in storm activity?, *Geophys. Res. Lett.,* **30**(2), 1072-1076.

Lawrence, J. R., S. D. Gedzelman, D. Dexheimer, H. K. Cho, G. D. Carrie, R. Gasparini, C. R. Anderson, K. P. Bowman, and M. I. Biggerstaff (2004), Stable isotopic composition of water vapor in the tropics, *J. Geophys. Res.,* **109**, D06115.

Lee, J., J. Worden, D. Noone, K. Bowman, A. Eldering, A. LeGrande, J. L. Li, G. Schmidt, and H. Sodemann (2010), Relating tropical ocean clouds to moist processes using water vapor isotope measurements, *Atmos. Chem. Phys. Discuss.,* **11**(2), 741-752.

Li, X. F., C. H. Sui, and K. M. Lau (2002), Precipitation efficiency in the tropical deep convective regime: A 2-D cloud resolving modeling study, *J. Meteorol. Soc. of Jpn.,* ***80***(2), 205-212.

Lindzen, R. S., M. D. Chou, and A. Y. Hou (2001), Does the earth have an adaptive infrared iris?, *Bull. Am. Meteorol. Soc.,* **82**(3), 417-432.

Lorenz, D. J., and E. T. DeWeaver (2007), The response of the extratropical hydrological cycle to global warming, *J. Clim.,* **20**(14), 3470-3484.

Malhi, Y., E. Pegoraro, A. D. Nobre, M. G. P. Pereira, J. Grace, A. D. Culf, and R. Clement (2002), Energy and water dynamics of a central Amazonian rain forest, *J. Geophys. Res.*, **107**(D20), 8061.

Manabe, S., and R. T. Wetherald (1975), Effects of Doubling Co2 Concentration on Climate of a General Circulation Model, *J. Atmos. Sci.,* **32**(1), 3-15.

Mapes, B., J. Bacmeister, M. Khairoutdinov, C. Hannay, and M. Zhao (2009), Virtual Field Campaigns on Deep Tropical Convection in Climate Models, *J. Clim.,* **22**(2), 244–257.

Martinelli, L.A., R.L. Victoria, L.S. Lobo Sternberg, A. Ribeiro, M. Zacharias Moreira (1996), Using stable isotopes to determine sources of evaporated water to the atmosphere in the Amazon Basin, *J. Hydrol.,* **183**(3), 191-204

Matsuyama, H., K. Miyaoka, and K. Masuda, (2005), Year-to-year variations of the stable isotopes in precipitation in February at Cuiab'a, located on the northern fringe of Pantanal, Brazil, *J. of Hydrometeorol.,* **6**, 324-329

McGuffie, K., and A. Henderson-Sellers (2004), Stable water isotope characterization of human and natural impacts on land-atmosphere exchanges in the Amazon Basin, *J. Geophys. Res.*, **109**, D17104

Merlivat, L., and J. Jouzel (1979), Global Climatic Interpretation of the Deuterium-Oxygen-18 Relationship for Precipitation, *J. Geophys. Res,* **84,** 5029-5033.

Mitchell, J. F. B., and W. J. Ingram (1992), Carbon-Dioxide and Climate - Mechanisms of Changes in Cloud, *J. Clim.,* **5**(1), 5-21.

Moorthi, S., and M. J. Suarez (1992), Relaxed Arakawa-Schubert - a Parameterization of Moist Convection for General-Circulation Models, *Mon. Weather Rev.,* **120**(6), 978-1002.

Munnich, M., and J. D. Neelin (2005), Seasonal influence of ENSO on the Atlantic ITCZ and equatorial South America, *Geophys. Res. Lett.,* **32**(21), L21709.

Neiman, P. J., F. M. Ralph, G. A. Wick, J. D. Lundquist, and M. D. Dettinger (2008), Meteorological characteristics and overland precipitation impacts of atmospheric rivers affecting the West Coast of North America based on eight years of SSM/I satellite observations, *J. Hydrometeorol.,* **9**(1), 22-47.

Newell, R. E., and Y. Zhu (1994), Tropospheric Rivers - a One-Year Record and a Possible Application to Ice Core Data, *Geophys. Res. Lett.,* **21**(2), 113-116.

Noone, D., J. Turner, and R. Mulvaney (1999), Atmospheric signals and characteristics of accumulation in Dronning Maud Land, Antarctica, *J. Geophys. Res.*, **104**(D16), 19,191–19,212.

Noone, D., and I. Simmonds (1999), A three-dimensional spherical trajectory algorithm, in *Research Activities in Atmospheric and Oceanic Modelling*, edited by H. Ritchie, pp. 3.26-3.27, World Meteorological Organization.

Noone, D. (2008), The influence of midlatitude and tropical overturning circulation on the isotopic composition of atmospheric water vapor and Antarctic precipitation, *J. Geophys. Res.,* **113,** D04102.

Noone, D. (2010), Identification of moistening and dehydration pathways in the tropical mid-troposphere from measurements of water vapor isotopic composition, *J. Clim.*, in review.

Okajima, H., S. P. Xie, and A. Numaguti (2003), Interhemispheric coherence of tropical climate variability: Effect of the climatological ITCZ*, J. Meteor. Soc. Japan,* **81**(6), 1371-1386.

Oort, A. H., and J. P. Peixoto (1983), Global Angular-Momentum and Energy-Balance Requirements from Observations, *Adv. Geophys.,* **25**, 355-490.

Payne, V. H., D. Noone, A. Dudhia, C. Piccolo, and R. G. Grainger (2007), Global satellite measurements of HDO and implications for understanding the transport of water vapour into the stratosphere, *Q. J. Roy. Meteorol. Soc.,* **133**(627), 1459-1471.

Peixoto, J. P., and A. H. Oort (1996), The climatology of relative humidity in the atmosphere, *J. Clim.,* **9**(12), 3443-3463.

Pierrehumbert, R. T. (1998), Lateral mixing as a source of subtropical water vapor, *Geophys. Res. Lett,* **25**(2), 151-154.

Pierrehumbert, R. T., and R. Roca (1998), Evidence for control of Atlantic subtropical humidity by large scale advection, *Geophys. Res. Lett.,* **25**(24), 4537-4540.

Pierrehumbert, R. T. (1999), Subtropical water vapor as a mediator of rapid global climate change, in *Mechanisms of Global Change at Millenial Time Scales, Geophys. Res. Lett.*, **112**, 339-361.

Price, J. D., and R. Wood (2002), Comparison of probability density functions for total specific humidity and saturation deficit humidity, and consequences for cloud parametrization, *Q. J. Roy. Meteorol. Soc.,* **128**(584), 2059-2072.

Ralph, F. M., P. J. Neiman, G. A. Wick, S. I. Gutman, M. D. Dettinger, D. R. Cayan, and A. B. White (2006), Flooding on California's Russian River: Role of atmospheric rivers, *Geophys. Res. Lett.,* **33**(13), L13801.

Randall, D. A., R. A. Wood, S. Bony, R. Colman, T. Fichefet, J. Fyfe, V. Kattsov, A. Pitman, J. Shukla, J. Srinivasan, R. J. Stouffer, A. Sumi and K. E. Taylor (2007), Climate Models and Their Evaluation. In: Climate Change 2007: The Physical Science Basis. Contribution of Working Group I to the Fourth Assessment Report of the Intergovernmental Panel on Climate Change [Solomon, S., D. Qin, M. Manning, Z. Chen, M. Marquis, K. B. Averyt, M.Tignor and H. L. Miller (eds.)]. Cambridge University Press, Cambridge, United Kingdom and New York, NY, USA.

Rienecker, M. M., M. J. Suarez, R. Todling, J. Bacmeister, L. L. Takacs, H.-C. Liu, W. Gu, M. Sienkiewicz, R. D. Koster, R. Gelaro, I. Stajner, and E. Nielsen (2008), The GEOS-5 Data Assimilation System - Documentation of Versions 5.0.1, 5.1.0, and 5.2.0, *The Technical Report Series on Global Modeling and Data Assimilation 104606,* **27.**

Rind, D., E. W. Chiou, W. Chu, J. Larsen, S. Oltmans, J. Lerner, M. P. Mccormick, and L. Mcmaster (1991), Positive Water-Vapor Feedback in Climate Models Confirmed by Satellite Data, *Nature, 349*, 500-503.

Risi, C., S. Bony, and F. Vimeux (2008a), Influence of convective processes on the isotopic composition (delta O-18 and delta D) of precipitation and water vapor in the tropics: 2. Physical interpretation of the amount effect, *J. Geophys. Res.,* **113,** D19306.

Risi, C., S. Bony, F. Vimeux, L. Descroix, B. Ibrahim, E. Lebreton, I. Mamadou, and B. Sultan (2008b), What controls the isotopic composition of the African monsoon precipitation? Insights from event-based precipitation collected during the 2006 AMMA field campaign, *Geophys. Res. Lett.,* **35**, L24808.

Rozanski, K., L. Araguasaraguas, and R. Gonfiantini (1992), Relation between Long-Term Trends of O-18 Isotope Composition of Precipitation and Climate, *Science,* **258**(5084), 981-985.

Rozanski, K., L. Araguas-Araguas, and R. Gonfiantini (1993), Isotopic patterns in modern global precipitation, in *Climate Change in Continental Isotopic Records*, edited by P. K. Swart, K. L. Lohmann, J. McKenzie, and S. Savin, *AGU Geophys. Monogr.,* **78**, 1-37.

Rozanski, K. and L. Araguas-Araguas (1995), Spatial and temporal variability of stable isotope composition of precipitation over the South American continent, *Bull. Inst. Fr. Etudes Andines*, **24**, 379-390.

Ryoo, J. M., T. Igusa, and D. W. Waugh (2009), PDFs of Tropical Tropospheric Humidity: Measurements and Theory, *J. Clim.,* **22**(12), 3357-3373.

Salathe, E. P., and D. L. Hartmann (1997), A trajectory analysis of tropical upper-tropospheric moisture and convection, *J. Clim.,* **10**(10), 33, 2533-2547.

Salati, E., and P.B. Vose (1984), Amazon Basin: A System in Equilibrium, *Science,* **225**(4658), 129.

Schmidt, G. A., G. Hoffmann, D. T. Shindell, and Y. Y. Hu (2005), Modeling atmospheric stable water isotopes and the potential for constraining cloud processes and stratosphere-troposphere water exchange, *J. Geophys. Res.,* **110**, D21314.

Seager, R., N. Naik, and G. A. Vecchi (2010), Thermodynamic and Dynamic Mechanisms for Large-Scale Changes in the Hydrological Cycle in Response to Global Warming, *J. Clim.,* **23**(17), 4641-4668.

Sengupta, S. and A. Sarkar (2006), Stable isotope evidence of dual (Arabian Sea and Bay of Bengal) vapor sources in monsoonal precipitation over north India, *Earth Planet. Sci. Lett.*, **250**, 511-521.

Shephard, M. W., R. L. Herman, B. M. Fisher, K. E. Cady-Pereira, S. A. Clough, V. H. Payne, D. N. Whiteman, J. P. Comer, H. Vomel, L. M. Miloshevich, R. Forno, M. Adam, G. B. Osterman, A. Eldering, J. R. Worden, L. R. Brown, H. M. Worden, S. S. Kulawik, D. M. Rider, A. Goldman, R. Beer, K. W. Bowman, C. D. Rodgers, M. Luo, C. P. Rinsland, M. Lampel, and M. R. Gunson (2008), Comparison of Tropospheric Emission Spectrometer nadir water vapor retrievals with in situ measurements, *J. Geophys. Res.,* **113,** D15S24.

Sherwood, S. C. (1996), Maintenance of the free-tropospheric tropical water vapor distribution .2. Simulation by large-scale advection, *J. Clim.,* **9**(11), 2919-2934.

Sherwood, S. C., E. R. Kursinski, and W. G. Read (2006), A distribution law for free-tropospheric relative humidity, *J. Clim.,* **19**(24), 6267-6277.

Sherwood, S. C., W. Ingram, Y. Tsushima, M. Satoh, M. Roberts, P. L. Vidale, and P. A. O'Gorman (2010a), Relative humidity changes in a warmer climate, *J. Geophys. Res.,* **115,** D09104.

Sherwood, S. C., R. Roca, T. M. Weckwerth, and N. G. Andronova (2010b), Tropospheric Water Vapor, Convection, and Climate, *Rev. Geophys.,* **48,** RG2001.

Soden, B. J., and I. M. Held (2006), An assessment of climate feedbacks in coupled ocean-atmosphere models. *J. Clim.*, **19**, 3354–3360.

Solomon, A. B. (1997), An observational study of the spatial and temporal scales of transient eddy sensible heat fluxes, *J. Clim.,* **10**(3), 508-520.

Stendel, M., J. R. Christy, and L. Bengtsson (2000), Assessing levels of uncertainty in recent temperature time series, *Clim. Dynam.,* **16**(8), 587-601.

Still, C. J., W. J. Riley, S. C. Biraud, D. C. Noone, N. H. Buenning, J. T. Randerson, M. S. Torn, J. Welker, J. W. C. White, R. Vachon, G. D. Farquhar, and J. A. Berry (2009), Influence of clouds and diffuse radiation on ecosystem-atmosphere CO2 and (COO)-O-18 exchanges, *J. Geophys. Res.,* **114,** G01018.

Suarez, M. J., M.M. Rienecker, M.J. Suarez, R. Todling, J. Bacmeister, L. Takacs, H.-C. Liu, W. Gu, M. Sienkiewicz, R.D. Koster, R. Gelaro, I. Stajner, and J.E. Nielsen (2008), The GEOS-5 Data Assimilation System - Documentation of Versions 5.0.1, 5.1.0, and 5.2.0, *NASA Tech. Memo., NASA/TM-2008-104606, 27, 97* pp.

Sun, D. Z., and R. S. Lindzen (1993), Distribution of Tropical Tropospheric Water-Vapor, *J. Atmos. Sci.,* **50**(12), 1643-1660.

Sun, D. Z., and I. M. Held (1996), A comparison of modeled and observed relationships between interannual variations of water vapor and temperature, *J. Clim.,* **9**(4), 665-675.

Sundqvist, H. (1978), Parameterization Scheme for Non-Convective Condensation Including Prediction of Cloud Water-Content, *Q. J. Roy. Meteorol. Soc.,* **104**(441), 677-690.

Tian, L., T. Yao, K. MacClune, J. W. C. White, A. Schilla, B. Vaughn, R. Vachon, and K. Ichiyanagi (2007), Stable isotopic variations in west China: A consideration of moisture sources, *J. Geophys. Res.*, **112**, D10112

Trenberth, K. E. (1980), Planetary-Waves at 500-Mb in the Southern-Hemisphere, *Mon. Weather Rev.,* **108**(9), 1378-1389.

Trenberth, K. E., and C. J. Guillemot (1995), Evaluation of the Global Atmospheric Moisture Budget as Seen from Analyses, *J. Clim.,* **8**(9), 2255-2280.

Trenberth, K. E., and C. J. Guillemot (1998), Evaluation of the atmospheric moisture and hydrological cycle in the NCEP/NCAR reanalyses, *Clim. Dynam.,* **14**(3), 213-231.

Trenberth, K. E. (1999), Atmospheric moisture recycling: Role of advection and local evaporation, *J. Clim.,* **12**(5), 1368-1381.

Trenberth, K. E., D. P. Stepaniak, and J. M. Caron (2002), Accuracy of atmospheric energy budgets from analyses, *J. Clim.,* **15**(23), 3343-3360.

Vimeux, F., R. Gallaire, S. Bony, G. Hoffman, J.C.H. Chiang (2005), What are the climate controls on δD in precipitation in the Zongo Valley (Bolivia)? Implications for the Illimani ice core interpretation, *Earth Planet. Sci. Lett.*, **240**, 205-220.

Vuille, M., M. Werner, R. S. Bradley, and F. Keimig (2005), Stable isotopes in precipitation in the Asian monsoon region, *J. Geophys. Res.*, **110**, D23108.

Uppala, S.M., et al. (2005), The ERA-40 Re-analysis, *Q. J. Roy. Meteorol. Soc.*, **131**, 2961-3012.

Webster, C. R., and A. J. Heymsfield (2003), Water isotope ratios D/H, O-18/O-16, O-17/O-16 in and out of clouds map dehydration pathways, *Science,* **302**, 1742-1745.

Wexler, H. (1959), Seasonal and Other Temperature Changes in the Antarctic Atmosphere, *Q. J. Roy. Meteorol. Soc.,* **85**(365), 196-208.

Willett, K. M., P. D. Jones, N. P. Gillett, and P. W. Thorne (2008), Recent Changes in Surface Humidity: Development of the HadCRUH Dataset, *J. Clim.,* **21**(20), 5364-5383.

Winton, M. (2006), Surface albedo feedback estimates for the AR4 climate models. *J. Clim.*, **19**, 359–365.

Wolter, K., and M. S. Timlin (1998), Measuring the strength of ENSO events: How does 1997/98 rank?, *Weather,* **53**(9), 269-324.

Worden, J., S. S. Kulawik, M. W. Shephard, S. A. Clough, H. Worden, K. Bowman, and A. Goldman (2004), Predicted errors of tropospheric emission spectrometer nadir retrievals from spectral window selection, *J. Geophys. Res.,* **109**(D9), D09308.

Worden, J., K. Bowman, D. Noone, R. Beer, S. Clough, A. Eldering, B. Fisher, A. Goldman, M. Gunson, R. Herman, S. S. Kulawik, M. Lampel, M. Luo, G. Osterman, C. Rinsland, C. Rodgers, S. Sander, M. Shephard, and H. Worden (2006), Tropospheric emission spectrometer observations of the tropospheric HDO/H2O ratio: Estimation approach and characterization, *J. Geophys. Res.,* **111**, D16309.

Worden, J., D. Noone, and K. Bowman (2007), Importance of rain evaporation and continental convection in the tropical water cycle, *Nature***, 445**(7127),528-532.

Wright, J. S., R. Fu, and A. J. Heymsfield (2009a), A statistical analysis of the influence of deep convection on water vapor variability in the tropical upper troposphere, *Atmos. Chem. Phys.,* **9**(15), 5847-5864.

Wright, J. S., A. H. Sobel, and G. A. Schmidt (2009b), Influence of condensate evaporation on water vapor and its stable isotopes in a GCM, *Geophys. Res. Lett.,* **36**, L12804.

Wright, J. S., A. Sobel, and J. Galewsky (2010), Diagnosis of Zonal Mean Relative Humidity Changes in a Warmer Climate, *J. Clim.,* **23**(17), 4556-4569.

Wu, X. Q., X. Z. Liang, and G. J. Zhang (2003), Seasonal migration of ITCZ precipitation across the equator: Why can't GCMs simulate it?, *Geophys. Res. Lett.,* **30**(15), D1824.

Wushiki, H. (1977) Deuterium content in the Himalayan precipitation at Khumbu District, observed in 1974/1975. In, Higuchi, K., Hakajima, C. and Kusunoki, K., eds. *Glaciers and Climates of Nepal Himalayas. Report of the Glaciological Expedition to Nepal: Part 2. Seppyo, Special Issue*, **39**, 50-56.

Yang, H., and R. T. Pierrehumbert (1994), Production of Dry Air by Isentropic Mixing, *J. Atmos. Sci.,* **51**(23), 3437-3454.

Zakharov, V. I., R. Imasu, K. G. Gribanov, G. Hoffmann, and J. Jouzel (2004), Latitudinal distribution of the deuterium to hydrogen ratio in the atmospheric water vapor retrieved from IMG/ADEOS data, *Geophys. Res. Lett.,* **31**(12), L12104.

Zhang, C. D. (2005), Madden-Julian oscillation, *Rev. Geophys.,* **43**(2), RG2003.

Zhu, Y., and R. E. Newell (1994), Atmospheric Rivers and Bombs, *Geophys. Res. Lett.,* **21**(18), 1999-2002.

Zhu, Y., and R. E. Newell (1998), A proposed algorithm for moisture fluxes from atmospheric rivers, *Mon. Weather Rev.,* **126**(3), 725-735.